Computational Modelling and Haemodynamic Investigation of Intracranial Aneurysms Before and After Flow-Diversion Treatment

Yujie Li

A thesis submitted to Macquarie University

for the degree of Doctor of Philosophy

October 31, 2018

MACQUARIE
University
SYDNEY·AUSTRALIA

Computational Modelling and Haemodynamic Investigation of Intracranial Aneurysms Before and After Flow-Diversion Treatment

Yujie Li

Department of Biomedical Sciences

Faculty of Medicine and Health Sciences

Supervisor:

Itsu Sen (Yi Qian), PhD

Co-supervisors:

Makoto Ohta, PhD

David Ignatius Verrelli, PhD

Y. Li

Sydney, Australia

STATEMENT OF ORIGINALITY

This work has not previously been submitted for a degree or diploma in any university, except for Tohoku University per the thesis submission agreement signed by both Macquarie University and Tohoku University before commencement of this joint-supervision Cotutelle program. To the best of my knowledge and belief, the thesis contains no material previously published or written by another person except where due reference is made in the thesis itself.

Yujie Li

October 31, 2018

Table of Content

Acknowledgement

It has been a gift to become a PhD candidate. During these years, all that I have seen, learned, and experienced contribute to my pursuit of the PhD, which is not only the degree itself, but also a better recognition of myself. This journey has brought challenges to me that I had never thought about, it has always been teaching me as much as it could and will always be a precious experience in my life. Before the end of my PhD study, I have many sincere thanks.

I wish to express my great thank to my supervisor in Macquarie University, Prof. Itsu Sen (Yi Qian), for providing me the opportunity to join the Cotutelle PhD program and giving me the access to obtain more achievements. The immense knowledge and rich experience of him become thoughtful considerations and valid opinions, giving me tremendous helps in an improved outlook in both research and life.

I also wish to express my sincere gratitude to my co-supervisor in Tohoku University, Prof. Makoto Ohta, for the continuous support and encouragement during my PhD study, not only in guiding me in the research with insightful comments, but also in supporting my life of studying abroad with unreserved concerns. The kindness of him has supported me to obtain many precious opportunities that have certainly broadened my horizontal in both research and life.

My sincere thank also goes to Dr. David Ignatius Verrelli, who is the co-supervisor of mine in Macquarie University, for not only being an advisor but also a friend. I am grateful for his tremendous contribution in helping me dealing with difficulties that I met in research as well as in academic English writing, as his suggestions and comments could always lead me to a solution. The professional knowledge and rigorous logic of him have enlightened me with a scientific method to comprehend and analyse a problem.

I also wish to express many thanks to my thesis examination committee at Tohoku University, Prof. Toshiyuki Hayase and Prof. Takuji Ishikawa. The inspiring suggestions and advises from them have tremendously improved the quality of this thesis.

I would also like to express my gratitude to Ms. Yasuno Emori, the secretary of Ohta lab at Tohoku University, for her great help in preparing many administration documents for me, as well as helping me deal with all kinds of daily affairs.

I also wish to acknowledge the many unreserved help, consistent support, and precious friendship that I received from all the lovely lab members in Ohta lab and Sen group over these years. I would like to express my sincere gratefulness to each one of them, for the happiness they have added to my PhD life.

I would like to thank Prof. Osamu Sasaki and Dr. Harumasa Kano from Tohoku University Museum for their kind support of equipment and technique for micro-CT scanning, which helped me get experimental data in good quality.

More thanks are expressed to Mr. Takashi Kosugi and Mr. Takafumi Kosugi from R-Tech in Japan, Prof. Haruo Isoda from Nagoya University in Japan, Prof. Winston Chong from Monash Medical Centre in Australia, and Dr. William Yang from CSIRO in Australia, for their kind contributions in our collaboration studies.

Special thank must goes to Mingzi Zhang, who is not only a good colleague, but also has been the best partner in both research and life, with consistent accompany over these years, sharing all the hard work and joys. The great endeavour and provident vision of him has been a good example, and the encouragement and concerns from him has helped me go through many challenges.

In the end, great thanks must be expressed to my parents, for their consistent concerns, selfless support and great understandings, which provide me a perfect environment to pursue my study. This work will not exist without their dedication.

Yujie Li

October 31, 2018

Summary

Haemodynamic information is believed to be one of the most crucial factors affecting the initiation, development, growth, and rupture of intracranial aneurysms (IAs). Many studies of haemodynamic simulation contribute to the understanding of aneurysmal flow dynamics; however, clarification and justification of the validity of simulation results inconclusive remains. Besides, for most simulations of flow-diversion effect using a model flow-diverting (FD) stent, the properties of model FD stents failed to be calibrated to match the represented device, which would lead to inaccurate predictions of flow-diversion efficacy.

Thus, this study aims to discover the factors that contribute to a more accurate and comprehensive simulation of aneurysmal haemodynamics and its flow-diversion treatment. Two main aspects were investigated in this thesis: 1) evaluation of the accuracy of computational fluid dynamics (CFD) predictions of aneurysmal haemodynamics before and after FD stent treatment, by comparing to *in vivo* and *in vitro* observations; and 2) investigation of the practicality of using porous medium (PM) stent models, with calibration of stent model parameters to represent the commercially available FD stents, by derivation of parameters like permeability (k) that account for the flow resistance induced by the model stent.

To meet these needs, haemodynamic investigations of IAs and their flow-diversion treatments have been performed using different approaches. In Chapter 3 and 4, the validity of CFD predictions of aneurysmal haemodynamics was evaluated, by comparing the resolved velocity field in patient-specific aneurysms with experimental methods, such as particle image velocimetry (PIV) and phase-contrast magnetic resonance imaging (PCMRI). By comparing against a physical stent model, the PM model stent was found to be a practical tool to assist flow-diversion simulation. In Chapter 5 and 6, the PM model thickness range that would help to retain the simulation benefits without compromising the accuracy was first confirmed; then PM model FD stents were respectively calibrated to reflect the flow resistance created by several treatment modes using commercially available FD stents.

Overall, CFD prediction is proved to be able to accurately resolve the aneurysmal flow dynamics, and the investigation of calibrated PM stent modelling provides an individualised method that is more efficient than CFD simulations with a fully-resolved stent model yet retains simulation accuracy. These studies substantially contribute to an improved validity of aneurysmal haemodynamic simulation, thereby enhancing the clinical relevance of such aneurysmal haemodynamic studies in the future.

List of Publications

Publications in Peer-Reviewed Academic Journals:

1. **Li Y.**, Anzai H., Nakayama T., Shimizu Y., Miura Y., Qiao A., Ohta M., 2014. Simulation of hemodynamics in artery with aneurysm and stenosis with different geometric configuration. *Journal of Biomechanical Science and Engineering*. Vol. 9, No. 1. (Refer to Section 2.4 and Appendix I)

2. **Li Y.**, Zhang M., Verrelli D. I., Chong W., Ohta M., Qian Y., 2018. Numerical simulation of aneurysmal haemodynamics with calibrated porous-medium models of flow-diverting stents. *Journal of Biomechanics*. 80(2018), 88-94. (Refer to Chapter 6)

3. Zhang M., **Li Y.**, Zhao X., Verrelli D. I., Chong W., Ohta M., Qian Y., **2017**. Haemodynamic effects of stent diameter and compaction ratio on flow-diversion treatment of intracranial aneurysms: A numerical study of a successful and an unsuccessful case. *Journal of Biomechanics*. 58(2017), 179-186.

4. Dai Y., Qian Y., Zhang M., **Li Y.**, Lv P., Tang X., Javadzadegan A., Lin J., **2018**. Associations between local haemodynamics and carotid intraplaque haemorrhage with different stenosis severities: a preliminary study based on MRI and CFD. *Journal of Clinical Neuroscience*. 66(2019), 220-225.

5. **Li Y.** & Verrelli D. I., Yang W., Qian Y., Chong W., **2019**. Validation of CFD model results against PIV observations of haemodynamics in intracranial aneurysms treated with flow-diverting stent. Submitted to *Journal of Biomechanics*. (Refer to Chapter 4; Under Review)

6. Zhang M., **Li Y.**, Verrelli D. I., Chong W., Ohta M., Qian Y., **2018**. Haemodynamic outcomes of intracranial aneurysm treatments with dual flow-diverting stents of different sizes. Submitted to the *Journal of Biomechanics*. (Under Review)

7. Zhang M., **Li Y.**, Sugiyama S., Verrelli D. I., Matsumoto Y., Tominaga T., Qian Y., Ohta M., **2018**. Incomplete stent expansion (IncSE) in flow-diversion treatment affects aneurysmal haemodynamics: A quantitative comparison of treatments affected by

different severities of malapposition occurring in different segments of the parent artery. Submitted to the *Journal of Biomechanics*. (Under Review)

Publications in Peer-Reviewed Conference Proceedings:

1. **Li Y.**, Zhang M., Verrelli D. I., Yang W., Chong W., Ohta M., Qian Y., **2017.** A sensitivity study on modelling a flow-diverting stent as a porous medium using computational fluid dynamics, in: *Engineering in Medicine and Biology Society (EMBC)*, pp. 3389-3392, 2017 *IEEE* the 39th Annual International Conference of the IEEE. doi:10.1109/EMBC.2017.8037583 (Refer to Chapter 5)

2. **Li Y.**, Zhang M., Verrelli D. I., Yang W., Chong W., Ohta M., Qian Y., **2017.** Modelling flow-diverting stent as porous medium with different permeabilities in the treatment of intracranial aneurysms: a comparison of a successfully treated case and an unsuccessful one, in *Proceedings of the 8th International Conference on Computational Methods* (*ICCM2017)*

3. Zhang M., **Li Y.**, Verrelli D. I., Chong W., Ohta M., Qian Y., **2017**. Applying computer simulation to the design of flow-diversion treatment for intracranial aneurysms, in: *Engineering in Medicine and Biology Society (EMBC)*, pp. 3385-3388, 2017 *IEEE* the 39th Annual International Conference of the IEEE. doi:10.1109/EMBC.2017.8037582

4. Zhang M., **Li Y.**, Verrelli D. I., Chong W., Ohta M., Qian Y., **2017**. Applying virtual stent deployment to study flow-diversion treatment for intracranial aneurysm: the effect of stent compaction on post-treatment wire configuration, in: *Proceedings of the 8th International Conference on Computational Methods* (*ICCM2017)*

Publications in Non-Peer-Reviewed Academic Journals:

1. 太田信，安西眸，吉田裕貴，Zhang Mingzi，**Li Yujie**，中山敏男. ステントの最適デザインを考える. 脳神経外科速報, 2014, vol. 24(5), pp. 532-537.

Co-authored Book Chapters:

1. 太田信，安西眸，吉田裕貴，Zhang Mingzi，**Li Yujie**，中山敏男. 基礎からよくわかる，実践的 CFD（数値流 体力学）入門，脳血管編，**2017**. Chapter 4(2), pp. 165-171. ISBN-10: 4-8404-6147-3, ISBN-13: 978-4-8404-6147-4.

Manuscripts in Preparation:

1. Yujie Li, Yoneyama Y., Terada M., Isoda H., Kosugi T., Kosugi T., Zhang M., Ohta M., intended submission in 2018. Haemodynamics in a patient-specific intracranial aneurysm obtained from experimental and numerical approaches: a comparison between PIV, CFD, and PCMRI, intended journal is *Technology and Healthcare*. (Refer to Chapter 3)

List of Figures

List of Table

List of Abbreviations

2D	Two-dimensional
3D	Three-dimensional
AAV	Aneurysmal Average Velocity
ACA	Anterior Communicating Artery
AR	Aspect Ratio
BA	Basilar Artery
BAF	Blood-Analogue FLuid
CAD	Computer-Aided Design
CCD	Charge-Coupled Device
CFD	Computational Fluid Dynamics
CT	Computed Tomography
CTA	Computed Tomography Angiography
DICOM	Digital Imaging and Communications in Medicine
DSA	Digital Subtraction Angiography
EL	Energy Loss
FD	Flow-diverting
FDM	Finite Difference Method
FEM	Finite Element Method
FRED	Flow Redirection Endoluminal Device
FVM	Finite Volume Method
GON	Gradient Oscillatory Number
IA	Intracranial Aneurysm
ICA	Internal Carotid Artery
LPCA	Left Posterior Cerebral Artery
MCA	Middle Cerebral Artery
MCR	Metal Coverage Ratio
MFR	Mass Flow Rate
microCT	Microscopic Computed Tomography
MRFD	Magnetic Resonance Fluid Dynamics
MRI	Magnetic Resonance Imaging
MRA	Magnetic Resonance Angiography
OSI	Oscillatory Shear Index

PCA	Posterior Communicating Artery
PCMRI	Phase-Contrast Magnetic Resonance Imaging
PDE	Partial Differential Equation
PED	Pipeline Embolization Device
PIV	Particle Image Velocimetry
PM	Porous Medium
Re	Reynold number
RPCA	Right Posterior Cerebral Artery
RRT	Relative Residence Time
SAH	Subarachnoid Haemorrhage
STL	Stereolithography
TOF	Time-of-flight
VMTK	Vascular Modelling Toolkit
VSD	Virtual Stent Deployment
WSS	Wall Shear Stress

Chapter 1
Introduction

1.1 Intracranial Aneurysms

An intracranial aneurysm (IA), also referred to as a brain aneurysm or cerebral aneurysm, is an intracranial vascular disorder that appears as a balloon-like bulge that dilates out from a localised weakness in the brain artery wall [1] (see Figure 1-1 [2]). The prevalence rate of IAs in the adult population is up to 5 % [1].

IAs vary in both size and shape [3,4]. Aneurysms are respectively regarded as small, large, giant, and super-giant aneurysms for aneurysms with diameter less than 15 mm, between 15 to 25 mm, between 25 to 50 mm, and over 50 mm [5]. IAs are classified into three types by shape, which are saccular aneurysms, fusiform aneurysms, and micro-aneurysms [1]. Saccular aneurysms, arising from one side of the blood vessel with a neck and a stem, often occur at the bifurcations and branches of large arteries at the Circle of Willis [6,7]; and it is the most common type of IA. Fusiform aneurysms, which have lower occurrence rates, manifest as an expansion in all directions of the artery locally. Micro-aneurysms are related to chronic hypertension, and often occur in small blood vessels (less than 300 μm).

1.1.1 Causes

The exact mechanisms of the initiation, development, and rupture of an aneurysm still remain unknown. However, some risk factors are considered to be related to the aneurysm formation and growth. Both illnesses and genetic conditions may lead to the initiation of an aneurysm, together with factors like hypertension, smoking, excessive alcoholism, obesity, and cocaine intake; in addition, head trauma and infections are also believed to be associated with aneurysm development [8–11].

1.1.2 Symptoms and risks

Patients with an aneurysm may experience various symptoms like headache, nausea, vomiting, and abnormal vision, *etc.*, while it is also possible for some patients to have no symptoms [12]; this largely depends on the status of the aneurysm. A severe consequence of IA development is the rupture of aneurysm, which may result in subarachnoid haemorrhage (SAH), known as brain bleeding. Patients with SAH have high risk of brain damage with paralysis or coma, even death. According to the collected data by a study of sudden death [13], ruptured IA account for 1.5 % of all natural sudden death. Additionally, the mortality rate at 30 days after rupture can reach as much as 30 % [1].

The occurrence rate and danger level of aneurysms with respect to their locations and shapes also differ. It is generally believed that larger aneurysms have higher tendency to rupture than smaller aneurysms; and also saccular aneurysms have higher risk of SAH than fusiform aneurysms [14].

1.1.3 Diagnosis

Most of the aneurysms are discovered when they start to rupture [15]. For most unruptured aneurysms, they are more likely to be discovered during routine brain imaging test incidentally [15].

Arteries where most IAs were identified are the anterior communicating artery (ACA), internal carotid artery (ICA), and posterior communicating artery (PCA), with collective occurrence rate of 30 to 35 %, followed by the middle cerebral artery (MCA) with 20 % [16].Depending on the location of the aneurysm and the patient's medical history, one or more of the following diagnostic tools can be adopted to observe the condition of the aneurysm [17].

i. Magnetic resonance imaging and angiography (MRI/MRA), which produce detailed images of tissues and blood vessels in the brain, using strong magnetic field, radio waves, and field gradients [18].

ii. Computed tomography angiography scan (abbreviated as CT/CTA scan), which produces a series of cross-sectional images that are able to capture detailed images of areas in the brain, using a combination of X-ray scans from different angles [18,19].

iii. Cerebral angiography, based on digital subtraction angiography (DSA) technique, which is a procedure to evaluate various conditions of the blood vessels, using X-ray images of the visible blood vessels after injection of contrast medium into an artery.

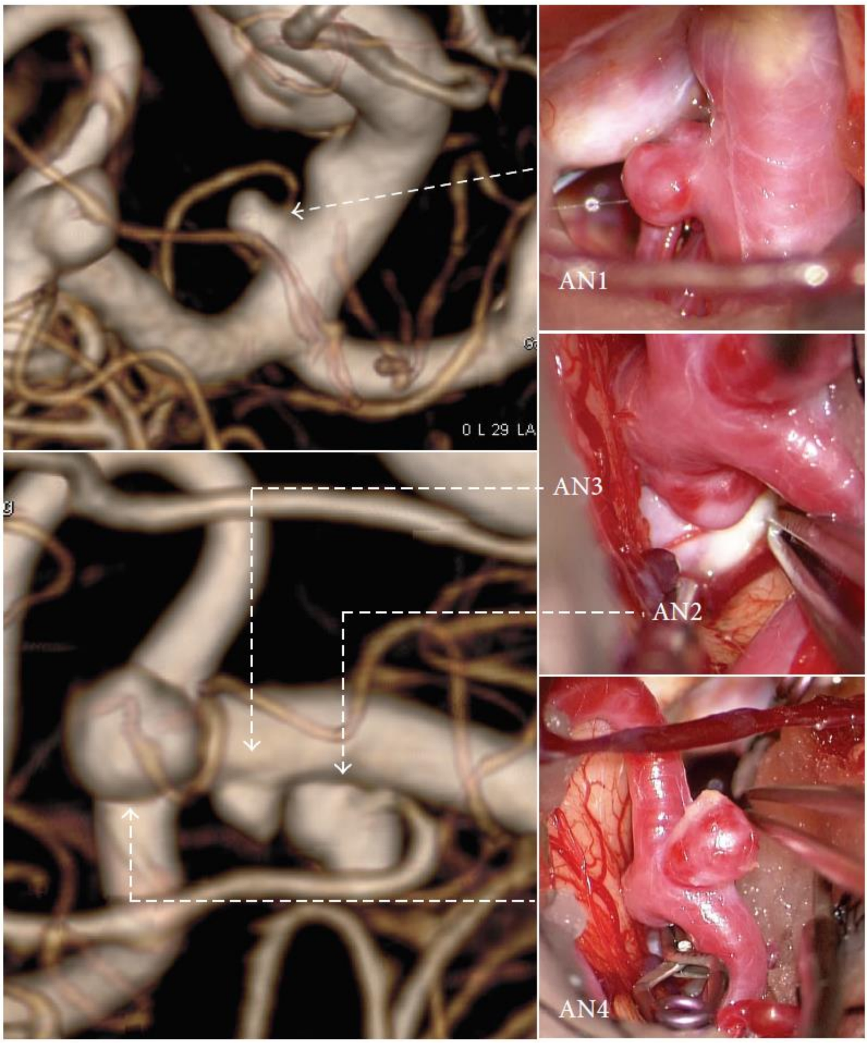

Figure 1-1 Intracranial aneurysms observed in rotational angiography (left) and *in vivo* (right). AN1 to AN4 in the intraoperative photographs respectively correspond to the four aneurysms identified in the rotational angiographical images. [2]

1.1.4 Treatments

The treatment of an aneurysm is determined from among the following methods according to the patient's need and the condition of the aneurysm. The size and location, and whether or not the aneurysm has ruptured, help medical doctors make a decision on each individual treatment [20–22].

1.1.4.1 Surgical clipping

The procedure of surgical clipping requires the surgeon to perform open-head surgery, during which the blood supply to the aneurysm will be blocked by putting a metal clip at the base of the aneurysm (see Figure 1-2(a) [23]). Surgical clipping is a more

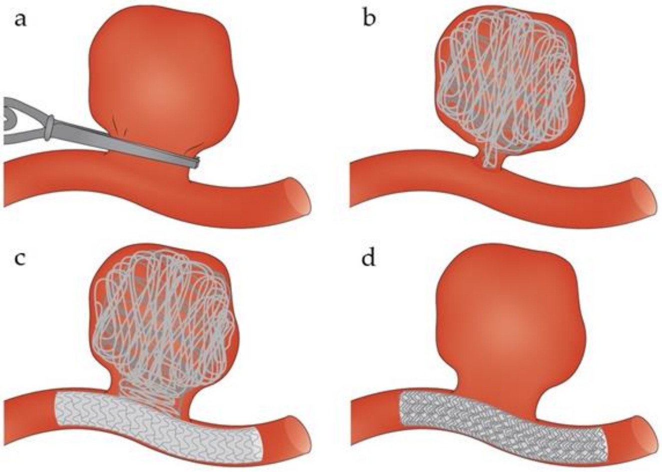

Figure 1-2 Treatments of IAs: (a) surgical clipping (b) coiling (c) coiling with assistant stent (d) FD stent [23]

established method for treating aneurysms, but it requires the neurosurgeons to be adequately experienced with precision and deep understanding of the structure of the brain, as otherwise may increase the complexities and risks of the procedure [24].

1.1.4.2 Endovascular treatments

Procedures using endovascular devices constitute a more recent method for the treatment of IAs. Treatment with endovascular devices, such as coils and flow-diverting (FD) stents, has been found to produce good clinical outcomes as a minimal-invasive method [25,26].

The procedure of endovascular coiling is performed by sending a catheter to the aneurysm through an artery, and then releasing platinum coils into the aneurysm to block the blood flow from entering it, thereby promoting aneurysmal thrombosis [27] (see Figure 1-2(b) [23]). For wide-neck aneurysms, a stent could be placed in the artery, across the aneurysm neck, supporting the coils inside the aneurysm (see Figure 1-2(c)). However, it also has risks of thrombosis and stenosis, and the recurrence rate can be higher especially for the coil treatment with wide-neck aneurysms [28].

A breakthrough treatment for complex aneurysms, for example the wide-neck aneurysm, the fusiform aneurysm, and the bifurcation aneurysm, has been developed, which is the FD stent. It offers these patients a successful alternative (> 90 %) to the previous treatment strategies [29].

Figure 1-3 Representatives of commercially available FD stents on the market [30-32]

A FD stent is a tubular metal mesh to be deployed in the parent artery across the aneurysm neck, to divert blood flow away from entering the aneurysm sac [26] (see Figure 1-2(d) [23]). Several brands of FD stent are currently available on the market (see Figure 1-3 [30–32]), *i.e.* Pipeline Embolization Device (*PED*; EV3-MT, Irvine, USA) [30,33], *Silk* FD stent (Balt, Montmorency, France) [32,34], Surpass (Stryker, Fremont, USA), and Flow Redirection Endoluminal Device (*FRED*; Microvention, Tustin, USA) [31]; these FD stents have different structures, varying in wire number, wire thickness, number of wire layers, braiding angle, and porosity (metal-free to total area) [26], thereby resulting in different flow-diversion effect.

1.2 Haemodynamics

Haemodynamics refers to the dynamics of blood flow, which depends on the physical laws that determine the blood flow in the vessels. Haemodynamic conditions continuously vary with respect to the environment and conditions in the human body.

1.2.1 The Study of Blood Flow

1.2.1.1 Blood and its Properties

Blood comprises plasma, red blood cells, white blood cells, and platelets. Due to different components in the blood, their continuous interaction between each other make the blood act more like a non-Newtonian fluid [35,36].

Blood plasma behaves like a Newtonian fluid [37]. At temperature of 37 ℃, the typical value of viscosity is 1.4 mPa·s [38], and it varies with temperature changes. The density of blood plasma is around 1050 kg/m^3 [39].

1.2.1.2 Cardiac Flow Rate

The pumping heart with rhythmic contraction and relaxation provides the original power that drives the blood running through the entire circulatory system. The volumes of blood within a unit time, also known as the blood flow rate, pumped out from the heart and returning to the heart are supposed to be approximately equal.

1.2.1.3 Pressure in Circulatory System

The blood pressure in the circulatory system is created by the heartbeat which also generates pulsatile blood flow. The pressure periodically varies between the maximal value and the minimal value — the systolic pressure and the diastolic pressure [40].

1.2.1.4 Velocity

The velocity of blood in different blood vessels is mainly associated with the total cross-sectional area of the corresponding level in the circulatory system that each vessel belongs to. The velocity is expressed as the blood flow rate in the given vessel divided by the local cross-sectional area.

The blood flow in cerebral vascular belongs to laminar flow in normal conditions [41], so that the velocity in the centre of the vessel is largest while close to the vessel wall is the smallest value. Mean velocity within the cross section is often measured [42].

1.2.1.5 Shear Stress

When blood is running along a blood vessel that forms a solid boundary, a shear stress will occur. The blood velocity at the vessel wall is dictated to be zero due to the no-slip boundary condition [43]. For Newtonian fluids under laminar conditions, the shear stress is proportional to the flow velocity gradient adjacent to the wall. According to the simple Hagen–Poiseuille equation, the shear stress is directly proportional to the blood flow rate, while inversely proportional to the diameter of the blood vessel [44,45].

1.2.2 Haemodynamic Parameters and Blood Vascular Disorders

Many studies indicate the relationship between haemodynamic information and local vascular disorders [6,7,46–50], like IAs and stenosis. Haemodynamic information is believed to be one of the most crucial factors affecting the initiation, development, growth, and rupture of IAs [47,50–53]. Therefore, the simulation of local aneurysmal haemodynamics should be carried out with adequate accuracy, as it helps to imply the aneurysm status. Moreover, the post-treatment aneurysmal haemodynamic information can also be useful information in the evaluation of aneurysm healing progress, as well as in the assessment of device treatment effects.

1.3 Literature Review

1.3.1 Implications of Haemodynamics on Intracranial Vascular Disorders and their Treatment

Many studies have shown the association between haemodynamic information and vascular disorders [54–57]. Especially saccular intracranial aneurysms that generally occur at arterial curves and bifurcations in the circle of Willis, show strong implications of a critical role for haemodynamics in such vascular geometry [6]. The haemodynamic index known as the gradient oscillatory number (GON) has been found to be closely associated with the generation of aneurysms [51]. Low wall shear stress (WSS) on the aneurysm wall is reported as a potential risk factor in aneurysm rupture, by the comparison of haemodynamic parameters between unruptured and ruptured IAs [47].

In contrast, reduction of inflow jet, energy loss (EL), volume flow rate, and WSS are found to be favourable haemodynamic parameters that indicate successful IA treatments [58–62]. The treatment of IAs with FD stents pursues a fast aneurysm occlusion, which is regarded as a sign of successful treatment. The occlusion time can be predicted by post-treatment aneurysmal haemodynamics; lower velocity, inflow rate, and shear rate are reported to be associated with a fast aneurysm occlusion [63].

1.3.2 Impact of Morphology Difference on Haemodynamic Information

Many studies have indicated that aneurysmal morphological differences might lead to haemodynamic variations [64,65]. Aneurysm morphologies of different aspect ratio (AR) are found to have different haemodynamic parameters, like inflow rate, time-averaged WSS, relative residence time (RRT), and oscillatory shear index (OSI) [66]. Investigation have shown that aneurysm AR, together with size ratio, are correlated to the EL when the flow running across the aneurysm. EL is a parameter believed to be able to reveal the potential tendency of aneurysm rupture, and increasing EL indicates higher risk of aneurysm rupture compared to decreasing EL [50,59,67,68].

Besides the aneurysm morphology, the position of an aneurysm and the parent vessel geometry can also influence the intra-aneurysmal haemodynamics; the presence of stenosis upstream of an aneurysm may lead to increased WSS on the aneurysm surface [69]. Aneurysmal haemodynamics are also found to be noticeably affected by different morphological combinations of aneurysm and parent artery curvatures, along with the aneurysm located at different positions [70]. By comparing the simulated flow in aneurysms respectively located at straight vessels and curved vessels, the flow patterns are confirmed to follow fundamentally different haemodynamics rules – shear-driven versus inertia-driven flow patterns [6].

1.3.3 Haemodynamic Studies

Studies using different methods to study the vascular haemodynamcis have been performed in the past. Raschi *et al.* studied the haemodynamic information in a growing patient-specific intracranial aneurysm by comparing the particle imaging velocimetry (PIV) and computational fluid dynamics (CFD) results [71]. Van Ooij *et al.*

studied the flow pattern in a patient-specific aneurysm with CFD, PIV, and phase-contrast magnetic resonance imaging (PCMRI) [72–75]. Bouillit *et al.* observed the flow pattern and velocity reduction in an idealised sidewall aneurysm before and after three commercial FD stent deployments, using both PIV and CFD [76–78]. With these research studies showing the agreement and disagreement between various methods, the comparison of aneurysmal flows with modifications resulting from FD stent interventions, for patient-specific IAs, have rarely been taken into consideration.

1.3.4 Modelling of FD Stents in Haemodynamic Simulation

Many simulations of FD stent treatment use porous medium (PM) method, as it can markedly improve the computational efficiency. In contrast to modelling the FD stent with fine meshes, which requires a high-resolution spatial discretisation around the stent's thin wires, PM-FD models mimic the resistance effect of an FD stent with parameters that characterise a PM, such as permeability (k) and inertial resistance factor (C_2) [79–82]. A number of studies have been performed to understand the correlation between the PM-FD stent and the fine-mesh FD stent model [58,79,80,83–87]. To obtain the PM model parameters that would be similar to an FD, Augsburger et al. created a FD test model, which had a geometry similar to the commercially available *Silk* FD stent, and derived k and C_2 values for the test model's PM analogue. Simulation of FD treatment results, using a PM model with *Silk* properties, also shown tendencies consistent with clinical results after treatment with *Silk* stent [58].

1.4 Research Objectives

Studies of haemodynamic simulation contribute to the understanding of aneurysmal flow dynamics and FD stent treatment efficacy. However, many of studies to date lack clarification and justification of the validity of simulation results, and, furthermore, published simulation studies remain inconclusive for PM modelling in the investigation of flow-diversion efficacy.

1.4.1 Shortcomings of Current Aneurysm Haemodynamic Studies

Further contributions can be made to the following aspects:

First, the accuracy of simulation results would be drastically compromised when the simulation was not performed following a rigorous protocol or lacked discussion of validity (*e.g.* the precision of model geometry reconstruction, the reasonableness of parameter settings, the consistency in the recurrence of circulation environment, *etc.*). Despite the fact that hundreds of IA simulation studies with/without FD stents have been published, few of them have sought to clarify their results' validity, via comparison with the real fluid environment *in vivo* or *in vitro*. Those accuracy-related discussions become particularly crucial, and cannot be avoided in the haemodynamic studies of any 'patient-specific' cases.

In addition, for most simulations in which a model FD stent is needed, there was a failure to calibrate the model FD stent's properties to match the stent that was represented, due to the neglect of the diversity in possible FD stent structures. Among different types of model FD stents, the PM model is one of the most commonly adopted models, as it can save computational time, as well as relieve the burden of performing a virtual stent deployment simulation. However, many simulations using a PM model failed to consider the drastic consequences resulting from different stent wire configurations. Instead, the only parameter setting used in their studies were a set of parameters derived from a *Silk* stent many years ago by Augsburger, *et al.* [79]. As these model FD stents ignored the importance of calibrating the parameter settings to the match the represented FD stents, the simulation of flow-diversion effects could not provide accurate predictions.

1.4.2 Objectives of this Thesis

In this thesis I seek to examine the accuracy and variation of parameters in haemodynamic simulations for an aneurysm and its flow-diversion treatment. To meet this need, efforts have been made in the following aspects:

(1) studies to explore the accuracy of CFD predictions of aneurysmal haemodynamics within a set of patient-specific cases, before and after FD treatment, by comparing to experimental methods (*i.e.* PIV, PCMRI, *etc.*);

(2) parametric studies to calibrate the PM model FD stents to different treatment modes using commercially available devices (*i.e.* the single *Silk+*, *PED*, *FRED*, as well as

several multiple stent deployment scenarios), thereby quantifying the sensitivity of the flow-diversion efficacy to the stent configurations.

With these studies, I expect to discover the simulation parameters and morphologic characteristics that may affect the credibility of aneurysm haemodynamic simulations, and, furthermore, provide future model FD studies a set of parameters after calibration to a variety of treatment modes.

1.5 Thesis Contents

The contents of this thesis are outlined as follows:

- Chapter 1: an introduction of this study's background, a literature review of the relevant publications, and a proposal of research objectives of this thesis;
- Chapter 2: introductions of the materials and methods to be applied in the following chapters;
- Chapter 3: an accuracy assessment of CFD simulations by comparing the aneurysmal haemodynamic results obtained with experimental methods (PIV and PCMRI), using a patient-specific aneurysm model;
- Chapter 4: an accuracy assessment of CFD simulations by comparing aneurysmal haemodynamic results obtained with PIV experiments, before and after FD stent treatment of a patient-specific aneurysm model; further, this chapter also involves the validation of a PM stent modelling;
- Chapter 5: an investigation of the impact on aneurysmal haemodynamics of variation of PM model thickness, when the PM permeation parameters are compensated to represent the same resistance;
- Chapter 6: a calibration of PM stent models to match various commercially available FD stents for the study of flow-diversion efficacies;
- Chapter 7: a conclusion of this study and the outlook beyond the content in this thesis.

Chapter 2

Materials and Methods

2.1 Modelling of Aneurysm Geometries

2.1.1 Idealised Aneurysm Geometries

Idealised models are usually established in studies of aneurysmal fluid flows to focus on the investigation of fluid variations that result from a specific morphological feature, as the idealised model can be designed to represent a vascular disorder from a comprehensive perspective, concerning different morphological scenarios of combination with its parent artery and at different severities of the disease [70,88,89].

For observation of the treatment efficacy of FD stent models with different wire structures, using idealised aneurysm models can eliminate undesired morphological factors that may have impact on the flow-diversion effect, thereby providing a simple fluid environment to achieve a pure evaluation of the stent wire structures [90,91].

Idealised aneurysm geometries can be created with computer-aided design (CAD) software tools. In this thesis, idealised models constructed using a commercial CAD tool, Pro/ENGINEER (Wildfire 5.0, PTC, USA), were employed in two scenarios. One is a saccular aneurysm with an upstream stenosis at different locations and severities (refer to Section 2.4 and Appendix I for detailed information), while the other is a straight tube with various FD stents placed in it (refer to Section 6.2.3 for detailed information).

2.1.2 Realistic Aneurysm Geometries

2.1.2.1 Data acquisition

Realistic aneurysms, also known as patient-specific aneurysms, can be detected by medical imaging techniques, like digital subtraction angiography (DSA), computer tomography angiography (CTA), and magnetic resonance angiography (MRA). The shape of the patient-specific aneurysm scanned by these approaches is usually stored as a series of slice-by-slice two-dimensional (2D) images in the digital imaging and communications in medicine (DICOM) format, which can then be reconstructed into three-dimensional (3D) geometries using either commercial or open-source image processing packages, *e.g.* OsiriX (Pixmeo SARL, Switzerland), MIMICS (Materialise, Belgium) and a vascular modelling toolkit (VMTK, http://www.vmtk.org/). This process involves image segmentation and 3D reconstruction, during which 2D contours showing the cross-section shapes represented by the pixel greyscales are first generated and then reconstructed into a 3D geometry based upon a contour interpolation strategy. Three patient-specific aneurysms were employed in this thesis (refer to Section 3.2.1, 4.2.1, 5.2.1, and 6.2.1 for detailed information).

2.1.2.2 In silico aneurysm model

Based on the slice-by-slice scans from clinical data, image segmentation and 3D reconstruction will be performed to obtain an in silico aneurysm model, using a combination of several computer software tools. The reconstructed geometry can then be stored as a surface model in STL format, which was assumed to have the same morphology as the patient-specific aneurysm measured obtained from medical imaging techniques.

To be further employed in numerical simulation, this 3D virtual model needs to be prepared as a computational model for fluid calculation, which is the meshing process. The entire fluid zone would be discretised into numerous tiny elements (tetrahedron, hexahedron, pyramid, polyhedron, *etc.*), through which the calculation of fluid properties can be transmitted between inlets and outlets.

2.1.2.3 *In vitro* aneurysm phantom

To meet the requirements for a physical experiment intended to study the fluid flow movements in aneurysms, an *in vitro* model should be created based on the 3D virtual models. In this thesis, patient-specific aneurysms were cast into silicone block models (refer to Section 3.2.1.1 and 4.2.1 for detailed information) with their aneurysm moulds obtained by using a 3D printing technique.

During the process of *in vitro* model manufacture, unexpected errors would usually happen due to the limitation in 3D printing resolution. To maintain fine similarity between computational model and physical model, a microscopic computed tomography (microCT) scan can be adopted to precisely capture the morphology of the physical model, which could later assist the reconstruction of a 3D geometry that has the same morphological details as the physical model.

To implement the microCT scanning, key procedures included: (1) the emitted X-rays first travelled through the model and were then recorded by a detector; (2) an X-ray projection image was then generated according to the X-rays transmitted to the detector; (3) a series of projection images was generated while the silicone phantom was rotating around; (4) the projection images were then processed into a series of 2D reconstructed images, which were known as the model cross sections, showing the internal structures of the scanned plane, and those images were stored in DICOM format (refer to Section 3.2.1.2 for detailed information).

2.2 Modelling of Flow-Diverting Stents

Three approaches of FD stent modelling that are suitable to be selected to meet different research purposes are introduced here, which are idealised FD stent model, porous medium (PM) stent model, and virtual stent deployment (VSD).

2.2.1 Idealised FD Stent Model

An idealised FD stent model is commonly used in the investigation of flow-diversion efficacy with different wire structures and the optimisation of existing wire structures. The model can be designed as a fully-resolved wire mesh in flat or curved planes [90], or a fully-resolved tubular wire mesh [91], with stent structures of various wire diameter, wire numbers, wire shape, layer of wire, *etc.*, thereby resulting in different porosities and pore densities.

Based on the features of several commonly used commercial FD stents on the market, idealised tubular FD stent models are created in this thesis to obtain the flow resistance created by each of them (refer to Section 6.2.2 for detailed information).

2.2.2 Porous Medium (PM) Stent Model

When a FD stent is modelled as a PM model, the entire stent model is regarded as whole body, without fully-resolved individual wires. This modelling approach can markedly improve the computational efficiency, as it avoids the difficulties that may arise in the process of fluid zone discretisation around thin wires, thereby releasing the burden on the flow calculation. In contrast to modelling the FD stent with fully-resolved fine meshes, PM models mimic the resistance effect of an FD stent with adjustment of parameters that characterise a PM. PM stent models were employed in Chapter 4, 5, and 6 in this thesis.

2.2.2.1 Porous medium and its properties

A porous medium (PM), also known as a porous material, is a kind of material that contains pores. The skeletal material of a PM is often a solid material in the structure of a frame or a matrix, while the pores inside the skeletor are commonly filled with a fluid.

Many properties can specifically characterise a PM, like its permeability (*k*), tensile strength, and electrical conductivity, but these may different for the respective constituents of a PM and its porosity and pore structures. The continuity of pores between the solid frame also varies in each PM; however, how much of the pore spaces can access the flow running through the PM is determined by the effective porosity excluding those closed pores.

To resolve the fluid flow through a PM, problems should respectively be discussed under different scales [92,93]. At the micro-scale, also known as the pore-scale, the fluid moves through only a few small pores—the fluid-filled spaces— and is resolved using conventional fluid mechanics approaches. However, at the macro-scale, which considers a wider field including a large number of pores, the conventional fluid mechanics approach can no longer be applied to such sophisticated flow movement, especially for the complex spatial resolution of the PM structure [94]. Therefore, over a representative elementary volume, a volume-averaging method is adopted to convert the micro-scale properties into macro-scale properties, like the intrinsic permeability (*k*), to describe the characteristic of the PM [93,94].

In the macro-scale, the intrinsic *k* determines the capability of a PM to transmit fluid. The *k*, together with the density and the viscosity of the fluid, influences the hydraulic conductivity of a PM for a single-phase flow. As a second-order tensor with nine components, as shown below, ***k*** represents permeabilities in different directions [94].

$$\boldsymbol{k} = \begin{bmatrix} k_{xx} & k_{xy} & k_{xz} \\ k_{yx} & k_{yy} & k_{yz} \\ k_{zx} & k_{zy} & k_{zz} \end{bmatrix} \mathrm{m}^2 \tag{2-1}$$

The only factor to determine the intrinsic k is the structure of the PM; depends on whether the PM frame is isotropic or anisotropic, the k in different directions can be either same or not.

2.2.2.2 Laws for fluid flowing through a PM

Due to the different properties of each PM, as well as specific properties of the fluid, a flow across the PM varies in both the behaviour when flowing through the PM and the amount of fluid that can pass through the PM.

The fluid flowing through the PM in macro-scale follows the momentum balance equations. Darcy's law and the Darcy–Forchheimer law, both obtained experimentally, can be used to respectively describe the flow through a PM in low or high velocity [92,93,95–98].

Darcy's law describes the proportional relationship between the discharge rate of a single-phase fluid through a PM, the pressure change across the certain distance, and the viscosity of the fluid, as shown in the equation below.

$$Q = -\frac{kA(p_b - p_a)}{\mu L}, \tag{2-2}$$

where Q is the total discharged volume of fluid per time (m^3/s), k is the intrinsic permeability (m^2), A is the cross-sectional area (m^2), p_a and p_b are the pressure at each position (Pa), μ is the fluid viscosity (Pa • s), and L is the length of the distance between two positions where the pressures are measured (m).

Therefore, the discharge per unit area per time can be deduced as:

$$\boldsymbol{q} = -\frac{\boldsymbol{k}}{\mu} \boldsymbol{\nabla} p, \tag{2-3}$$

where $\boldsymbol{q}$ is the Darcy flux (m/s), and $\boldsymbol{\nabla} p$ is the vector of pressure gradient (Pa/m).

According the equation, Darcy's law explains some features of fluid flowing through the PM: 1) it is the pressure gradient over a distance that governs the flow across a PM; 2) the flow moves from high pressure to low pressure areas; 3) higher pressure difference leads to higher discharge rate; 4) the discharge rate varies with respect to different structures of PM.

However, Darcy's law only applies to slow flow. Experimental observations indicate the validity of Darcy's law for flow with Reynolds number (Re) less than 10. For flow in PM with Re larger than 10, the enhanced influence on flow of inertial effects can become crucial. Therefore, as an additional form of Darcy's law, the Forchheimer law, as shown in the equation below, including an inertial term added to the original equation, is capable to account for the non-linear phenomenon of the pressure change under different fluid discharge rate [94,99].

The coefficient for the Forchheimer term is strongly dependent on the regime of the flow. As the discharge rate of fluid increases, the coefficient needs to be calibrated to reflect the experimental observations of the inertial effects [94].

2.2.2.3 PM model FD stent in numerical simulation

In numerical simulation of the fluid dynamics, a FD stent can be modelled as a PM layer, as both of them have the same feature of creating a resistance to the flow, and allow only a portion of the fluid to flow through. The PM layer can be modelled by adding a momentum source term to the continuity and Navier–Stokes equations, as shown in the equation below, at specific elements in the volumetric mesh of the fluid zone [79,81].

$$S_i = -\left(\frac{\mu}{k} v_i + C_2 \frac{1}{2} \rho |\boldsymbol{v}| v_i\right), \tag{2-4}$$

where k is isotropic permeability, C_2 is inertial resistance coefficient, i stands for the coordinate x, y, or z, v is velocity, μ is viscosity, and ρ is density.

The pressure drop, which reflects the resistance to the flow through the PM, can is calculated as

$$\Delta p_i = -S_i \, \Delta e_i, \tag{2-5}$$

where Δp_i is the pressure drop across the PM, and Δe is the thickness of the porous medium.

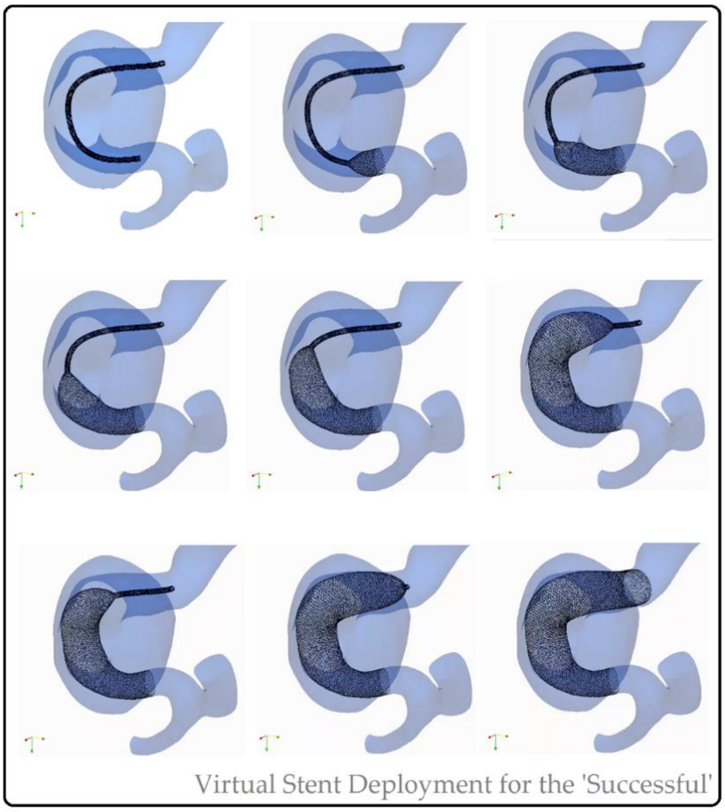

Figure 2-1 FD stent deployment process of a successfully-treated aneurysm case. (From top-left to bottom-right: stent vertices fully crimped to fully expanded) [101]

Therefore, for a PM model FD stent with a given thickness, the *k* and C_2 parameters can be respectively derived and defined to create certain flow resistance.

2.2.3 Virtual Stent Deployment (VSD)

To simulate the actual FD stent deployment procedure, a FD stent model with fully-resolved wire structures can be generated using different virtual stent deployment (VSD) methods [100–104]. VSD of commercially available FD stents can be performed to mimic the stent structures in a patient-specific aneurysm artery, from the initially crimped condition to the expanded status within the parent artery (see Figure 2-1 [101]).

2.3 Fluid Flow Studies

2.3.1 Computational Fluid Dynamics (CFD)

Computational fluid dynamics (CFD), based on the Navier–Stokes equations, is a combination of the use of applied mathematics, physics, numerical analysis and data structures in computational methods, in order to solve problems in fluid mechanics. In the biomedical engineering field, CFD calculation is commonly used to clarify the local haemodynamics in human blood vessels [105,106]. With the scanned data from clinical imaging techniques, a realistic 3D model of the human vascular system can be reconstructed. Thus, the fluid behaviour in such vascular systems can be resolved using CFD while the assumption of blood-analogue-fluid is adopted, as well as the boundary conditions to be specified as for the realistic blood flow environment.

The process of this numerical analysis of fluid flow involves the representation of partial differential equations (PDE) in the form of discrete algebraic equations. Three popular discretisation methods in CFD are respectively finite volume method (FVM), finite element method (FEM), and finite difference method (FDM). In the FVM, volume integrals in a PDE that contain a divergence term are converted to surface integrals, using the divergence theorem (also known as Gauss's theorem). These divergence terms are then evaluated as fluxes at the surfaces of each finite volume. These methods are conservative, as the flux entering a given volume is identical to that leaving the adjacent volume.

The FVM is often applied to the simulation of high-Re turbulent flows and source term dominated flows, as it requires less computer memory and shorter simulation time compared to FEM. While the approach of FEM is often used in structural analysis of solids or fluids, FVM offers great supports for unstructured meshes, which suits the description of patient-specific arterial flows [107].

CFD simulation software tool Ansys (Canonsburg, USA) is based on FVM, in which the discretised fluid domain is to be solved with Navier–Stokes equations which describes the conservation of fluid mass, momentum, and energy. The general form of the steady state Navier–Stokes equation is

$$\rho u_j \frac{\partial u_i}{\partial x_j} = -\frac{\partial P}{\partial x_i} + \frac{\partial}{\partial x_j}\left[\mu\left(\frac{\partial u_i}{\partial x_j} + \frac{\partial u_j}{\partial x_i}\right)\right] + S_i , \qquad (2\text{-}6)$$

where ρ represents the density, P is the static pressure, u_i and u_j are velocity components and μ is the dynamic viscosity. S_i is the source term of the momentum equation, which can be used to account for the pressure drop through a certain kind of material.

CFD simulations were employed in Chapter 3, 4, 5, and 6 in this thesis.

2.3.2 Particle Image Velocimetry (PIV)

Particle imaging velocimetry (PIV) is non-intrusive optical method used to investigate the instantaneous velocity vector field of the fluid flows. By analysing the displacement of a great number of particles in the fluid that precisely trace the flow, the flow movement can be accurately resolved [108]. The basic components in a standard planar PIV system include a laser source, the light-sheet-forming optics, the seeding particles for tracing the fluid movement, a high-speed still camera to capture images of the particles, the image digitisation hardware, and a computer for the storage and analysis of data.

PIV has advantages in many aspects. As a non-intrusive method, if the seeding particles are reasonably adopted and added in to the fluid, the distortion of the fluid flow can be negligible [109]. Moreover, the use of optical measurement eliminates the error that may induced by any intrusive flow measurement devices. In addition, with adequate resolution of the camera, precise analysis of the velocity vector field can be achieved. However, planar PIV is not capable of measuring the velocity components in the z axis. The velocity in such direction is normally not only missed, they may influence the analysis of data in x and y axis due to parallax. This limitation is possible to be avoided by performing stereoscopic PIV measurement, which requires two high-speed cameras tracing the particle movement from different angles.

PIV experiments were employed in Chapter 3 and 4 in this thesis.

2.3.3 Phase-Contrast Magnetic Resonance Imaging (PCMRI)

Magnetic resonance imaging (MRI) is a non-invasive imaging method commonly used in clinics that produces detailed 3D images of human anatomical information, without the use of damaging radiation. It is often used in the detection and diagnosis of diseases, as well as in post-treatment monitoring. This method is based on technology that stimulates and detects the changes in the direction of protons, which are found in the water compositions in the human body.

Phase-contrast MRI (PCMRI) is a method to obtain quantitative information on blood flow in the human body, which can be operated both under holding breath or during normal respiration [110]. In PCMRI, a pair of bipolar gradients is used, which is able to create phase shifts of moving spins. By measuring the phase change, velocity of flow can be calculated, based on the proportional correlation between the spin velocities and their phase shifts. Therefore, with PCMRI, the 3D or 4D (plus time, for the time-resolved PCMRI) velocity vector field of blood flows in the human body can be measured [111].

The most precise measurement of flow can be achieved when the target plane of imaging is perpendicular to the vessel of interest, while the flow encoding is set as the flow across the plane. However, due to technique limitations, some errors are difficult to avoid in PCMRI: for example, incorrectly matched encoding velocity, inadequate temporal and spatial resolution, and errors in phase offset [110].

PCMRI measurements were employed in Chapter 3 in this thesis.

2.4 An Application of CFD Simulation of Flows in Idealised Aneurysm Models

CFD simulations were employed in every study in this thesis. A preliminary simulation was first performed with an idealised aneurysm located in parent artery with complicated morphologies. Through this test, basic methodologies for CFD simulation were confirmed, while the impact on aneurysmal flow pattern affected by morphological factors were also observed.

2.4.1 Introduction

The purpose of this application was to investigate the impact of upstream stenosis morphology on aneurysmal haemodynamics, by performing CFD simulations with idealised straight-vessel and curved-vessel aneurysm models. Specific attention is paid to different severity of stenosis, various distance between stenosis and aneurysm, and curvatures of the parent arteries. Results of the straight-vessel models are shown herein (details about the curved-vessel models can be found in Appendix I).

2.4.2 Materials and Methods

2.4.2.1 Modelling

Idealised models were created using CAD software (Pro/ENGINEER Wildfire 4.0, PTC, USA). Morphological parameters for straight vessels with stenosis and an aneurysm [112] are as follows. The length of the vessel is 140 mm, which assures enough space for the flow to be fully developed from the inlet. The aneurysm, with a diameter of 8 mm, is located at the centre of the vessel. Positions of the stenosis vary between distances of 1 mm, 10 mm, and 30 mm to the aneurysm. The diameter of the parent artery is 4 mm and the diameter of stenosis area varies with respect to the level of stenosis, as shown in Figure 2-2.

The degree of stenosis is calculated by the equation below:

$$\text{Stenosis Ratio} = (D_1 - D_2)/D_1 \times 100\%, \tag{2-7}$$

where D_1 is the normal parent artery diameter and D_2 is the minimal diameter at the stenosis—the narrowest position [113]. A variety of degrees of stenosis were studied to represent mild stenosis (30%) and moderate stenosis (50%) [113].

2.4.2.2 Meshing

Since mesh quality is a critical to the simulation accuracy, the meshes for all cases were generated under the same protocol. The entire fluid zone was discretised into

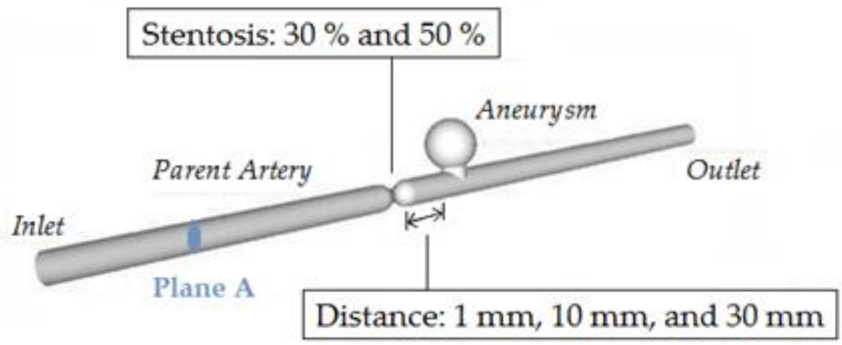

Figure 2-2 Sketch of geometry with stenosis and aneurysm in a straight vessel

tetrahedral elements, with three prism boundary layers. The maximal element size was defined as the smallest vessel diameter (D_2) divided by ten, in order to ensure that the fluid zone was discretised into at least ten elements for even the narrowest cross-section. The entire fluid domain was discretised into about one to two million elements across different cases. A mesh dependency test was performed to ensure the simulation accuracy.

2.4.2.3 Fluid Simulation

Assumptions of Newtonian, incompressible fluid and laminar flow were determined for the fluid, with the density specified as 1050 kg/m^3 and the viscosity specified as 0.0035 Pa·s. A steady condition was applied for all simulations. Average velocity of 0.2 m/s was specified at the model inlet with a Re of 240, within the range of Re in intracranial arteries (from 110 to 850). With this setting, the simulation was in good consistency with the assumption of laminar flow in every grid within the fluid zone. A pressure boundary condition of 0 Pa was defined at the outlet. Stationary and no-slip conditions were set on the model walls. The calculation was performed using a commercial solver (Ansys Fluent, USA) based on FVM method.

2.4.3 Results

2.4.3.1 Flow pattern

Figure 2-3 displays the recirculation after different degrees of stenosis. The reattachment length was observed from the velocity vector plot on the centre plane along the axial direction (see Figure 2-3(a)). As the degree of stenosis increases, the reattachment occurs at the wall at an increasing axial distance from the stenosis. 3D streamlines were also examined which showed an identical trend to the reattaching

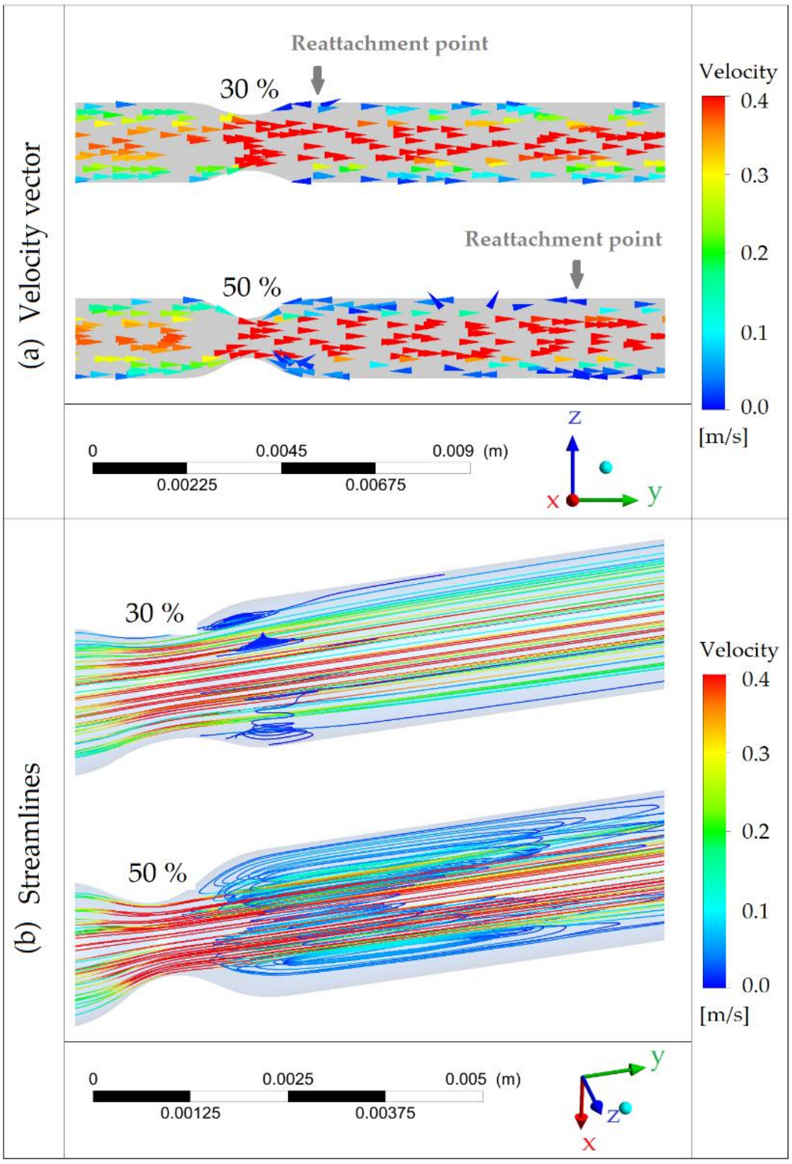

Figure 2-3 Reattachment point and recirculation of models with stenosis of different degrees (the direction of main flow is from left to right)

flow in the velocity vector plot (see Figure 2-3(b)). Figure 2-4 shows the aneurysmal flow pattern disrupted by the existence of the flow recirculation.

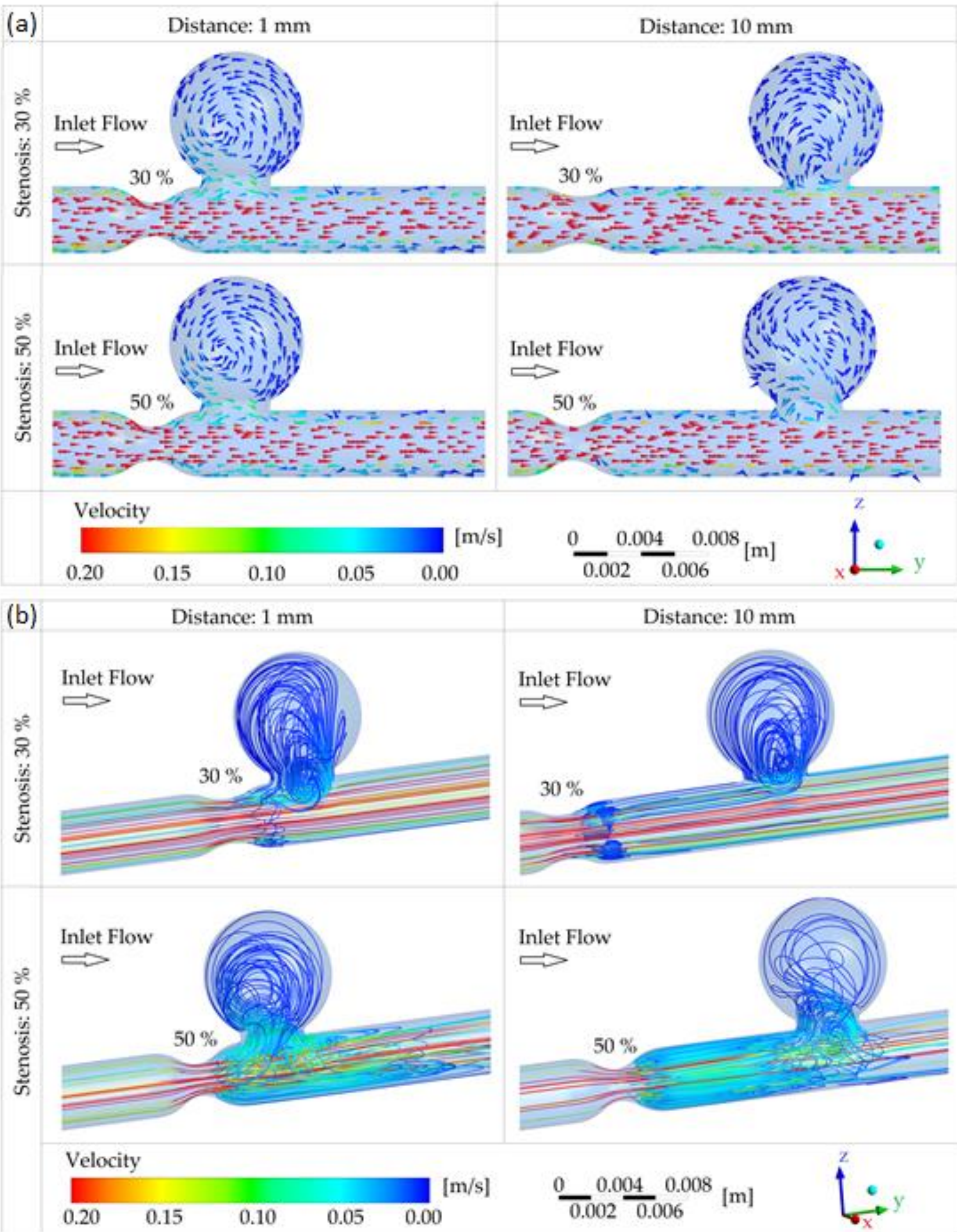

Figure 2-4 Flow pattern for aneurysms with pre-aneurysmal stenosis in different positions and stenosis levels: (a) velocity vector on centre plane (b) streamlines

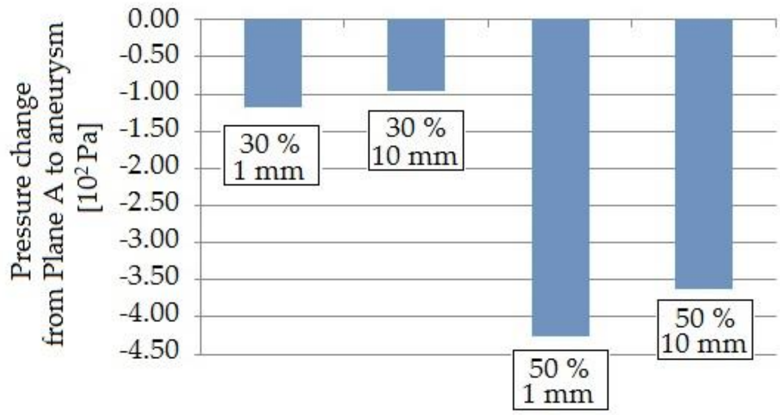

Figure 2-5 Intra-aneurysmal pressure (average value) change in straight vessel models (The label below each bar represents the characterised model, i.e. '30 % 1 mm' means model with 30% stenosis while the distance between stenosis and aneurysm is 1 mm.)

2.4.3.2 Pressure

Figure 2-5 shows the variation in pressure between aneurysm and Plane A (see Figure 2-2). For the same severity of stenosis, the pressure drop remains in a constant range of magnitude, while increased degree of the stenosis is observed to account for a greater pressure drop. When the severity of stenosis is 30 %, the aneurysmal pressure drop, which is calculated by the change between the average pressure of aneurysm and Plane A, is around 118 Pa. When the degree of stenosis increases to 50 %, the aneurysmal pressure drop rises to 426 Pa, indicating the pressure drop increased as much as 308 Pa resulting from a more severe stenosis. From the results, it demonstrated that the existence of stenosis has certainly influenced the aneurysmal pressure, mainly depending on the severity of the stenosis

2.4.4 Conclusion

This study implemented the simulation of idealised models with a certain shape and size of aneurysm on straight vessels with different degree of stenosis on various positions. Results indicate that the existence of stenosis and the consequent reattachment flow lead to various aneurysmal flow patterns, depending on morphological factors like the degree of stenosis and its distance to the downstream aneurysm.

Chapter 3

Haemodynamics in a Patient-Specific Intracranial Aneurysm Obtained from Experimental and Numerical Approaches: a Comparison between PIV, CFD, and PCMRI

3.1 Introduction

3.1.1 Background

Haemodynamics is considered to be a crucial factor affecting the initiation, growth and rupture of an intracranial aneurysm [114–116], therefore a number of methods are developed to investigate haemodynamic parameters for the estimation of aneurysm condition as well as the formation and treatment of this disease.

There are several commonly adopted methods: (1) particle image velocimetry (PIV), which is an optical method to visualise the flow movement in *in vitro* models [117,118]; (2) computational fluid dynamics (CFD), which is a numerical method to analyse problems with the involvement of fluid flows in virtual models [120]; (3) phase-contrast magnetic resonance imaging (PCMRI), which is a specific type of the medical imaging technique to primarily determine the vector field of flow velocities in the 3D fluid zone at different time frames [121,122]; this approach can be used in both *in vivo* and *in vitro* measurements.

3.1.2 Current Issue

Each method has its own advantages and limitations. Flow patterns in the same geometry obtained from PIV, CFD and PCMRI have rarely been compared, especially for complex flow behaviours that may occur in patient-specific aneurysms. However, this knowledge would be important to achieve an accurate analysis of the fluid flows, which is the foundation for further studies about aneurysmal haemodynamics with more advanced purposes.

3.1.3 Purpose

The purpose of this research is to compare the aneurysmal velocity vector field obtained from three different methods: PIV, CFD, and PCMRI. Through the agreements and disagreements in 2D velocity vector plane, 3D velocity streamlines, and quantitative velocity comparisons, this study aims to understand the power of each method to analyse the aneurysmal fluid flows.

3.2 Materials and Methods

3.2.1 Aneurysm Model

3.2.1.1 *In vitro* silicone phantom

This study was approved by the institutional review boards of Nagoya University and Iwata City Hospital in Japan (Ref 2010-1062-3), and the patient data was anonymised. A realistic aneurysm model was used in this research, which is a right basilar artery-superior cerebellar artery aneurysm of a 70-years-old female patient. The aneurysm was located at the bifurcation of basilar artery (BA), right posterior cerebral artery (RPCA), and left posterior cerebral artery (LPCA). The aneurysm was scanned on a 3T MR imaging scanner (Signa HDx 3T, GE) by using a 8-channel neurovascular array coil. 3D time-of-flight (TOF) MRA was performed with a scan resolution of 0.37×1.0×0.5 mm (0.37×0.37×0.5 with zero fill interpolation). Imaging parameters were set as following: TR/TE, 26.0/3.1 ms; flip angle, 20°; acquisition time, 5 minutes 39 seconds.

With the scanned data, an original stereolithography (STL) file of the blood vessel with aneurysm was reconstructed using commercial medical image processing software (OsiriX V5.8.1). With the original STL file, an *in vitro* model was manufactured by casting the aneurysm and its parent arteries into a silicone block model (R'Tech, Japan), as shown in Figure 3-1. Plane A located around the aneurysm neck was selected as the measurement plane to compare the haemodynamic results between PIV, CFD, and PCMRI.

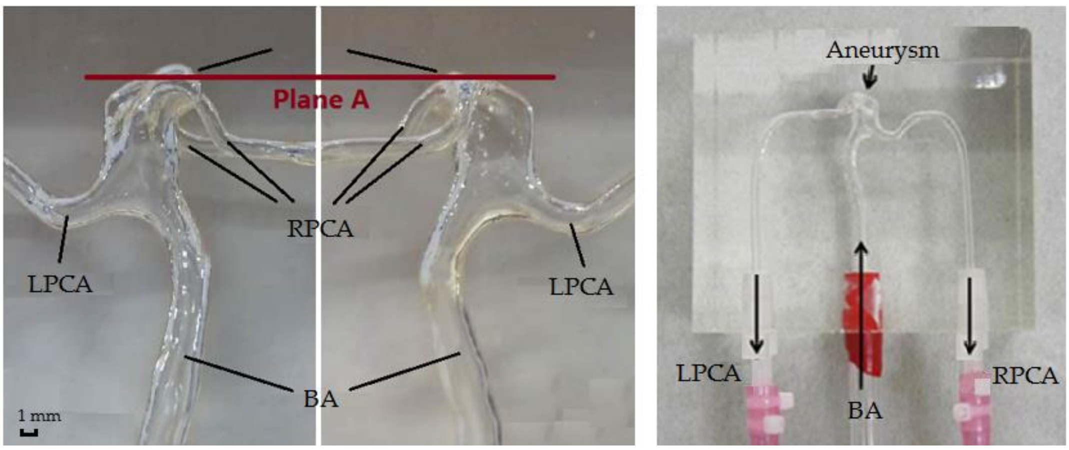

Figure 3-1 Silicone phantom of the patient-specific aneurysm: (a) back view (b) front view (c) silicone block

3.2.1.2 Reconstructed three-dimensional virtual model

Considering the morphological discrepancies that might be incurred during the fabrication process of the silicone model using 3D printing technique, the silicone model was scanned by a microCT scanner (ScanXmate-D180RSS270, Comscantec), as shown in Figure 3-2(a). While the silicone model was rotating around in the machine, a series of projection images were generated and then processed into a series of 2D cross-section images showing the internal structure of the silicone model at different heights, as shown in Figure 3-2(b). These cross-sectional images were stored as DICOM format for further processing. In order to capture the detailed morphological

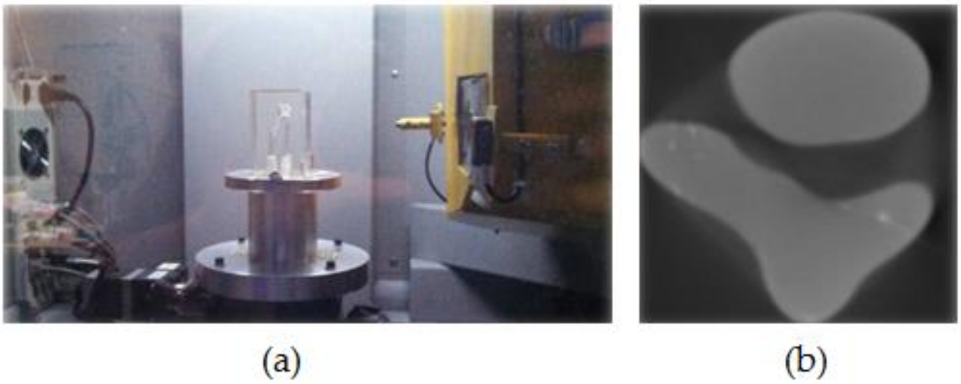

Figure 3-2 MicroCT scan: (a) scanning (b) two dimensional DICOM data

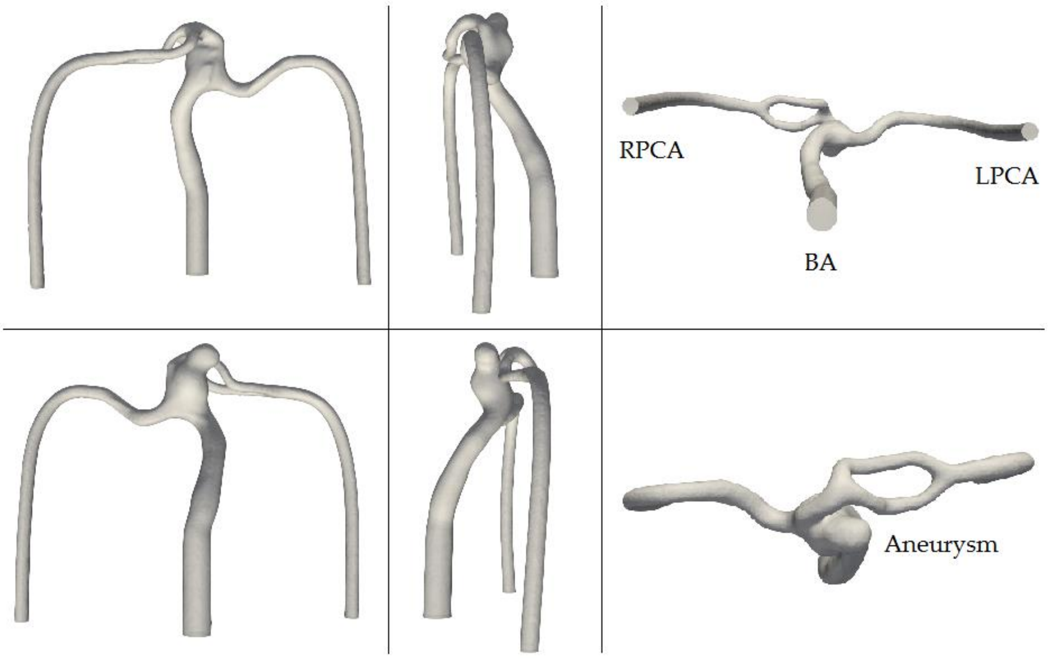

Figure 3-3 Reconstructed three-dimensional aneurysm model

characteristics, I adopted a resolution of 40 μm, so that even the narrowest area of the aneurysm model, which was approximately 1.4 mm, could be depicted by around 35 pixels.

Based on these slice-by-slice scans, image segmentation and the 3D reconstruction were performed using a combination of several computer software tools. The quality of all DICOM data was improved using the image-processing software ImageJ (https://imagej.net). First, image contrast was enhanced for all cross-section images and clearness of the boundaries between different media was improved; this contributed to an accurate segmentation. Second, all cross-section images went through a noise reducing process to modify the sudden change of brightness, as such spots might be caused by the dust in the silicone models. With the series of improved cross-section images, the lumen boundary was extracted and reconstructed into a 3D virtual model in STL format using commercial medical image processing software (OsiriX MD, Pixmeo SARL, Switzerland), as shown in Figure 3-3. After this process, the morphology of the silicone model and the geometry used for CFD simulation were considered to be equivalent.

3.2.2 Blood-Analogue Fluid (BAF) for PIV and PCMRI

Blood-analogue fluid (BAF) was created for the flow modelling in both PCMRI measurement and PIV experiment. Fluid properties that may affect its haemodynamic behaviours, like fluid density and viscosity, were specified to be as close as those of human blood, as shown in Table 3-1. To meet the fluid measurement requirements for each experimental approach, composition of the solution was slightly different. As an optical method, the refraction index of the BAF used in PIV was specifically controlled to match with the silicone model, so that the visualisation of flow movement would not be influenced by undesired refraction. Since the BAF for PIV and PCMRI was created separately, unavoidable differences existed in the solution properties within a reasonable range, with 8 and 14 % difference respectively for density and viscosity.

Table 3-1 Blood-analogue fluid in PCMRI and PIV

	PCMRI	PIV
Solution	Aqueous Glycerol	Glycerol and Aqueous NaI
Density [g/ml]	1.1	1.2
Dynamic Viscosity [mPa•s]	4.03	4.73
Refractive Index	-------------	1.46
Temperature [℃]	17	17

3.2.3 PIV Experimental Setup

The silicone aneurysm model was connected to a pump (NBL30PU, R'Tech, Japan) through tubes, with BAF running into the aneurysm model from BA as inlet and coming out from LPCA and RPCA as outlets [123]. A straight tube with 1-metre-length was added before the inlet of the silicone block, in order to provide enough distance for the inflow to be fully developed before entering the aneurysm [123]. Flow rate was generated by the pump at 290 mL/min, which is close to the average flow rate of human blood in BA. Three Coriolis flow meters (FD-SF1, Keyence Corporation, Japan) were connected into the circulation system to monitor the inlet and outlet flow rates, while valves were used to assist the adjustment of outlet flow rates for them to maintain the expected difference between RPCA and LPCA as 170 and 120 mL/min respectively. These target flow rates were obtained from clinical data. Seeding particles with the same density as the BAF were added into the BAF at low concentration: that way the movements of particles following the running BAF can be captured by the camera.

A high speed camera (FASTCAM SA3, Photron) with resolution of 17×17 μm was placed in front of the silicone block to acquire images of the particle movements on the measurement plane (plane A) illuminated by the 1 mm thick laser sheet, which was provided by Nd: YAG laser (DPSS laser system-532NM X 300MW, Edmund Optics) [123]. A series of 500 continuous images were imported into a PIV software application (Davis ver8.1, LaVision) for the analysis of the velocity vector field. The resolution of the interrogation window set in the post-processing was 64×64 pixels with 75 % overlapping.

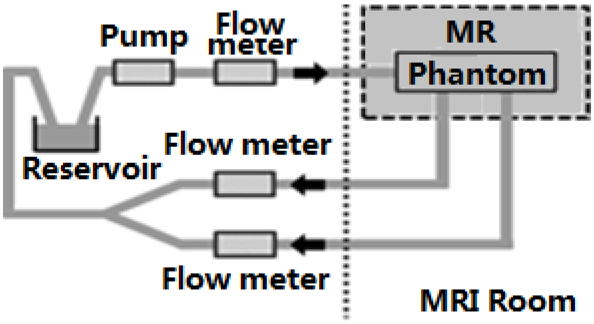

Figure 3-4 Sketch of the experimental system for PCMRI

3.2.4 PCMRI Measurement Setup

The same circulation system as PIV experiment was established for the PCMRI measurement, as shown in Figure 3-4, with BAF for PCMRI running at the same flow rates. 3D cine PCMRI was performed with a resolution of 0.5×0.5×1 mm. Imaging parameters were set as following: TR/TE, 7.8/3.88 ms; flip angle, 15°; acquisition time, 16 minutes 16 seconds.

Post-analysis of the magnetic resonance fluid dynamics (MRFD) was performed using the commercial software (Flova, R'Tech, Japan) to obtain haemodynamics in the 3D fluid zone. Images of the 4D-flow signal strength and the flow velocity were first loaded into the software as DICOM data, and the blood vessel wall was generated then based on the signal intensity of the 3D TOF MRA, using a marching-cube or region growing method. Velocities were computed with arbitrary spatial resolution after that, and meanwhile more haemodynamic parameters, like wall shear stress, OSI, *etc.*, were able to be displayed.

3.2.5 CFD Simulation Settings

With the reconstructed 3D aneurysm model, the computational grid was created for the entire fluid zone in tetrahedral and prism elements with three boundary layers using a commercial software (ICEM CFD, ANSYS, USA). To ensure the simulation accuracy, the quality and robustness of the computational grid was checked by performing a mesh dependency test, which indicated that the meshing scenario with total elements of 1.4 million was stable enough for an accurate simulation (see Figure 3-5).

The flow was assumed to be incompressible Newtonian fluid at steady state, with a laminar description. Boundary conditions were set to replicate the flow environment created in both PIV and PCMRI, as shown in Table 3-2. Blood density was specified as 1050 kg/m^3, while viscosity was 0.0035 Pa·s. As silicone model has negligible elasticity, the surface boundary condition for the computational model was set as rigid wall. The flow simulation was performed using a commercial solver (Fluent, Ansys, USA) with finite volume method.

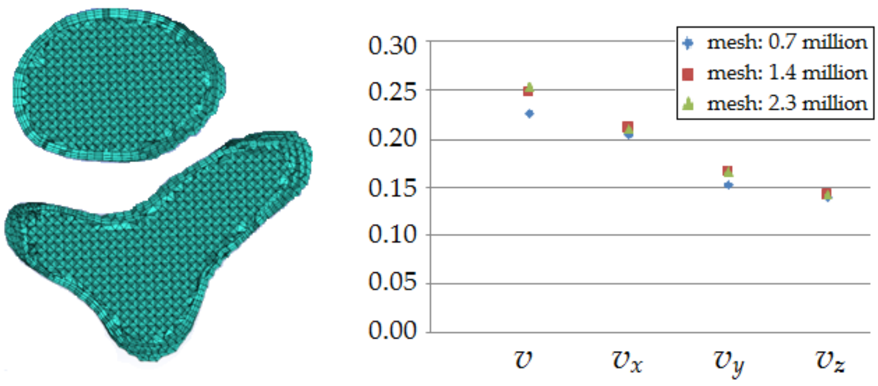

(a) (b)

Figure 3-5 Mesh elements on the measurement plane: (a) mesh elements on a cut plane of the case with 1.4 million mesh elements (b) velocity comparison on the cut plane for different mesh conditions (v is the velocity magnitude, while v_x, v_y, and v_z are the velocity components in X, Y, and Z axis, respectively)

Table 3-2 Fluid boundary conditions

	PIV	PCMRI	CFD
Boundary condition	Flow rate	Flow rate	Flow rate & Pressure
Inlet: BA flow rate [mL/min]	290	290	-----
Inlet: BA pressure [Pa]	-----	-----	0
Outlet: RPCA flow rate [mL/min]	170	170	170
Outlet: LPCA flow rate [mL/min]	120	120	120

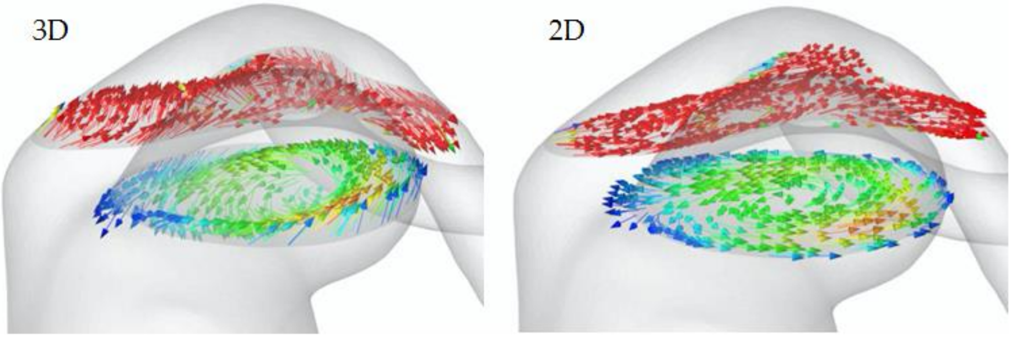

Figure 3-6 3D planar velocity vectors (left) and the in-plane projection of vectors (right)

3.2.6 Haemodynamic Characteristics

To compare with 2D velocities obtained from PIV experiment, a variable of 2Dvelocity was created in the post-processing of the CFD simulation (as equation 3-1 and 3-2). The projection of velocity vector on the measurement plane (plane A) was also generated for visualisation (see Figure 3-6).

$$\text{3D velocity magnitude} = \sqrt{\left(v_x^2 + v_y^2 + v_z^2\right)}, \quad (4\text{-}1)$$

$$\text{2D velocity magnitude} = \sqrt{\left(v_x^2 + v_y^2\right)}. \quad (4\text{-}2)$$

3.3 Results

3.3.1 Shape Comparison for Plane A: PIV, CFD and PCMRI

The location of plane A is around the aneurysm neck, as shown in Figure 3-1. Figure 3-7 shows the shapes of plane A measured by different methods, the ellipse on the left side indicates the shape of the aneurysm neck while the polygon on the right side is the cut plane in the outlet artery (RPCA). As can be seen from the figure, the shapes obtained from PIV and CFD are in good agreement in terms of both the shape and size. While the plane shape detected by PCMRI can depict the general morphology of the aneurysm neck and the outlet cut plane, it shows less similarity to that of PIV and CFD. Figure 3-7(c) shows an ellipse with larger size, especially in the top-right area where the neck plane almost reaches the junction area between the aneurysm and the

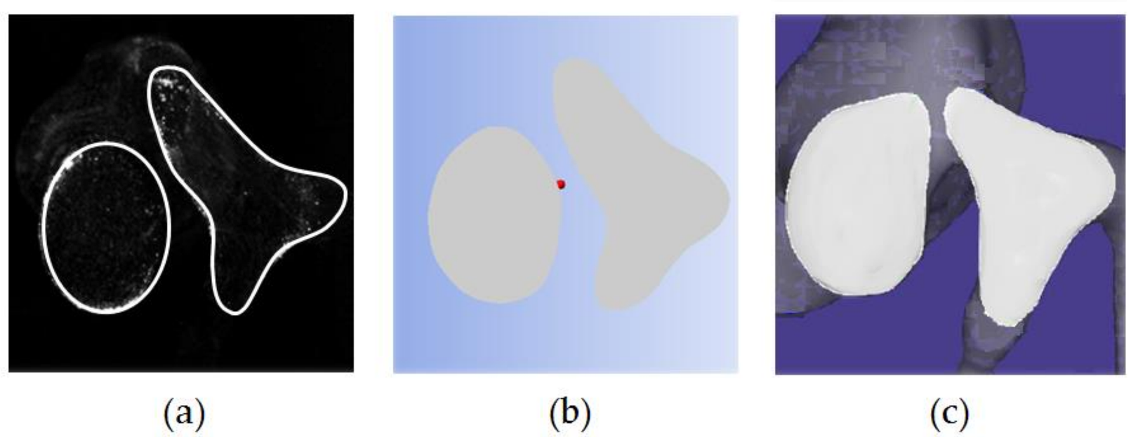

Figure 3-8 Shape of the target plane in different methods: (a) PIV (b) CFD (c) PCMRI

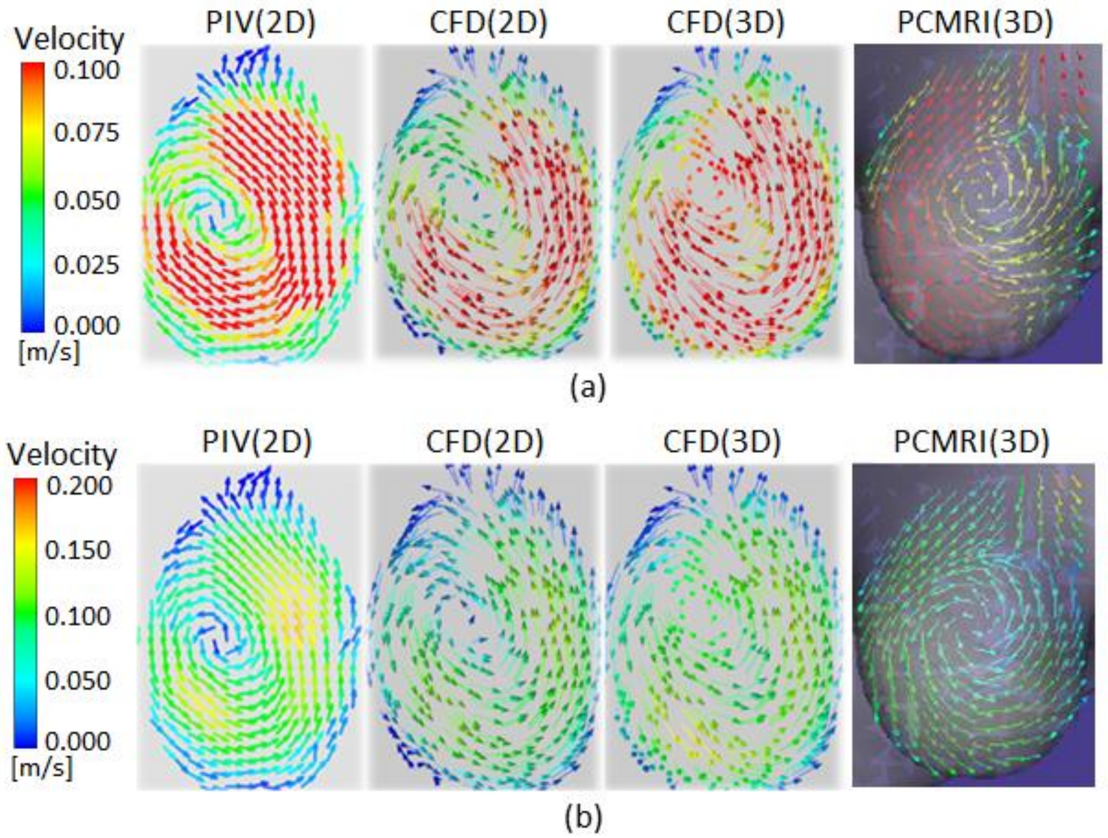

Figure 3-7 Comparison of velocity vector field on plane A between PIV, CFD and PCMRI results (results are from one set of measurements presented with different colours: (a) maximal velocity at 0.1 m/s (b) maximal velocity at 0.2 m/s)

bifurcation arteries. The ellipse on the left side was selected as the measurement plane for further velocity vector field comparisons.

3.3.2 2D Velocity Vector Comparison: PIV, CFD and PCMRI

From the comparison of 2D velocity vectors on the measurement plane in Figure 3-8, the velocity vector field obtained from PIV experiment and CFD simulation shows good agreement, in terms of both the flow pattern and velocity magnitude. A vortex appears at the centre with flow rotating in the anti-clockwise direction, and lower velocity is detected at the vortex centre comparing with the surrounding flow. When the flow rotates to the top area of this plane, it separates into different directions, forming a separation point. Velocity higher than 0.1 m/s is detected at the rotating flow around the vortex centre from both PIV and CFD; meanwhile, low velocity is also found at similar positions, i.e. the vortex centre, the bottom side close to the aneurysm wall, and the flow separation area.

For the velocity vector plane obtained from PCMRI in Figure 3-8, the flow pattern in the centre as an anti-clockwise rotation can still be captured, with higher velocity; however, the flow pattern close to the boundary shows some discrepancies. Obviously, compared to that of the PIV and CFD results, the position of the flow separation point moves to the upper-middle area on the right side, which is also the position of the dissimilarity found in the plane shape comparison.

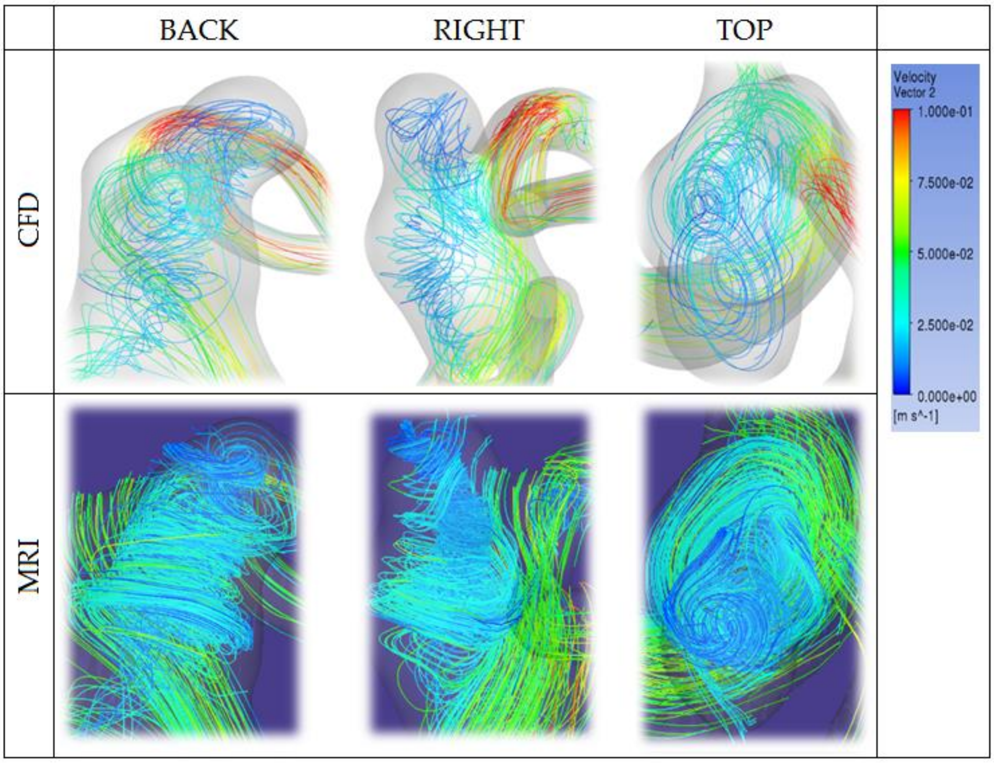

Figure 3-9 3D streamlines in the centre of the aneurysm obtained with CFD and PCMRI (displayed in various views)

3.3.3 3D Streamline Comparison: CFD and PCMRI

3D velocity streamlines in the aneurysm sac were visualised with results from both CFD and PCMRI, as shown in Figure 3-9. Although some dissimilarities exist around the model wall, the flow pattern in the centre of the 3D fluid zone shows good agreement between the prediction by CFD and the measurement by PCMRI, in terms of both the velocity magnitude and the position and direction of the vortex.

3.3.4 Quantitative Velocity Comparison: PIV, CFD and PCMRI

To further check the agreement between PIV and CFD, 2D velocity magnitude on a horizontal line on the measurement plane across the vortex was compared, as shown in Figure 3-10, which indicates good similarities. Besides, the maximal value and average value of different velocity components on the measurement plane were also compared between three methods, as shown in Figure 3-11, the velocity predicted by CFD shows higher values than that of PIV, followed by PCMRI. Moreover, difference between CFD and PIV ranges from 22 to 28 % for different velocity components, while that between CFD and PCMRI indicates a larger discrepancy for 32 to 41 % across different velocity components, as shown in Figure 3-12.

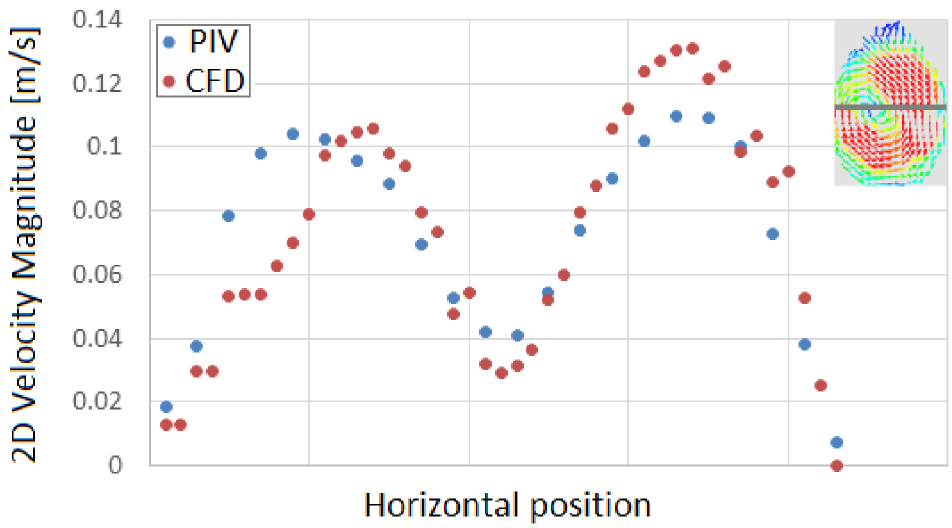

Figure 3-10 In-plane velocity magnitude comparison between PIV and CFD. The sketch at the top-right corner indicates the position of the line. The velocity is plotted from the left to the right edge on the line across the vortex.

809

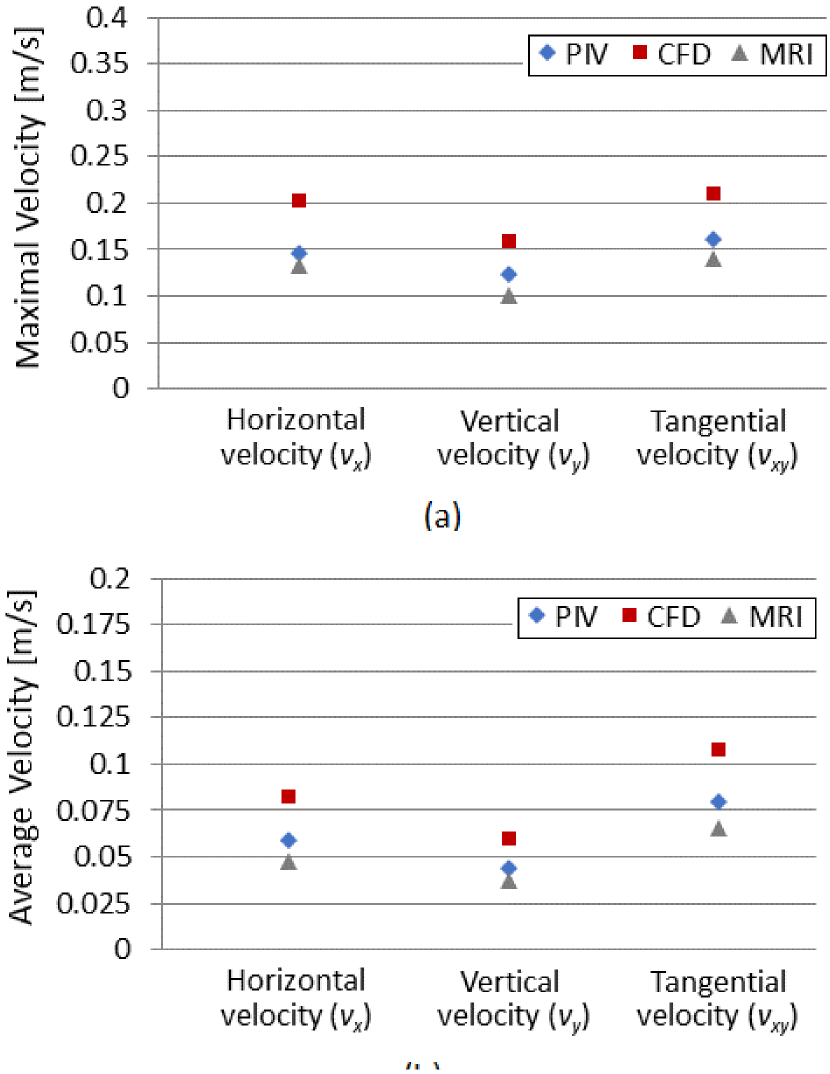

Figure 3-11 Quantitative comparison of velocity magnitude on the measurement plane: (a) maximal velocity (b) average velocity

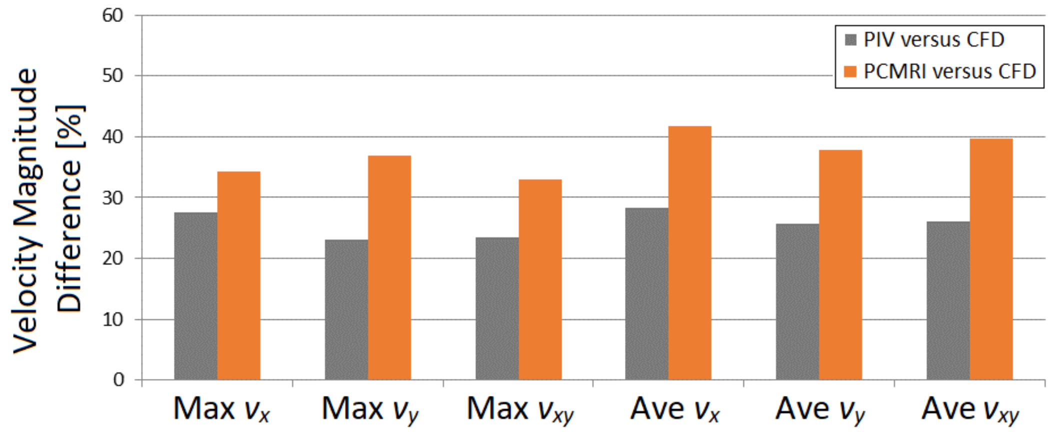

Figure 3-12 Velocity magnitude difference between CFD and PIV or PCMRI

3.4 Discussion

In this study, the velocity vector field in a patient-specific aneurysm model has been studied using different methods – PIV, CFD, and PCMRI, which are commonly adopted numerical and experimental approaches to obtain the fluid haemodynamics. Comparisons of 2D flow patterns and 3D streamlines between these methods have been performed, with a further quantitative check of velocity magnitude. Results with good similarities can be found in the 2D velocity vectors between PIV and CFD, as well as in the 3D flow pattern between PCMRI and CFD. Through the comparison, this study has revealed the characteristics of these methods – advantages and drawbacks – which could serve as useful knowledge and important references for future haemodynamic investigations using these methods. Moreover, CFD is widely used to study the difference in haemodynamic changes between successful and unsuccessful

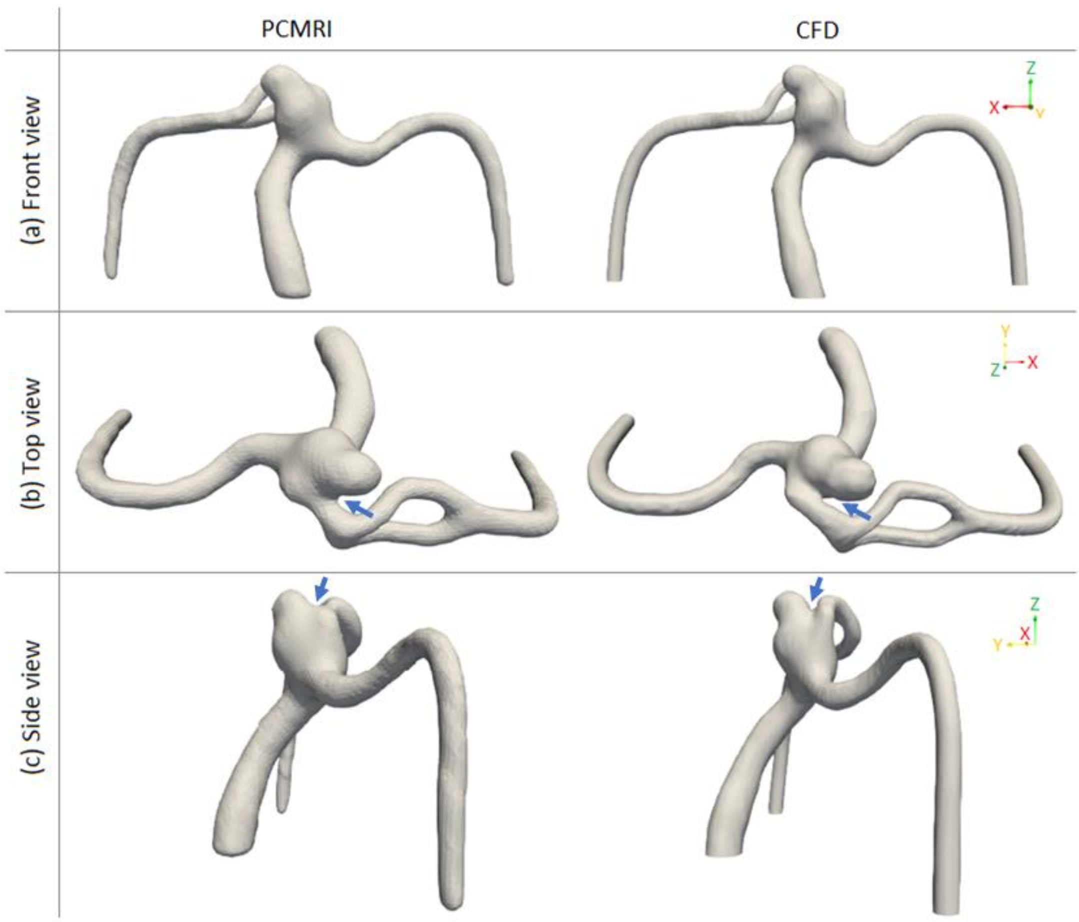

Figure 3-13 Comparison of the morphology of 3D models used in CFD and measured by PCMRI

treatments for intracranial disorders, which causes it to be recognised as a useful tool in the risk factor analysis after clinical operations [124]; meanwhile it could also assist to evaluate the treatment efficacy between different strategies, like clinicians' decisions on the number of FD stents, whether a compaction of the stent wires is needed, *etc.* [101]. This study has also examined the power of CFD technology to produce valid results that could assist to make decisions before and after clinical treatments.

3.4.1 Model Morphological Difference in PCMRI

According to the plane shape comparison in Figure 3-7, the discrepancies in plane A measured between PCMRI and other approaches are found to be at the location which is close to the aneurysm neck and the artery bifurcations – in another words, the area that has relatively complex morphological variations than normal blood vessels that may lead to unusual haemodynamic conditions.

Due to the technical restrictions, the measurement resolution adopted in PCMRI could not be as fine as that of PIV and CFD [73], therefore some morphological details might be unavoidably compromised. MRFD results are obtained based on the clinical imaging dataset scanned from 3D TOF MR angiography (MRA) and 3D PCMRI. As for other clinical imaging techniques like rotational angiography (RA) and computed tomography angiography (CTA), vascular geometries obtained by MRA are thought to be larger than those of real vascular geometries due to a partial volume effect caused by relatively poor spatial resolution [125,126]. Moreover, PCMRI is based on the detection of variation in spin motions of hydrogen atoms under a certain magnetic field, which relates to the phase shift that has a proportional relationship to the hydrogen particle velocity [127,128]. Nevertheless, unlike the water molecules in the body that provide hydrogen atoms (both moving particles in the blood flow and steady particles in the surrounding tissues), the silicone model that is the surrounding material of the BAF contains relatively few hydrogen atoms, which limits the performance of PCMRI measurement close to the model wall, which is also the edge of the fluid zone.

To further understand the morphology difference, I extracted the surface of the model generated from PCMRI measurement, which was then compared with the 3D model used for CFD (which was reconstructed from the microCT scans of the silicone model), as shown in Figure 3-13 Looking from the front view (see Figure 3-13(a)), the geometries for PCMRI and CFD show good similarity, in terms of the overall shape and size; the characteristics of aneurysm, bifurcations and artery bending are accurately captured. However, local discrepancies can be found around the aneurysm neck – more precisely, the junction area between the aneurysm neck and the outlet RPCA, as marked by the blue arrows in Figure 3-13 (b) and (c). Curvature of the bending from the aneurysm neck to the outlet RPCA is larger in the CFD model, resulting in a more obvious sunken region between the aneurysm and outlet artery.

According to size measurements with the CFD model, the smallest diameter of the BA, LPCA, RPCA, and aneurysm sac is approximately 3.2, 1.8, 1.4, and 3.5 mm, respectively; however, the narrowest distance between the aneurysm and RPCA at the sunken region is less than 0.3 mm, which is smaller than the pixel size in PCMRI measurement (with a resolution of 0.5×0.5×1 mm). This indicates that PCMRI detection for a complex geometry may unavoidably compromise some morphological details, especially for those with smaller size than the measurement resolution; however, the general characteristics of the geometry can be accurately replicated [111]. The morphology comparison between the physical silicone model and the MRA model for PCMRI is not presented here, as the physical model is considered to have the equivalent morphological details to the microCT-based CFD model (see Section 3.2.1.2).

This finding also explains the difference in the shape of plane A (see Figure 3-7), as it is located around the aneurysm neck, the difference in the sunken region degree affected the shape of the cut plane in aneurysm neck and the outlet artery.

3.4.2 Flow Pattern Discrepancies and Agreements in PCMRI

The planar velocity vector difference displayed in Figure 3-8 can also be explained by the morphological difference. As the separation point on the measurement plane is affected by the direction and position of the aneurysmal inflow and outflow, any morphological variation would easily lead to a changed haemodynamic behaviour.

Based on the model in Figure 3-13, the location of plane A in PCMRI should be closer to the junction area between the aneurysm sac and the RCPA than that in CFD and PIV.

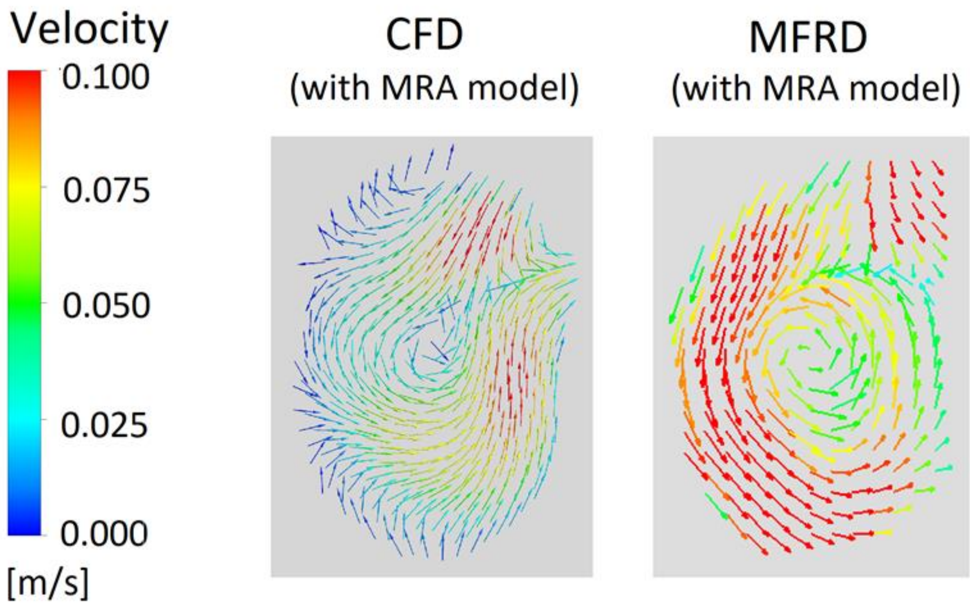

Figure 3-14 Comparison of velocity vector field on plane A between CFD simulation with the MRA model and MFRD processing of the PCMRI results

Thus, while the flow vortex in the aneurysm centre is the same as detected from PIV and CFD, the PCMRI-measured planar velocity vector close to the aneurysm wall represents a distinct flow pattern of aneurysmal outflow, before it joins the mainstream in the parent artery to then enter the outlet RPCA on the right side. Despite the planar flow pattern difference, the overall prediction of the 3D flow pattern is in good agreement with that of CFD, indicating the power of PCMRI to properly capture the global flow characteristics. In addition, those discrepancies of the local flow prediction could be avoided with the adoption of an improved measurement resolution [111].

To exclude the velocity vector discrepancies due to the model morphological differences raised by the MRA measurement, an extra CFD simulation was performed with the aneurysm model generated from MRA, and its velocity vector result was compared to the MRFD result, as shown in Figure 9. Comparing to Figure 4, improved similarities in flow pattern can be seen here, especially at the right side where is connected to the bifurcation to RPCA and close to the sunken region. This finding confirmed the influence on the velocity vector comparison by the model morphological differences reported in Figure 3-14.

3.4.3 Advantages and Drawbacks in Different Methods

Through the investigation of aneurysmal haemodynamics obtained from PIV, CFD, and PCMRI, the advantages and disadvantage for each of them were revealed. As an optical method to visualise the flow movement in the target model, PIV could precisely capture the velocity vector field in fine resolution with the use of a high-speed digital camera, if the experimental system was properly established. Modelling of the physical fluid environment, matched refractive index of the fluid with the material used for the *in vitro* model, and accurate calibration of pixel size in the post-processing are crucial factors affecting the validity of experimental results. In this study, the PIV result analysis could only provide 2D velocity vector fields due to the restriction from our 2D PIV experimental setup. With a 3D PIV system or the volumetric PIV system, a 3D planar velocity vector field or the flow pattern in the 3D fluid zone can be visualised; however, requirements for experimental setups would become far more complex, with the support of more high-performance devices and more sophisticated calibration and post-processing techniques.

Compared to PIV, CFD is a more flexible tool that allows the 3D fluid zone to be precisely predicted, although the simulation requires necessary assumptions which may unavoidably idealise the modelling of flow and the variations in the flow field. However, assumptions can be reasonably adjusted to avoid over simplifications [129]. While it is important to define the boundary conditions as close as possible to the physical environment to mimic the real flow field, some adjustment of boundary condition settings would be required in the best interest of calculation. For example, in this study, in order to achieve a converged calculation, the boundary condition set for inlet BA in CFD was adopted as traction free at zero pressure, instead of the actual flow rate measured from patients which was used for the physical flows in the other two methods (while CFD boundary conditions for outlets followed the measured flowrates). However, the resulting inflow and outflows were calculated and compared to the measured flowrated afterwards, to validate the choice of boundary conditions. In a word, such parameters should be carefully adjusted to ensure it would not create a distinct flow environment, thereby leading to different flow behaviours.

For PCMRI, while it measures the 3D flow field without flow assumptions and compromised boundary conditions, the resolution is not as fine as that of the other two approaches due to the current technical restrictions [73]. For geometries in larger scale that have less morphological details than patient-specific cerebral aneurysms, PCMRI would be more powerful to capture the flow patterns. For those models with similar scales and complexities as that used in this study, though the measured 3D streamlines could provide a reasonable global flow pattern, adopting a fine resolution with considerations of the smallest geometrical detail would result in a more precise local flow pattern.

Moreover, it is difficult to create an 100% same flow environment between the in vitro measurement and numerical simulation, as the fluid flow react sensitively to its surroundings, for example the in vitro models and working fluid may be slightly varied in different times of fabrication. However, in the present study the modelling of aneurysm model as well as the working fluid are technically controlled by both the mechanical properties and the fluid properties [130].

3.4.4 Limitations

Considering the facts that high flow rate leading to high Reynolds number of the flow might require a different assumption of turbulent flow (rather than laminar, depending on flowrate and geometry though) in the CFD simulation, or wide-range velocity variations might still challenge the PIV algorithm [131], we should be aware that different inflow conditions may create unexpected problems for each method. This means that a wider range of inflow conditions for this validation study could help to examine the performance of each approach from a more comprehensive view. Besides, it would also be meaningful to compare the flow pattern on different target planes, and thereby investigate the agreement between these methods affected by the local morphological complexities.

All experiments were performed under a steady-state flow condition, without consideration of the pulsatile phenomenon, as the intracranial blood vessels have negligible pulsation along the cardiac cycle. Other studies have demonstrated that despite small variations of the local flow due to the pulsatile flow behaviour, steady flow simulation provides a good approximation of spatial average velocity magnitude in IA [132], and the instantaneous shear stress and flow rate in a pulsatile flow regime can be estimated reasonably well from a steady flow simulation [133]. It is also reported that that steady-state models provide reasonable estimates for the time-averaged haemodynamics of true pulsatile flow [134].

Due to some systematic limitations, the aneurysmal flow pattern was only compared between different methods on a single target plane, at a given inflow condition in this study. However, the adopted inflow rate could be regarded as a representative level within the range of the average flow rate in human cerebral arteries; further, the selected measurement plane was located at the critical section around the aneurysm neck, with morphological details in high complexity. With the above-mentioned facts, I assume that the finding from this study could be representative and useful as a preliminary research outcome, even with limited research scenarios. Studies with a more comprehensive scheme should be carried out in future works.

Moreover, as resolution and precision for each method varies, the accuracy of each obtained result can be affected. However, we performed a mesh dependency test for the CFD simulation to assure the simulation accuracy. Also, a fine resolution at the best capability of the high-speed camera was adopted for PIV, while the measurement using MRI set a resolution as good as possible.

3.5 Conclusion

In this study, I studied the flow pattern in a patient-specific cerebral aneurysm using both experimental and numerical approaches that are commonly adopted in fluid dynamics studies – PIV, CFD, and PCMRI – and compared the geometric shape, planar velocity vector field and 3D streamlines obtained from these methods. The flow patterns between PIV and CFD show good agreement, in terms of the 2D velocity vectors and the in-plane velocity magnitude. Meanwhile, the 3D flow pattern obtained from PCMRI shows good similarity to that of CFD. Through this comparison, outcomes of CFD simulation have been quantitatively validated against experimental outcomes, and the results give confidence to future haemodynamic studies using CFD technology, which would better assist the surgical planning and treatment strategy evaluation before and after clinical operation for intravascular disorders.

This work provides a vital foundation for future validation studies, as the reported agreements and inconsistencies between different approaches have preliminarily revealed their advantages and drawbacks. Based on this, improvements can be made to further validate the analysis by these methods in a more comprehensive scenario. Moreover, deeper understanding of these research methods is beneficial for future aneurysmal haemodynamic investigations, as it might contribute to more reasonable adoptions of research approaches and protocols to serve the purpose.

Chapter 4

Validation of CFD Model Results against PIV Observations of Haemodynamics in Intracranial Aneurysms Treated with a Flow-Diverting Stent

4.1 Introduction

4.1.1 Background

As aneurysmal haemodynamics is considered to be an important factor affecting the initiation, growth, and rupture of intracranial aneurysms (IAs), different methods have been established to study the aneurysmal fluid flows, with either *in vitro* phantoms or 3D virtual models.

Besides the exacerbation of aneurysm severity, the healing of an aneurysm is also closely related to the haemodynamic variations in the aneurysm after clinical operations. One of the commonly adopted endovascular treatments for IAs is to place a flow-diverting (FD) stent across the aneurysm neck to discourage the blood flow from entering the aneurysm neck, thereby leading to an aneurysm occlusion. Therefore, post-treatment aneurysmal haemodynamic modification is a critical indicator of treatment effectiveness.

Several methods are commonly adopted to obtain such aneurysmal haemodynamic modifications, before and after FD stent treatment, to assist with the estimation of the treatment efficacy. As introduced in the previous chapter, particle image velocimetry (PIV) involves the measurement of real physical motions but can be cumbersome and expensive to establish. Meanwhile, computational fluid dynamics (CFD) is more flexible than PIV, offers higher spatial resolution and the ability to derive all flow parameters, but it necessarily requires several assumptions or parameters to be specified by the operator.

While a physical stent can be used in PIV experiments, the investigation of flow-diversion treatment efficacy using CFD simulations requires modelling of the FD stent. There are different options to model the FD stent for CFD – using the fully-resolved stent model [100,101], or alternative methods like modelling the stent as a porous medium (PM) layer [58,79,83]. Nonetheless, the specification of the stent model in the numerical simulation is critical to resolve accurate fluid behaviour.

4.1.2 Current Issue

As indicated in the previous chapter and a number of published studies on untreated aneurysms, the aneurysmal flows obtained from different approaches like PIV and CFD shows reasonable agreement [76–78]. However, the more complicated flow behaviour in a patient-specific aneurysm with a deployed FD stent could be a more challenging subject for flow validation using the two different methods, and little study has checked their agreements and differences. Moreover, in terms of flow-diversion efficacy, results obtained from numerical simulation when the stent is modelled as a PM layer have never been validated before against physical measurements.

4.1.3 Purpose

To make the power of CFD available to the challenge of modelling blood flow for FD stents deployed into patient-specific aneurysm models, it requires a validation against physical measurements. In this research, a more sophisticated validation of the CFD model against PIV data for a patient-specific aneurysm, without and with a *Silk* stent, was carried out, aiming to comprehensively examine the flow agreement between the two approaches at a variety of flowrates and at several locations in the aneurysm, and thereby validate the flow behaviours obtained with the PM modelling of the FD stent in simulations.

4.2 Materials and Methods

4.2.1 Aneurysm Geometry

This study referred to a patient case comprising a 66-year-old female manifesting a sidewall IA of approximately 25 mm maximal diameter and 20 mm in effective diameter located on the internal carotid artery. This patient was subsequently treated successfully with a *Silk* FD stent (post-treatment follow-ups observed complete occlusion in the aneurysm), but the pre-treatment geometry is used herein.

Figure 4-1 Reconstructed aneurysm (left) and the manufactured silicone phantom (right): the dark grey area in the in silico model stands for the PM stent and the position of aneurysm neck, and the metal mesh in the silicone model is the *Silk* stent; the silicone model is filled with BAF and air-bubble, which lead to torsion in the view of the *Silk* stent

Institutional ethics approvals (Ref 5201100750 and 10274L) permitted use of this patient-specific geometry.

A 3D virtual aneurysm model was reconstructed based on a set of 2D DICOM data obtained by CTA scan using Mimics (Materialise, Leuven, Belgium). A cavity in the shape of the reconstructed aneurysm and associated parent artery, bifurcating into two outlets, was cast into a block of clear silicone [cf. 98,99] (see Figure 4-1).

4.2.2 Physical modelling

4.2.2.1 Flow-diverting stent implantation

A *Silk* (Balt International, Montmorency, France) FD stent which has a diameter of 4 mm and length of 30 mm was studied in this work. The size of the stent was selected to suit the patient-specific aneurysm geometry.

4.2.2.2 Flow Circuit

The silicone aneurysm phantom was connected via a series of tubes to a *BVP-Z* gear pump (Ismatec, Germany) with which the flowrate of blood-analogue fluid (BAF) was adjusted. Nominal flowrates of 150, 250, and 400 mL/min were set according to the reading from a calibrated ultrasonic flow transducer placed on the inflow tube. Pressure was also monitored at both inlet and outlet.

The BAF was prepared from a mixture of approximately 50.19 % water, 32.85 % glycerol, 16.86 % sodium iodide and 0.10 % sodium thiosulfate (by mass) [cf. 98,99]. At a room temperature of approximately 22 ± 1 °C, the mixture closely matched the refractive index of the silicone block (1.410, using an Abbe refractometer (Atago, Japan)), and also had a kinematic viscosity appropriate for blood (3.05 mm^2/s target value, which was confirmed to be attained to accuracy of better than ±15 % using a Cannon–Fenske viscometer (Cannon, U.S.A.)) (See Table 4-1).

Table 4-1 Properties and compositions of the blood-analogue fluid

Parameter	**Target**	**Actual**
Refractive index [–]	1.41	1.408 to 1.412
Kinematic viscosity [mm^2/s]	3.05 to 3.06	~2.88 (2.82 to 2.92)
Density [kg/m^3]	—	1248 to 1250
Viscosity [mPa.s]	—	~3.60
Temperature [°C]	22.0	22±1
H_2O [$\%_m$]	50.19	*
$C_3H_8O_3$ [$\%_m$]	32.85	*
NaI [$\%_m$]	16.86	*
$Na_2S_2O_3$ [$\%_m$]	0.10	*

*True proportions of each pure component added are not precisely known, as the NaI used had absorbed some (unknown) amount of water, and the composition of the original mixture was therefore adjusted to achieve the desired refractive index. However, based on the properties being close to the target values, it is fair to assume that the actual percentages would indeed be close (±5%, say) to the target values. An additional small amount of sodium thiosulfate was also added several months later to address the subsequent slow decolouration.

4.2.2.3 PIV measurement system

An ILA (Intelligent Laser Applications GmbH, Germany) 2D PIV system was used (see Figure 4-2), consisting of a SensiCam (PCO, Germany) 12-bit digital CCD camera (1280×1024 pixels), which was synchronised with a New Wave (New Wave Research, USA) 120 mJ double-cavity Nd:YAG Laser. The output laser beam at wavelength of 532 nm was guided through an articulated arm system to the measurement location, where the beam was expanded by a cylindrical lens to form a 1.0 to 1.5 mm thick planar vertical light sheet over the measurement plane. The typical field of view of the CCD

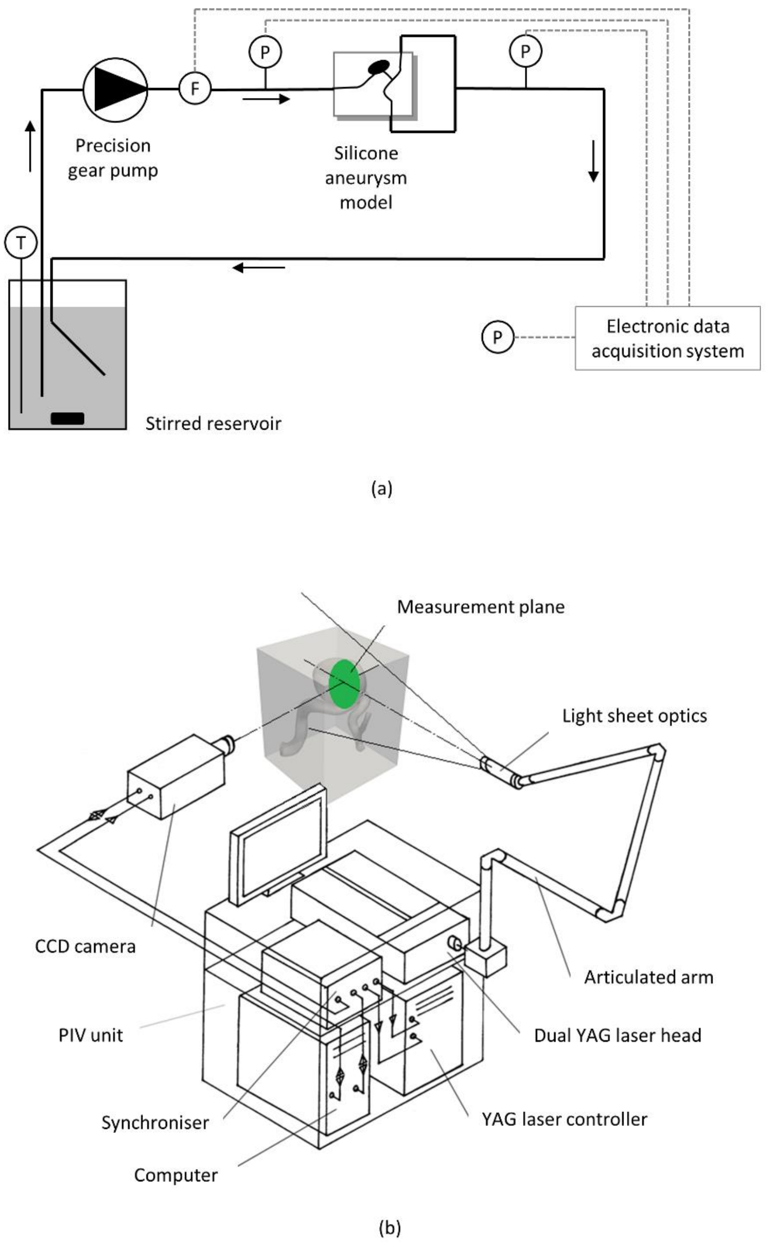

Figure 4-2 PIV experimental setup: (a) schematic depicting the circuit used in the physical modelling; T indicates temperature measurement (alcohol thermometer), F indicates flow measurement (ultrasonic non-contact sensor), and P indicates pressure measurement (non-contact sensors adjusted for ambient pressure); (b) schematic depicting the PIV measurement system.

camera was 35 × 28 mm^2 using 1280 × 1024 pixels of CCD array. The smallest resolvable length is 27.3 μm, which is the real length of each pixel. The interrogation windows were 64 × 64 pixels (1.75 × 1.75 mm^2), with 50% overlap between consecutive interrogation cells, providing a velocity vector spacing of 32 pixels (0.875 mm).

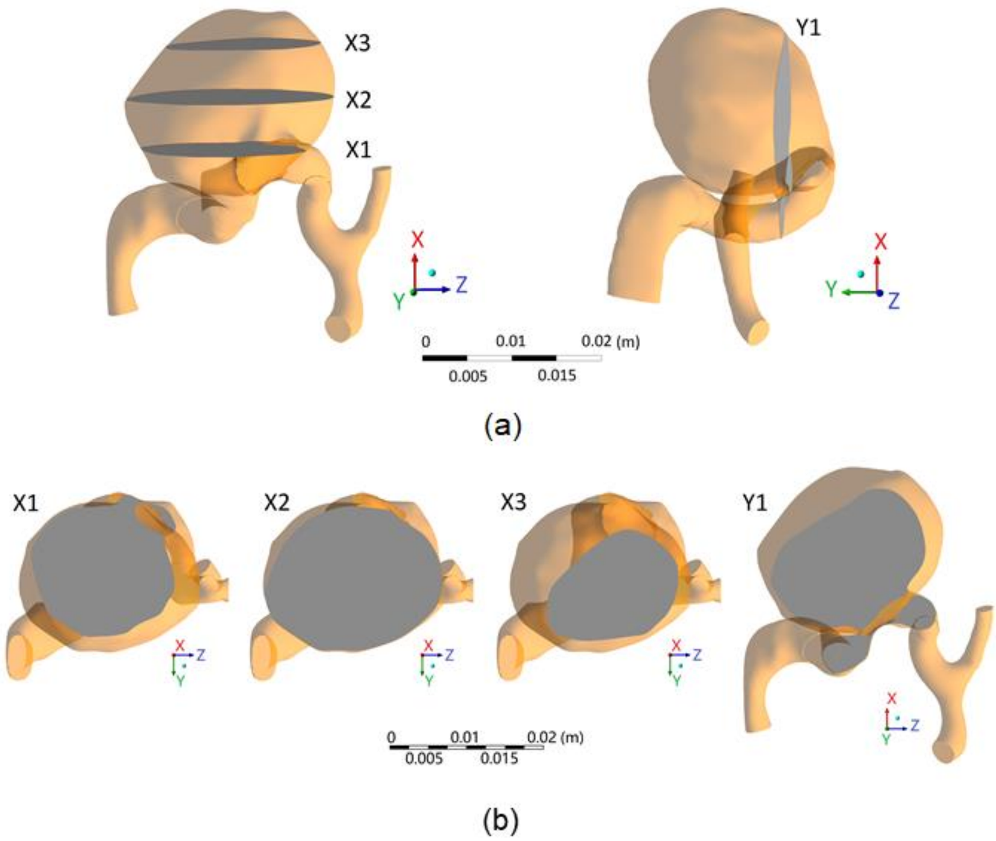

Figure 4-3 Sketch of measurement planes: (a) positions of measurement planes respectively in horizontal and vertical directions; (b) shapes of measurement planes.

To avoid the reflection on the metal stent and improve the clearness of the flow movements, rhodamine B fluorescent particles were used as the seeding particles in the BAF at low concentration. The fluorescent particles have a mean diameter of 18 μm and a relative density of 1.09. When the measurement plane is illuminated by the laser sheet, the light scattered or reflected from the silicone block and the metal stent has the same wavelength as the laser (532 nm). However, the light emitted from the Rhodamine B fluorescent particles has a longer wavelength (>570 nm). With the aid of an optical long-pass filter at 550 nm to eliminate the scattered and reflected light from the silicone block and metal stent at 532 nm, only the fluorescent light from Rhodamine B articles is transmitted to the CCD camera. The optical relaxation time of the seeding particles is about 20 μs, which is negligible compared to the separation time of 400 μs between the pairs of images used for computation of particle displacements. The uncertainty of pixel displacement in the measurement is about 0.2 pixels within the interrogation window of 64 × 64 pixels. In each PIV measurement, 400 pairs of successive images were taken at the laser repetition rate of 4 Hz. Hence, a mean velocity flow pattern was obtained by statistically averaging 400 successive instantaneous velocity vector maps over approximately two minutes.

PIV measurements were made on two series of planes illuminated by the laser. For one series the planes were approximately parallel to the neck of the aneurysm, and planes in the other series were perpendicular to this. In this study, several representative planes were selected to perform the velocity vector field analysis for the comparison with CFD results. These planes are depicted in Figure 4-3(a). Plane X2 is located at the centre of the aneurysm, while plane X1 and X3 are parallel planes on the left and right of plane X2, with approximately 6 mm displacement either side. Plane Y1 is located at the centre of the jet flow in the perpendicular orientation.

4.2.3 Computational Modelling

4.2.3.1 Flow-diverting stent modelling

In order to save simulation time, a PM stent model was employed instead of resolving the geometry of the individual FD wires. Like the physical stent, the FD stent model used in CFD was designed as a tube across the aneurysm orifice to fit the shape of the patient artery. The FD stent was then defined as a homogeneous PM layer with a thickness of 0.1 mm, which is consistent with our other report and has been demonstrated to be sufficiently thin to provide accurate modelling of the flow [137,138]. Thinner models will more or less lose the advantages of using a PM model, while the accuracy will not have practical improvement. From clinical observation, we found the flow appeared to be closed at the aneurysm neck. Therefore, we designed the FD stent model to completely fit the patient artery in our CFD model. (More details about the methodology of PM stent modelling can be found in Section 2.2.2.)

Based on computed correlations previously reported for a 0.08 mm thickness [79], this study adopted as initial values a permeability of 1.40×10^{-9} m^2 and an inertial resistance factor of 6962 m^{-1}, as the corresponding thickness-compensated values for the flow resistance parameters in our PM model, to describe flow resistance through the wall of the FD stents.

4.2.3.2 CFD simulation

CFD modelling was performed using the CFX software suite (ANSYS, U.S.A.). Blood density was specified as 1050 kg/m3, while viscosity was 0.0035 Pa·s. Steady-state simulations were conducted, with a laminar flow specification. Due to the rather thin geometry, computational meshes of more than 1 million cells were employed (validated as practically grid-independent by using up to 16 million cells).

4.3 Results

4.3.1 CFD versus PIV: no Stent

4.3.1.1 2D velocity vector contour comparison

PIV provides estimates of in-plane velocity on several cross-sections. In-plane velocity vectors are also available from the CFD modelling for corresponding planes.

A side-by-side comparison of flow patterns from CFD and PIV without a FD stent is presented in Figure 4-4(a) for a flowrate of 250 mL/min on plane X1, X2, and X3. Clearly a good agreement can be found in the position of the vortex, the direction of the circulating flow, and the planar velocity distribution. While the general flow pattern matches well, the vortex positions are slightly more towards the wall in the CFD result on all planes, especially for plane X3.

To be more precise, the positions of vortices measured in different situations (planes and flowrates) were quantitatively compared. At the middle flowrate (250 mL/min), the vortex centre predicted by CFD on plane X1 is at identical horizontal position and approximately 1.7 mm higher in vertical direction than that of PIV. While on plane X2, the CFD vortex centre is at similar vertical position and approximately 4.5 mm to the right of the PIV location in the horizontal direction. Further, the vortex centre on plane X3 in CFD is at similar vertical height and approximately 1.5 mm to the left of the PIV location in the horizontal direction (refer to Table AII-1 in Appendix II). These results are in agreement with the visualisation that vortices in CFD results are slightly near to the wall.

For brevity, while the validation also hold for planes X1 and X3, I present here for the two other flowrates vector plots for only plane X2, which is the centre plane for the two other flowrates (Figure 4-4(b) and Figure 4-4(c)). Similarities in the flow pattern and velocity distribution can also be clearly seen.

Besides this, the velocity magnitude represented by colour indicates good agreement between results from CFD and PIV. It can be observed that the jet flow velocity predicted by CFD is slightly higher than that of PIV on all measurement planes at different flowrates.

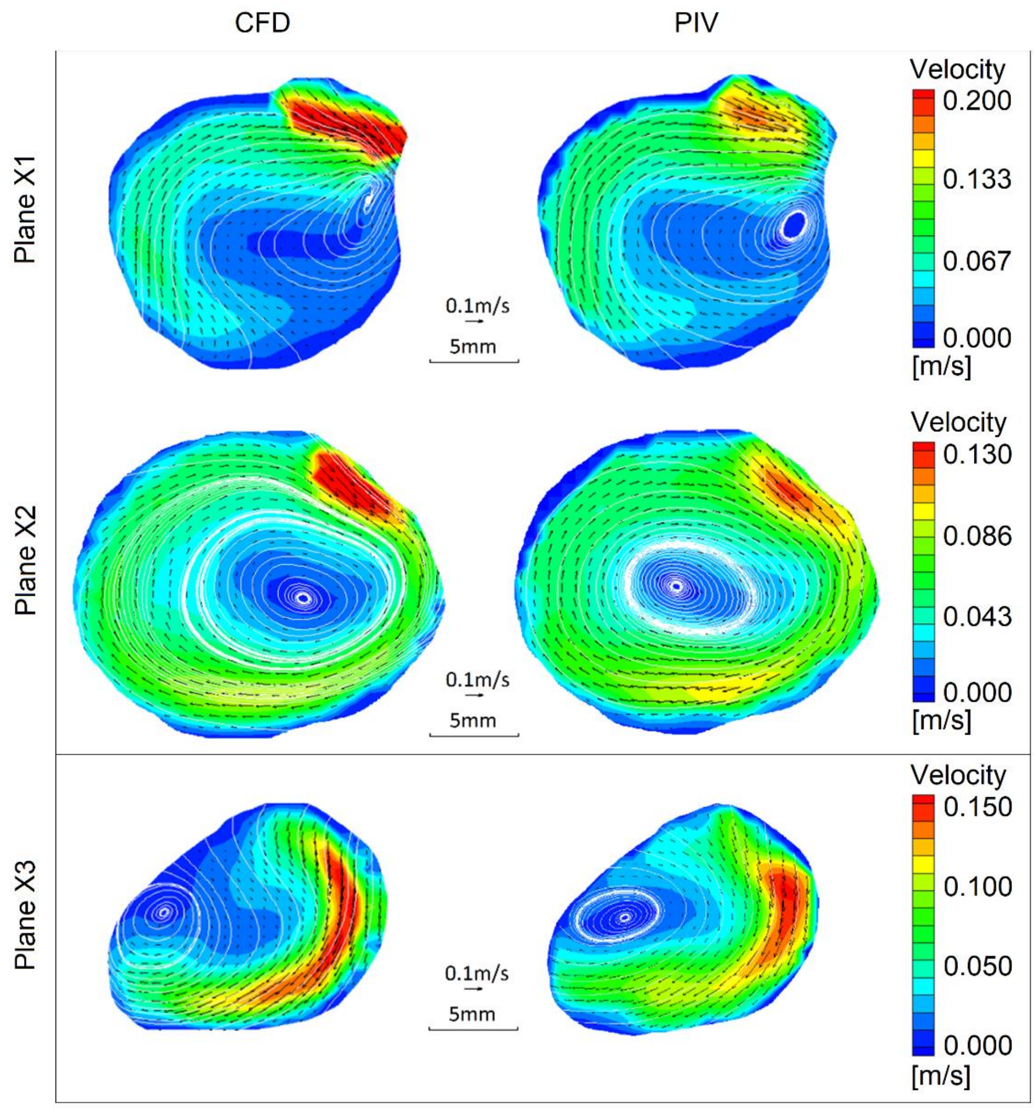

(a)

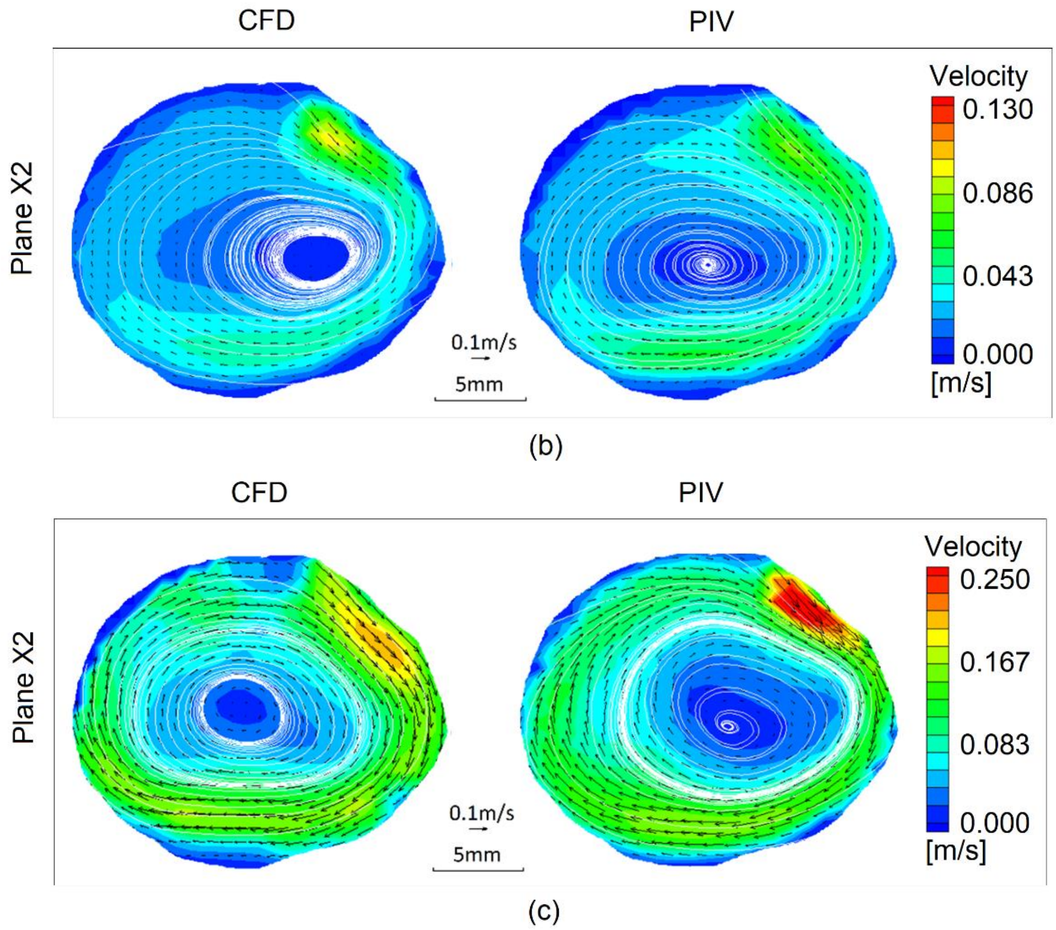

Figure 4-4 Comparison of velocity contours on measurement planes in horizontal direction for the no stent case at different flowrates (black arrows are individual velocity vectors and while lines are velocity streamlines) : (a) 250 mL/min (b) 150 mL/min (c) 400 mL/min.

4.3.1.2 Velocity magnitude comparison

Although the inspection of velocity vectors and contours was performed on the entire cross-section on numerous planes at different flowrates, to demonstrate the quantitative agreement, I extracted estimates of the vertical velocity components along a line through the vortex centre on each plane. A few important planes (X1, X2, and X3) that represent the haemodynamic features, at a middle flowrate of 250 mL/min were reported here. The data are plotted and compared in Figure 4-5, in which the positions of the lines are given in small inset sketches. PIV results are displayed point-by-point along the selected lines, while CFD results can be displayed as continuous lines due to its fine spatial resolution. Overall both the direction and the magnitude of this velocity component are matched along the selected lines in all three planes, while differences can be noticeable at the points in the jet or adjacent to the wall.

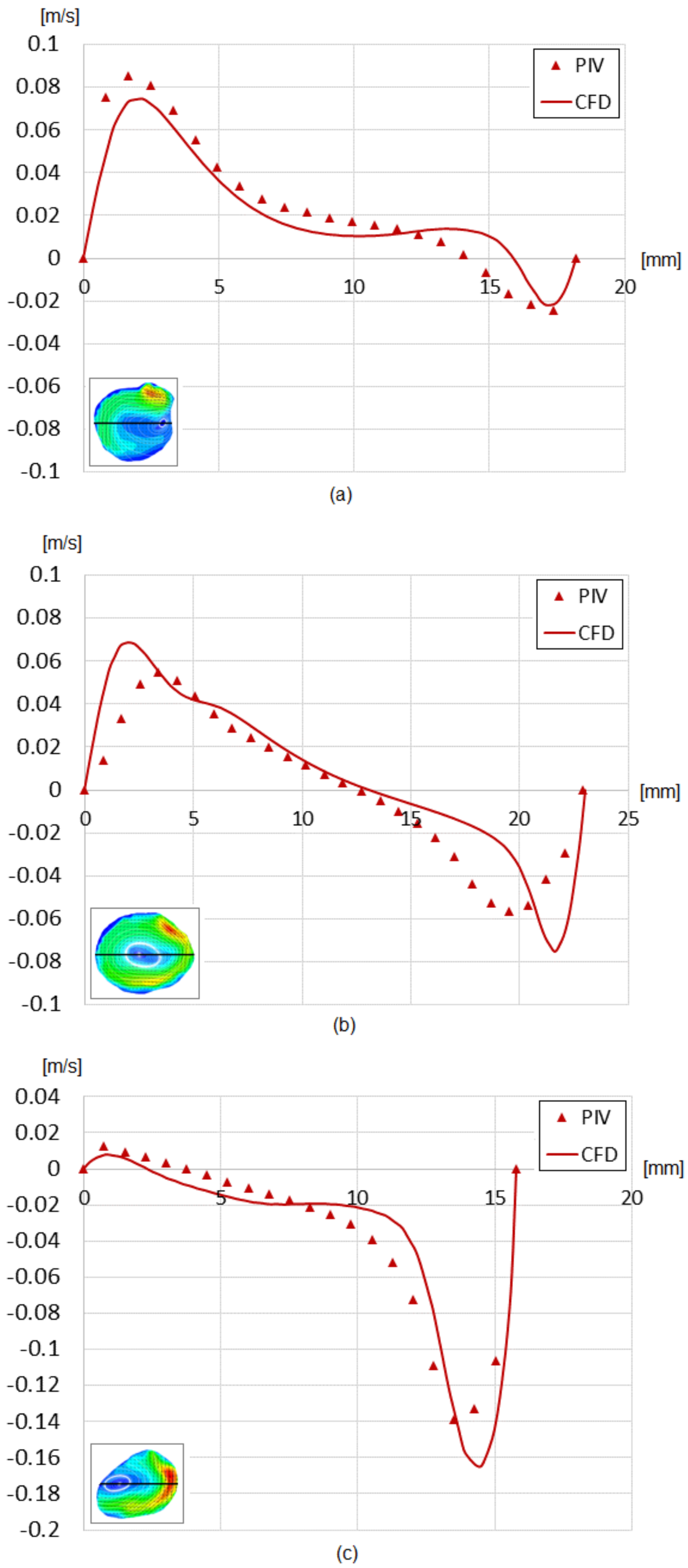

Figure 4-5 Comparison of in-plane vertical velocity through a line on each measurement plane at flowrate 250 mL/min for the no stent case: (a) Plane X1 (b) Plane X2 (c) Plane X3 (ordinate represents the vertical velocity and abscissa represents the horizontal positions from left to right edge).

1194

4.3.2 CFD versus PIV: with *Silk* stent

4.3.2.1 2D Velocity vector contour comparison

Figure 4-6(a) presents a comparison between aneurysmal flow patterns obtained from CFD and PIV after being treated with a *Silk* stent on four measurement planes (X1, X2, X3, and Y2) at the medium flowrate of 250 mL/min. The agreement is tolerable, although not so close as in the untreated scenario. CFD predictions using the reference *Silk*-based flow resistance parameters show similar flow patterns to PIV observations with perceptible difference.

Plane X1 goes across the convex curve of the stent as it is located just above the aneurysm neck, so the high-speed mainstream flow in the parent artery is displayed in the CFD result at the top-right corner in Figure 4-6(a). The analysis of flow measured by PIV in this area was however eliminated to avoid noise, as the metal stent had induced strong reflection. In the remaining areas on plane X1, the distribution of velocity vectors and streamlines between CFD and PIV are in an acceptable concordance, along with the velocity contours. As for plane X2, which is located at the middle of the aneurysm with less influence of the FD stent, the flow patterns from CFD and PIV show good agreement (see Figure 4-6 (a)). The positions of the vortex centre in both results are at similar vertical locations, with the CFD vortex slightly towards the right side by approximately 2.5 mm in the horizontal direction (refer to Table AII-1 in Appendix II). However, on the off-centre plane X3, the vortex position obtained from CFD is apparently close to the wall compared to that of PIV, resulting in varied velocity streamlines around the vortex (see Figure 4-6 (a)). Comparison was also carried out on a plane in the vertical direction that captures the jet flow, plane Y1, on which similar flow patterns and velocity magnitudes for the CFD and PIV results can be observed (see Figure 4-6 (a)).

For brevity, for the two other flowrates velocity contours are only presented for plane X2 here (Fig. 4-6(b&c)), in which acceptable agreements between flows are observed, while the validation also holds for planes X1 and X3.

As in the untreated case, the jet flow velocity calculated by CFD is higher than that measured by PIV at each flowrate on all cross-sections.

4.3.2.2 Velocity magnitude comparison

In-plane velocities extracted along the same lines specified previously are shown for planes X1, X2, and X3 at a flowrate of 250 mL/min in Figure 4-7. From the plotted results for CFD and PIV, vertical velocities along the line on each cross-section plane are generally in acceptable agreement. Further, comparing to the untreated velocity magnitude, apparent flow reduction can be generally observed from the velocity estimates on all cross sections in the treated aneurysm model.

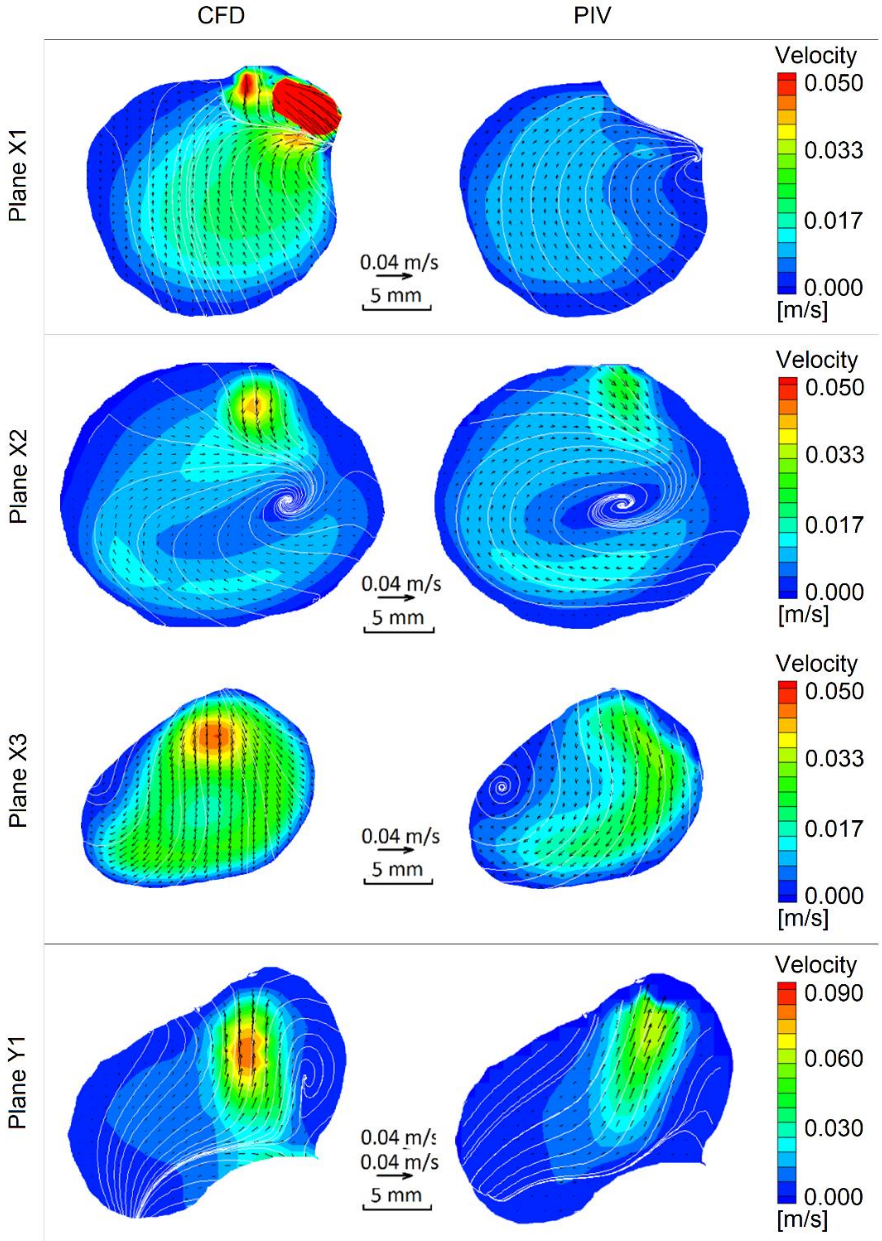

(a)

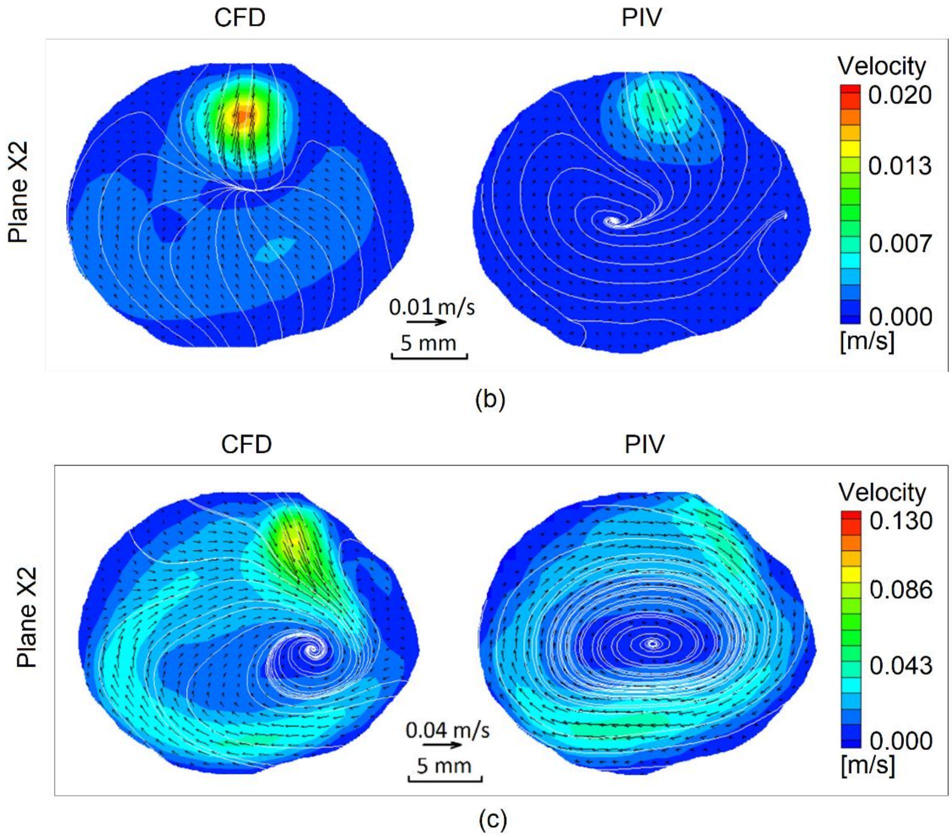

Figure 4-6 Comparison of velocity contours on measurement planes for the *Silk* stent case at different flowrates (black arrows are individual velocity vectors and while lines are velocity streamlines) : (a) 250 mL/min (b) 150 mL/min (c) 400 mL/min.

1232

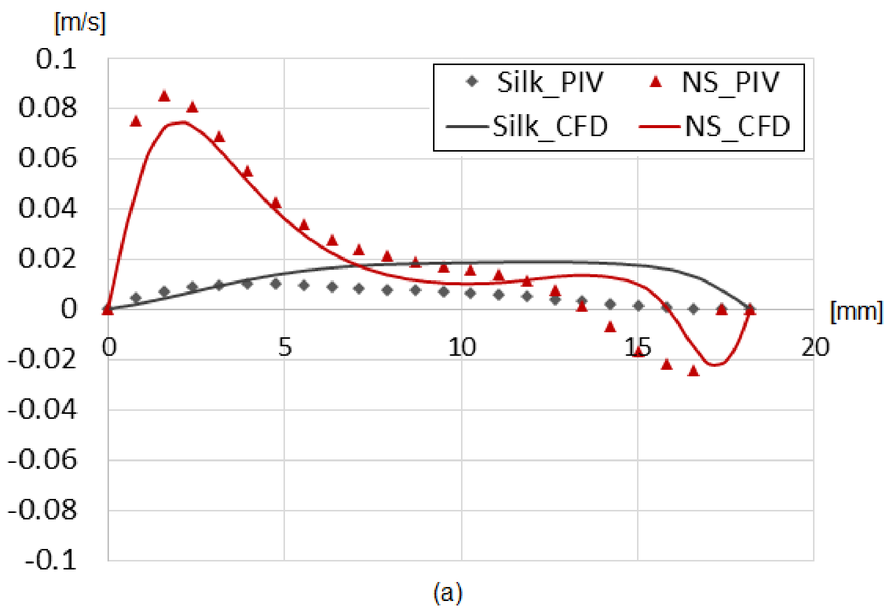

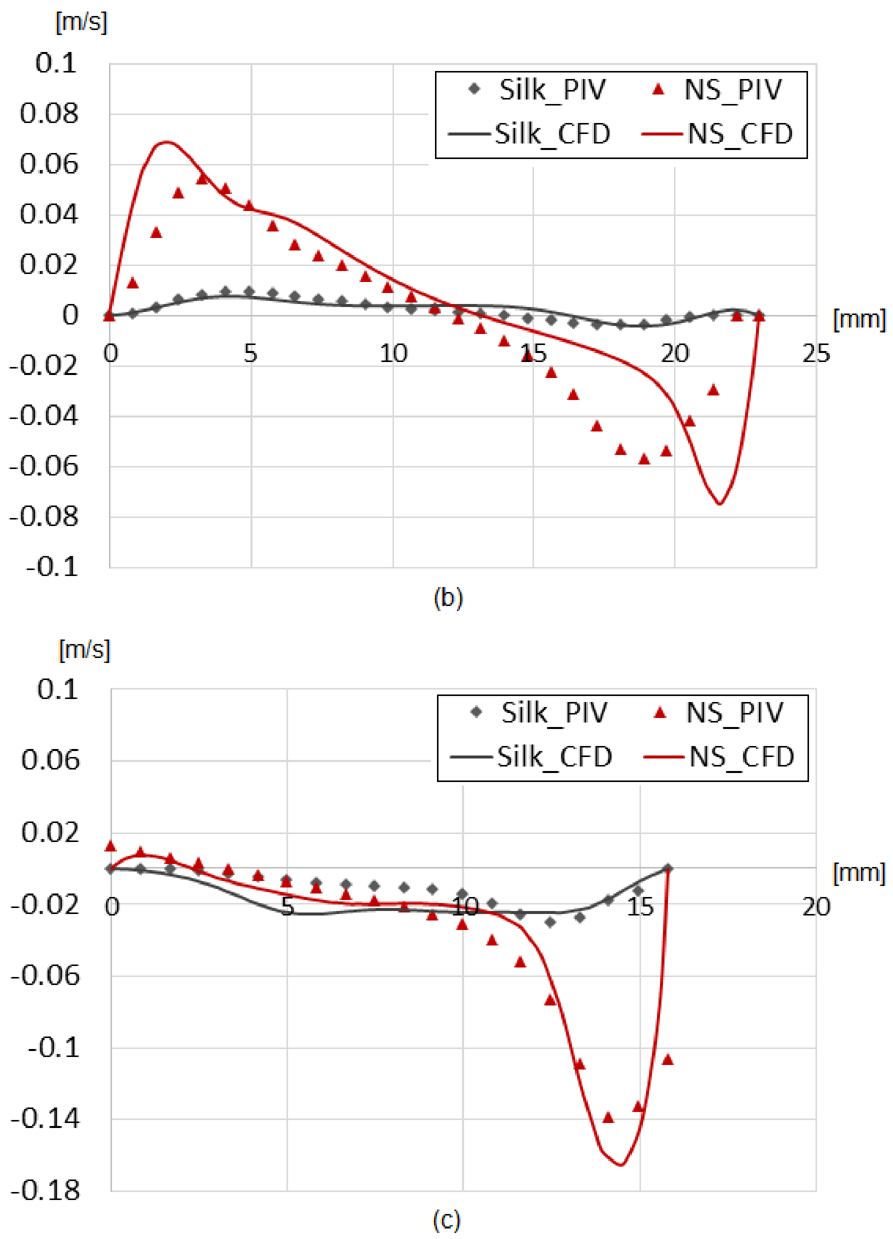

Figure 4-7 Velocity reduction after Silk stent treatment and the comparison of in-plane vertical velocity through a line on each measurement plane at flowrate 250 mL/min for the *Silk* stent case: (a) Plane X1 (b) Plane X2 (c) Plane X3 (ordinate represents the vertical velocity and abscissa represents the horizontal positions from left to right edge).

4.4 Discussion

This study has investigated the aneurysmal flow pattern, before and after FD stent treatment, using PIV and CFD, when the *Silk* stent used in PIV was modelled as a PM model in CFD. Velocity vectors and contours on different cross-section planes in both the horizontal and vertical direction to the aneurysm neck were checked, together with the in-plane velocity estimates comparison on a line across the detected vortex for each plane. By doing this, the comparison has achieved a pleasing concordance between the CFD and PIV results, which validates the CFD models for both the no-stent and with-stent cases.

The effect of inserting a FD stent, under all the flow conditions and at different planes within the aneurysm, can be clearly observed in the PIV measurements. Nevertheless, there is a practical benefit to being able to predict flow behaviours using computational models, without resorting to physical experimentation.

This work demonstrates that modelling of a FD stent as a PM model in CFD can achieve an accurate prediction of the aneurysmal flow variations, provided that the PM properties are set to create a flow resistance that matches that of the represented physical stent. Although previous researchers have estimated flow resistance by comparing PM stent models against fully-resolved stent models in CFD, this study is the first to validate the PM stent model simulation results against observations from physical PIV measurements.

4.4.1 Advantages of PM Model Due to the Uncertainty of FD Stent Deployment

Although the flow resistance created by a FD stent with a particular mechanical construction is designed to be constant, many other factors affect the actual flow-diversion efficacy, like the individual aneurysm geometry and the manner of the stent deployment.

For deployment of a physical FD stent in a patient-specific aneurysm, the wire structures may differ substantially depending on the deployment strategies, applied force, neck morphology, *etc.* in individual operations. Moreover, stent configurations resulting from different virtual stent deployment methodologies can also vary. A previous study revealed 10 percentage points' decrease in aneurysm inflow with every 25 percentage points' increment in compaction of stent wires [101]. These facts would increase the difficulties in accurately modelling a fully-resolved wire stent for CFD simulation.

Modelling the FD stent as a PM model avoids the unpredicted complexities in local wire distribution, while the flow resistance created by the PM layer can be calibrated to match with the represented stent, by defining the PM properties. This feature enhances the stability of the flow-diversion effect. From the acceptable agreements between PIV and CFD results, the PM stent model presented in this study is found to be a practical and flexible tool to be used in the prediction of the flow behaviour.

4.4.2 Sensitivity to Measurement Plane Location

The discrepancy in the vortex positions of the PIV and CFD results on plane X3 for the *Silk* case (see Figure 4-6) raised my concern about the precise location of the measurement plane position in those two sets of data. Considering the possible positioning errors, given that the laser sheet is 1.0 to 1.5 mm thick, slight misalignment could happen during the experiment. Therefore, CFD results on a plane with a 1 mm displacement to plane X3, namely X3', were checked, which shows apparently improved agreement with the PIV results (see Figure 4-8). This finding indicates that the planar flow contours could be sensitive to the location, even within small 1 mm displacements. The alignment of measurement planes should be carefully noted.

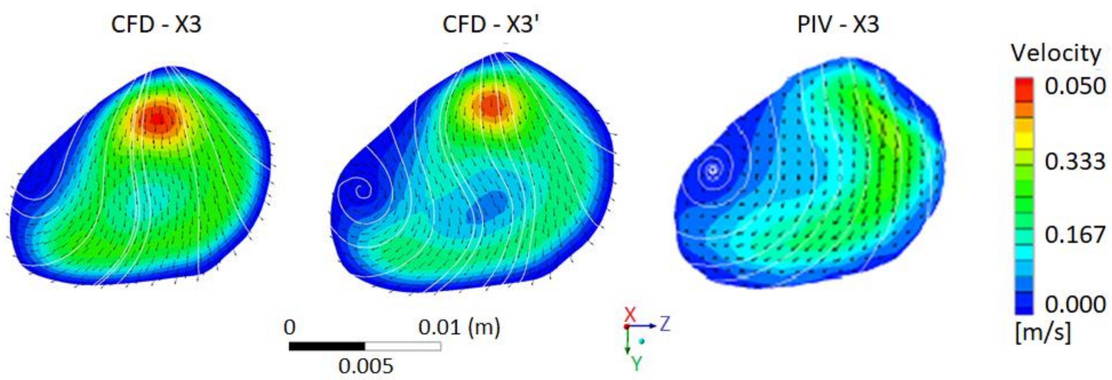

Figure 4-8 Comparison of velocity contours on measurement plane X3 and X3' (1-mm displacement to X3) for the *Silk* stent case at flowrates 250 mL/min

4.4.3 Limitations

Whilst the comparison yield good agreement in the flow patterns throughout the majority of the aneurysm domain, it was unable to obtain exactly matched flow details at every location including the jets and vortices. However, it is unrealistic to expect 100 % agreement between physical experiments and computational simulations. Unavoidable differences can arise though, for example, tiny discrepancies in the location of the laser light sheet (that may result from a misalignment or the finite thickness of the laser sheet), and small discrepancies in the construction of the physical silicone model geometry compared to the computational model geometry. PIV measurements are also less reliable in the immediate neighbourhood of walls, stents or jets [139]. Furthermore, PIV relies on coarser interpolation, and can be influenced by flow patterns existing slightly in front of or behind the nominal location of the plane.

There are also some assumptions inherent in the simulations. CFD was implemented using a steady-state assumption, which should match the constant flow conditions of the experiment well. Other studies have demonstrated that steady-state models provide reasonable estimates for the time-averaged haemodynamics of true pulsatile flow [134]. An indication of the effect of varying flowrate can also be gained by examining the three flowrates considered herein. Furthermore, CFD was implemented using a laminar flow model in this study. Although this has been shown to be reasonable for steady flows [58], for pulsatile flows other models may be worth considering [140].

The above comparisons also show that the agreement of flows in the untreated case is better than that of the stented case, which can be affected by the simplifications (homogeneous and isotropic features) and parameter specification (k and C_2) set for the PM model in this simulation. It could be possible to improve the ability of the PM model to precisely replicate the local resistance of the physical stent by the use of spatially-varying parameters [102], or with different resistances for tangential flow within the PM model [cf.63,64]. However, there is insufficient basis for adding more parameters into the model at present, as this study aims to validate the simulation result against the physical observations by using *Silk*-based PM stent modelling. The comparison has demonstrated the credibility of the use of *Silk*-based PM stent modelling, provided that the PM model properties are specifically defined based on the represented physical stent. More sophisticated settings of PM properties can be studied in future work.

4.5 Conclusion

Flow patterns in a patient-specific aneurysm obtained between PIV and CFD have been comprehensively compared in this study, qualitatively and quantitatively, with and without the *Silk* FD stent, at three arterial flowrates, and on numerous cross-sectional planes in different orientations.

In the absence of a FD stent, the CFD model is capable of accurately simulating flow within an aneurysm. With the modelling of a FD stent in the simulation of flow in a treated aneurysm, agreement can be maintained in the bulk flow patterns, with acceptable discrepancies at individual locations.

This agreement has revealed the power of CFD in predicting aneurysmal flows and resolving the flow variations with the application of a PM model stent. For the first time, the PM modelling of a stent has been validated against physical observations, through which the credibility of this methodology is confirmed. This study has built the foundation for the use and development of PM modelling in CFD as a practical and flexible tool for future investigations of aneurysmal flow variations after FD stent treatment.

Chapter 5

Sensitivity of Aneurysmal Haemodynamics to Porous Medium Stent Modelling Settings

5.1 Introduction

5.1.1 Background

In CFD simulations, modelling FD stents as fully-resolved wire meshes requires a large number of computational mesh elements, which increases the computational difficulties. To improve the simulation efficiency, modelling FD stents as a porous medium (PM) was developed [58,79,83].

5.1.2 Current Issue

In earlier studies, the diversity of PM stent models led to considerable differences in the flow resistance forces. Permeability is one of the main properties that characterise a PM, and describes the capacity for fluid transmission. Adjustment of the permeability, therefore, may result in a variety of flow resistance forces. As permeability is related to the stent porosity, the sensitivity of the flow to permeability also helps to predict the magnitude of effect arising when the porosity is modified due to a change in deployment of the device.

Meanwhile, morphological differences in PM stent models, for example the thickness, may also greatly affect the aneurysmal inflow [80]. Even though the true value of existing stents is about 30 to 50 μm, it may be computationally expedient to use a different thickness to model the PM stent. Besides, as the diameter of the parent arteries are usually in millimetres, thickness of the PM layer should be designed within a reasonable range, to ensure that the narrowed artery around the aneurysm neck (due to the existence of the PM layer) would not cause unexpected influence on the mainstream flow pattern and aneurysmal inflows. However, few studies have addressed these issues, or studied the effects of those parametric settings on aneurysmal haemodynamics.

5.1.3 Purpose

The objective of this study is to investigate the haemodynamic differences attributable to model parameter adjustments in CFD simulations with a PM stent. More specifically, this study focuses on the sensitivities to PM model thickness and permeability, by exploring their influences on post-stenting haemodynamics for multiple values of flow rate. Knowledge of sensitivity is useful given variability that may be caused from differences in deployment or stent design on one hand, and practical computational constraints on the other hand.

5.2 Materials and Methods

5.2.1 Patient-Specific Aneurysm Model

A large patient-specific cerebral aneurysm, with a maximum diameter of 25 mm, was studied after institutional ethics approval was obtained [58,83].

Using 2D DICOM data from a CT scan, the 3D aneurysm geometry was reconstructed in STL format. The in-plane spatial resolution and the inter-plane spacing of the DICOM data has been confirmed to be fine enough to adequately represent the morphology of a cerebral aneurysm [46].

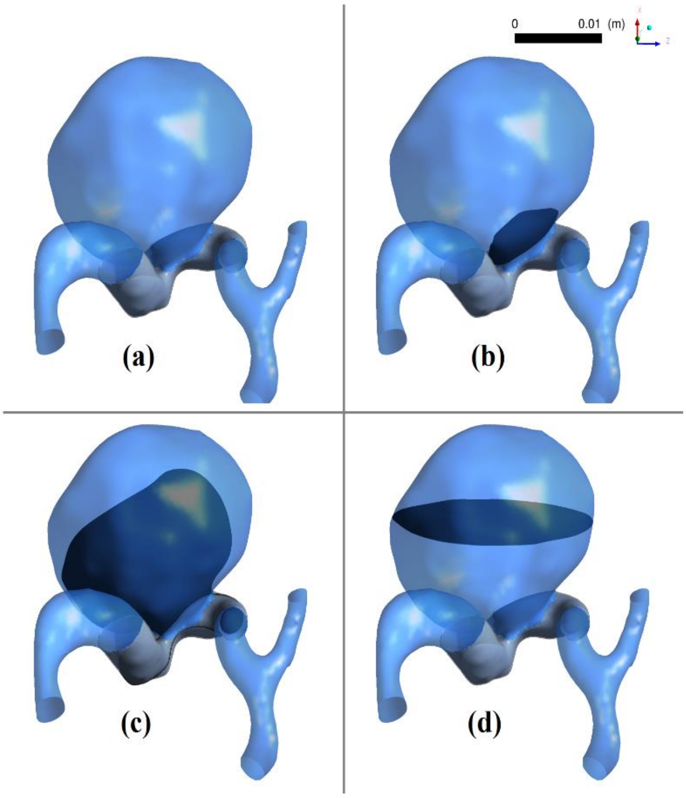

Figure 5-1 Geometry of the cerebral aneurysm and the porous-medium stent, and the positions of each plane of interest: (a) Geometry of the aneurysm and the porous-medium stent model (b) Position of the neck plane (c) Position of the intra-aneurysmal jet plane (d) Position of the intra-aneurysmal centre plane

An intra-aneurysmal centre plane and a jet plane were selected to summarise the simulation results. The positions of the two planes are shown in Figure 5-1.

5.2.2 Porous Medium Method

The 3D virtual FD stent geometry was modelled as a moulded tube, with varied effective diameters, running through the parent artery and covering the aneurysm neck.

In contrast to the conventional stent geometry with individual wires, the FD stent was modelled as a homogeneous PM layer in the simulation. (More details about the methodology of PM stent modelling can be found in Chapter 2.2.2.)

5.2.3 Adjustment of PM Stent Model Thickness

Besides the permeability and the inertial resistance factor, the thickness of a PM stent may also influence the pressure drop, as seen from equation 2-5. This study hypothesised that a different choice of thickness in the model can still provide valid predictions of flow when the flow resistance parameters are correspondingly compensated (Table 5-1), while maintaining the advantages of using a PM model. Hence, the PM stent was constructed in three thickness levels, which were 50, 100, and 200 μm.

Table 5-1 Permeabilities and Inertial Resistance Factors [a]

Thickness, Δe (μm)	Permeability, k (m^2)	Inertial resistance factor, C_2 (1/m)
50	6.22×10^{-10}	1.40×10^{5}
100	1.40×10^{-9}	6.96×10^{4}
200	2.49×10^{-9}	3.50×10^{4}

a. The respective 'initial' values are shown here for each thickness.

5.2.4 Adjustment of Permeability

Initial values of permeability and inertial resistance factor were adapted from a numerical test model of the *Silk* [79], a commonly used single-layer FD stent, listed in Table 5-1. For the three different stent thicknesses, the values of k and C_2 were compensated to maintain a consistent pressure drop across the FD wall (for a given flow velocity, independent of thickness).

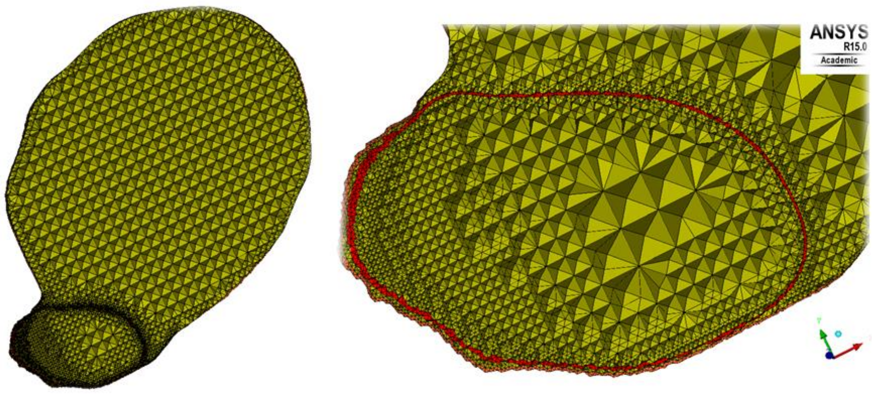

Figure 5-2 Mesh generation for aneurysm model with model FD stent deployed of thickness 50 μm

In order to observe the parametric sensitivity of aneurysmal haemodynamics to permeability, this study considered deviations in the permeability in a series of percentages — 80%, 90%, 100%, 110%, and 120% — of each initial value.

5.2.5 Meshing

A computational mesh dependency test was conducted to assure the accuracy before carrying out all simulations. The entire fluid zone was discretised into 0.7 to 2.8 million tetrahedral elements, with elements in smaller size added to the artery wall and the stent surface, using ICEM (Ansys, U.S.A.). (see Figure 5-2)

5.2.6 Flow Simulation

The blood flow was modelled as a Newtonian, incompressible fluid in the laminar flow regime under steady conditions. To match the characteristics of human blood flow, density and viscosity were specified as 1050 kg/m^3 and 0.0035 Pa·s, respectively.

A mass flow rate boundary condition was set at the inlet for all cases, variously specified to correspond to nominal volumetric flow rates of 150, 250, and 400 mL/min, to observe the permeability sensitivity under different flow rate conditions. A traction free pressure condition was set on the outlets for all cases. The artery wall was described as stationary and no slip. CFD simulation was performed with a commercial finite-volume-method solver, CFX (Ansys 15.0, U.S.A.).

5.2.7 Haemodynamic Parameters

Mass flow rate (MFR) through the aneurysm neck plane was calculated and presented as a percentage (MFR%) compared to the untreated case.

Energy loss (EL) is reported as one of the major factors in the prediction of aneurysm growth and rupture; herein it refers to the difference in fluid energy between the inflow and the outflow across the aneurysm ostium as per,

$$\mathrm{EL} = \sum_{i=1}^{n_{\mathrm{in}}} Q_{\mathrm{in},i}\left(\frac{p_{\mathrm{in},i}}{\rho} + \frac{1}{2}v_{\mathrm{in},i}^2\right) - \sum_{j=1}^{n_{\mathrm{out}}} Q_{\mathrm{out},j}\left(\frac{p_{\mathrm{out},j}}{\rho} + \frac{1}{2}v_{\mathrm{out},j}^2\right), \qquad (5\text{-}1)$$

where Q represents MFR, p is static pressure, ρ is the density of the fluid, v is the velocity, and i and j refer to coordinate locations on the ostium [124,141]. It is also given as a percentage (EL%) of that in the corresponding untreated case [141].

5.3 Results

5.3.1 Effect of PM Thickness on Aneurysmal Haemodynamics, with Compensated Permeability Values

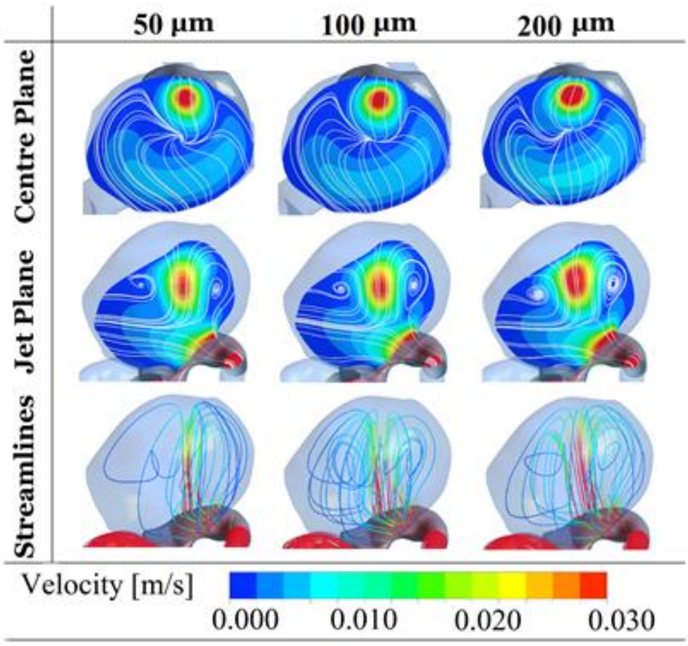

(a)

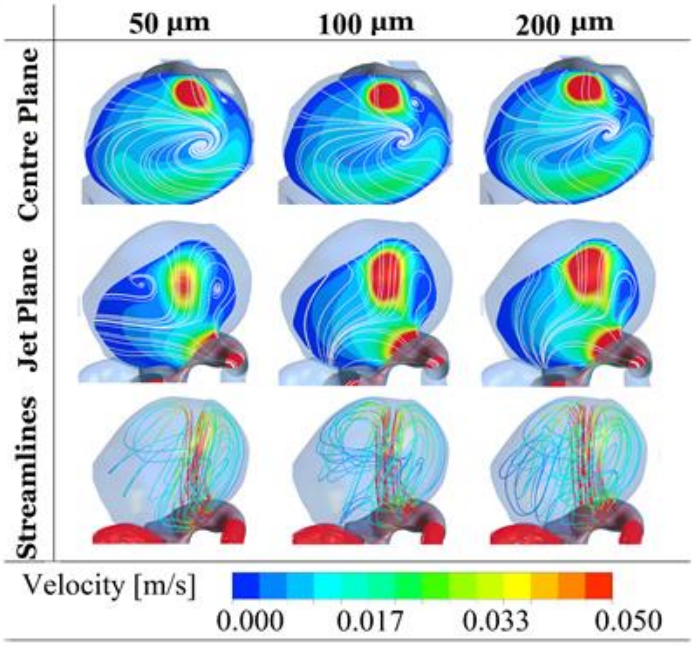

(b)

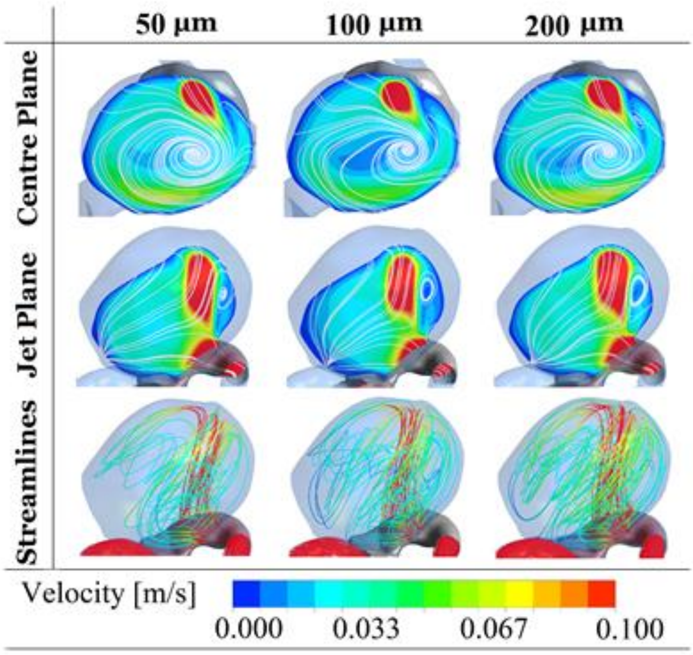

(c)

Figure 5-3 Intra-aneurysmal flow patterns for a porous-medium stent (at 'initial' permeability) with different thicknesses under varied inlet flow rate: (a) 150 mL/min (b) 250 mL/min (c) 400 mL/min

Figure 5-3 demonstrates the flow patterns and velocity contours for PM stents with different thicknesses. The permeability was kept at the 'initial' values (see Table 5-1) for the three cases. Under different inflow conditions, no obvious distinctions between the flow patterns, tangential velocity vectors and contours were observed on either the centre plane or the jet plane in simulations with stent thicknesses of 50, 100, and 200 µm.

Figure 5-4 presents the variations of intra-aneurysmal MFR and EL calculated based on the aneurysm neck plane. For each thickness, the permeability of all cases presented in the chart was the 'initial' value. For a given inlet boundary condition, the maximum difference in MFR% reduction is less than 5 units for the thicknesses of 50, 100, and 200 µm, while the maximum difference for EL% is less than 2 units.

5.3.2 Aneurysmal Haemodynamics for Different Inlet Flow Rates

From the difference in flow reduction rates between different inlet flow conditions, it indicates that the flow reduction efficacy decreases as the inlet flow rate increases (see Figure 5-4). For a given thickness and permeability, when the inlet flow rate increases from 150 to 400 mL/min, the intra-aneurysmal MFR% value is increased by about 18 to 20 units.

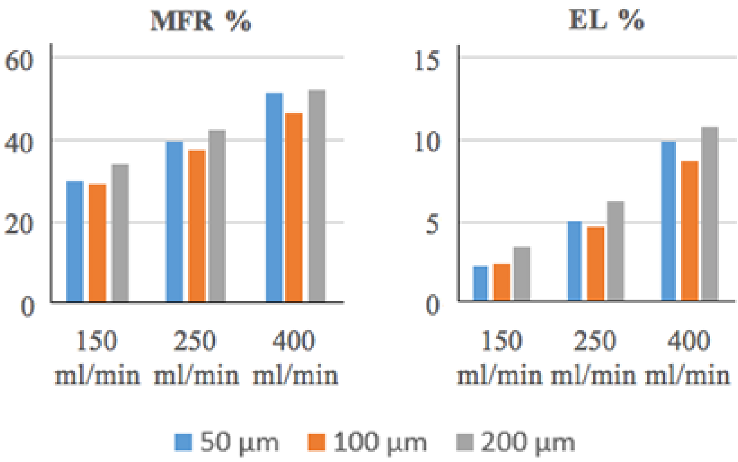

Figure 5-5 MFR% and EL% for different inlet flow rates. (Each PM model is specified with the 'initial' permeability.)

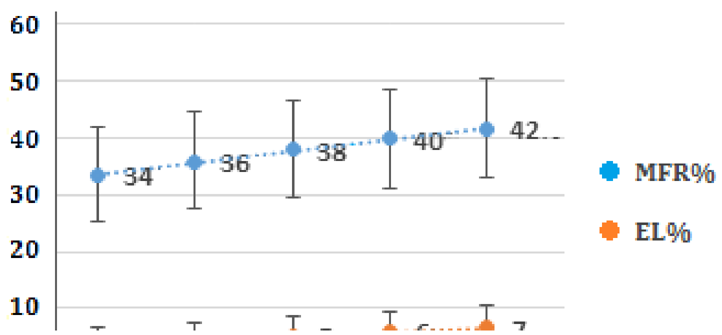

Figure 5-4 MFR% and EL% of cases with modified permeability
(Error bars show the effect of different inlet flow rates.)

5.3.3 Aneurysmal Haemodynamics with Different Permeabilities

Figure 5-5 shows the changes in MFR% and EL% in response to the alterations to permeability. Both MFR% and EL% increase as the permeability rises from 80 to 120 % of the 'initial' value. Each 10 % increment in the permeability resulted in increases of approximately 2 and 1 unit in MFR% and EL%, respectively. The result also reveals that under each inlet boundary condition, the gradient stays similar for both MFR% and EL%.

5.4 Discussion

5.4.1 Effect of PM Thickness on Aneurysmal Haemodynamics, for Compensated Permeability Values

The pressure drop for flow passing through the PM layer can be affected by the layer thickness, even though flow resistance parameters were compensated, as it is easy to imagine that an excessively thick FD layer can interfere with blood flow in the parent artery. This study investigated the possible post-stenting haemodynamic differences caused by FD layer thicknesses of 50–200 μm (none occupies more than 5% of the parent artery diameter), and found no obvious distinctions between them. However, one should be aware of the potential interference if using FD model thickness greater than 200 μm (or layer thicknesses exceeding 5% of the parent artery diameter).

The physical thickness of commercially available FD stents — from a single layer stent (*e.g. Silk*: 30–50 μm), to dual-layer stents, and even treatments using multiple single layer stents (*e.g.* three *Silk* stents: 90–150 μm) [29,79,142] is poorly defined. Nonetheless, the range of FD layer thicknesses in this study covers most of these, and the haemodynamics was insensitive to the choice of thickness provided the flow resistance parameters were suitably compensated beforehand. Therefore, the thickness range of stents employed in this study would be acceptable to be applied in future studies using PM models.

5.4.2 Effect of PM Intrinsic Properties on Aneurysmal Haemodynamics

For a PM, the intrinsic properties such as permeability and the inertial resistance factor can greatly affect the intra-aneurysmal flow patterns. Results indicated that with the increase of PM permeability (from 80% to 120% of the 'initial' values adapted from the literature), the relative aneurysmal inflow increased from 34% to 42%, and the relative aneurysmal energy loss increased from 4% to 7% of the untreated condition. This suggests that the determination of permeability should be well taken care of in simulations using a PM stent model.

5.5 Conclusion

When the thickness of a PM model is adjusted (with compensated k and C_2), within the range of 50 to 200 μm, the aneurysmal flow pattern, velocity magnitude, MFR, and EL are not disturbed by such slight variation relative to the diameter of the parent artery.

The permeability of a PM stent can be related to the porosity of a deployed FD stent. Using a PM to model FD stents of different nominal porosities requires adjustment of the specific permeability setting to properly reflect the flow resistance properties of the represented stent.

Chapter 6

Effect of Calibrated Porous Medium Flow-Diverting Stent Models on Aneurysmal Haemodynamic Modifications

6.1 Introduction

6.1.1 Background

In contrast to modelling the FD stent with fine meshes, which requires a high-resolution spatial discretisation around the stent's thin wires, porous medium (PM) stent models mimic the resistance effect of an FD stent with parameters that characterise a PM, such as permeability (*k*) and inertial resistance factor (C_2) [79,80].

As introduced in Chapter 5, permeability of a PM stent can be related to the porosity of a deployed FD stent. Therefore, when adopting a PM to model FD stents of different nominal porosities, it is critical to characterise the PM property settings to properly reflect the flow resistance of the represented stent.

6.1.2 Current Issue

A number of studies have been performed to understand the correlation between the PM stent and the fine-mesh FD stent model [79–81,83]. To obtain PM model parameters that would be similar to an FD stent, Augsburger *et al.* created an FD test model [79], which had a geometry similar to the commercially available *Silk* FD stent (Balt Extrusion, France), and derived the *k* and C_2 of the test model's PM analogue.

Although the methodology of using PM stent models was established, few studies have been carried out to specify the calibrated PM properties that could match different brands of FD stent available on the market, like the *PED*, *Silk+*, and *FRED* (refer to Chapter 1.1.4). Furthermore, most of the published PM stent studies utilised the PM properties derived by Augsburger *et al.* [79] in the simulation of FD stent treatment even with other brands of device — and indeed often without correctly accounting for the PM model thickness.

6.1.3 Purpose

The objective of this study is to specify calibrated PM stent model parameters for different treatment scenarios — single FD and multi-FD implantation, as well as for treatments with different brands of device (*e.g. PED, Silk+, FRED, etc.*). To meet this need, this study first generated FD test models corresponding respectively to a single *PED*, *Silk+*, and *FRED*, as well as for two *PED* stents (overlaid), and further considered regions or alignments with the lowest and highest porosities for each of these models. The corresponding PM stent model properties — k and C_2 — for each case were derived, and further applied in the CFD simulation of treatments for two patient-specific aneurysms to contrast the effects of different parameters as might realistically be encountered.

6.2 Materials and Methods

6.2.1 Aneurysm Models

Two patient-specific IAs were studied after the institutional ethics approval was obtained. Aneurysm A has a maximum diameter of 25 mm with a narrower neck of about 12 mm; aneurysm B has a maximum diameter of 20 mm with a wider neck of about 15 mm. The 3D aneurysm geometries were reconstructed from sets of 2D DICOM images obtained from CTA scans. The in-plane spatial resolution and the inter-plane spacing of the CTA scans has been confirmed to be fine enough to represent the morphology of the intracranial aneurysms [58].

6.2.2 FD Stent and Test Model Construction

Three commercially available FD stents that are commonly used in clinical treatment — *PED*, *Silk+*, and *FRED* — were studied in this research. The *PED* is a uniform-mesh single-layer stent, comprising 48 wires of 30 μm diameter, with typical porosity from 65 to 70 % *[ref]*. The *Silk+* is also a single-layer stent, but made from 44 thinner wires (25 μm) and 4 thicker wires (40 μm), with a nominal porosity of about 75 to 80 %. The *FRED* is a dual-layer stent, braided from 48 thinner wires (about 25 μm, inner layer) and 16 thicker wires (about 60 μm, outer layer), with a typical porosity of about 70 % [29,30,143–145].

With the above information about the three FD stents, I used a mathematical method to describe the nodal information of the wires' centrelines for these FD stents, when each of them is expanded in a straight cylind tube with the diameter of 4 mm. The 3D virtual FD stents were then generated (see Figure 6-1) by sweeping through all of the nodes on the centrelines, with a circular cross-section in a nominated diameter, using an open source application, Paraview (https://www.paraview.org/) [141] [89].

Based upon the three fully-resolved FD stents, seven scenarios of treatment with either a single FD or two FDs deployed were investigated, and the fully-resolved FD stent test model for each scenario was correspondingly constructed (see Figure 6-2). The seven scenarios include treatment with:

1) a single *PED* (scenario ‘*P*’);

2) and 3) a single *Silk*+ with the maximal/minimal metal-coverage ratio (MCR) (scenario ‘*S-max*’ and ‘*S-min*’);

4) and 5) a single *FRED* with the maximal/minimal MCR (scenario ‘*F-max*’ and ‘*F-min*’);

6) and 7) two *PED*s with the maximal/minimal MCR (scenario ‘*DP-max*’ and ‘*DP-min*’) achieved within the aneurysm ostium.

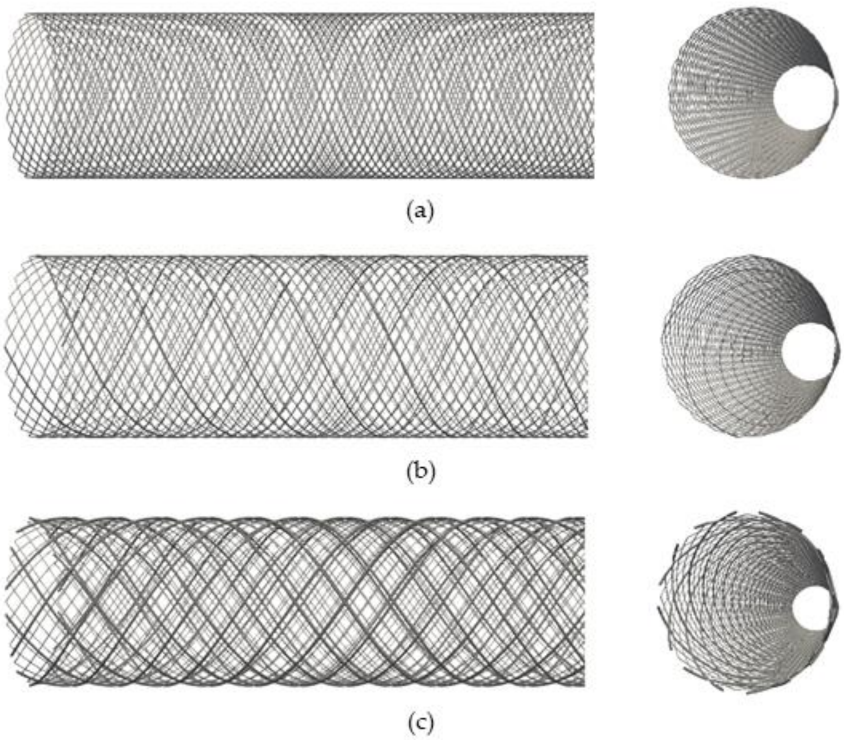

Figure 6-1 Sketch of the fully-resolved FD stents: (a) *PED* (b) *Silk*+ (c) *FRED*

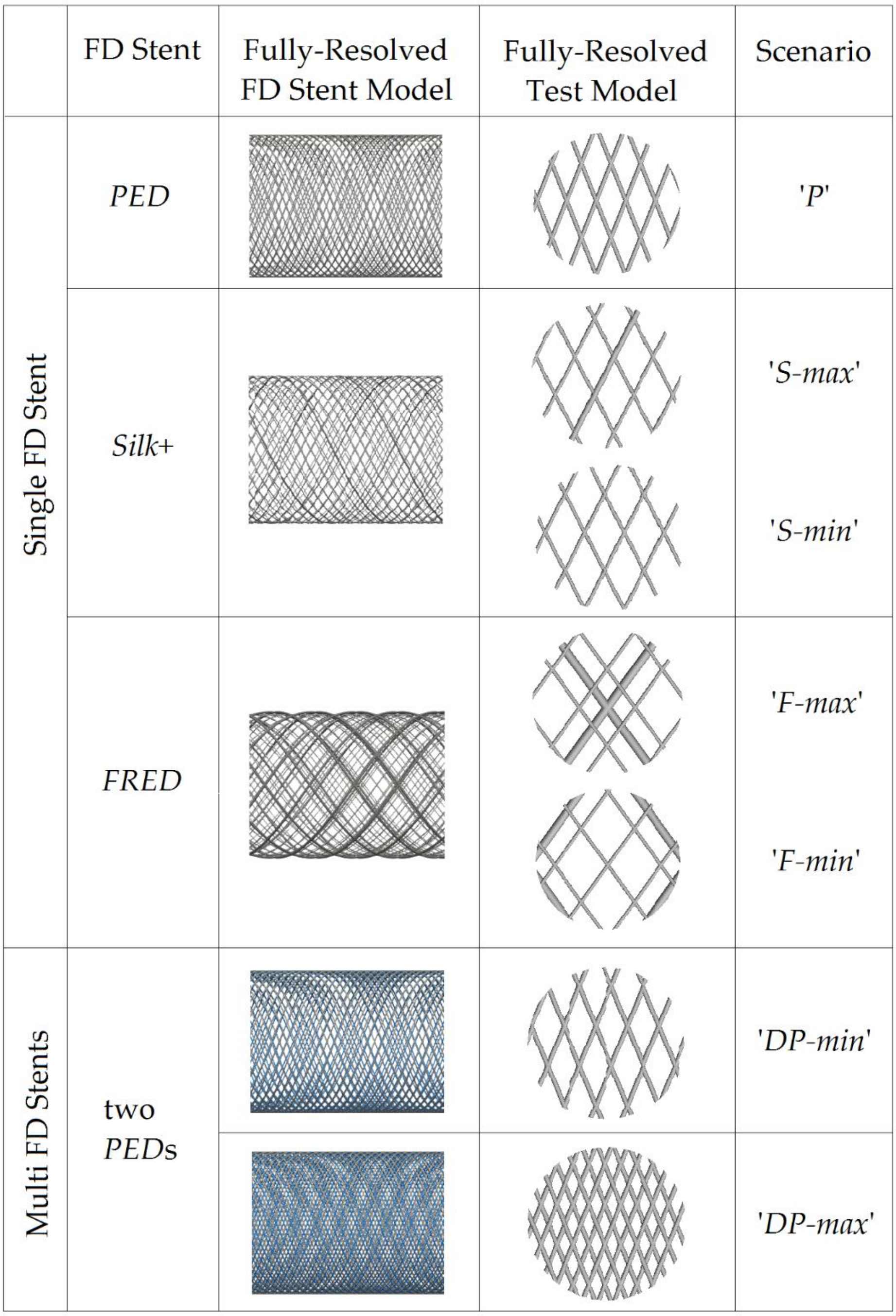

Figure 6-2 Sketch of the corresponding fully-resolved test model scenarios for each FD stent. Scenario names ending with '*-max*' or '*-min*' respectively denote the test models with maximal or minimal MCR.

6.2.3 Determination of PM Properties and Construction of PM-FD Models

The properties (k and C_2) of each PM-FD model were determined based upon the test model generated from the corresponding fully-resolved FD stent. This technique was adopted from a previous study by Augsburger *et al.* [79].

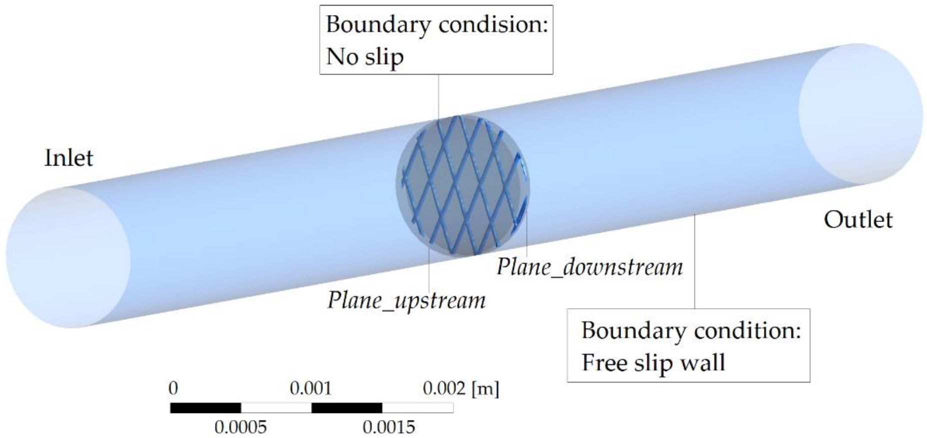

Figure 6-4 Simulation condition of the test model (*PED* is used as an example in the figure)

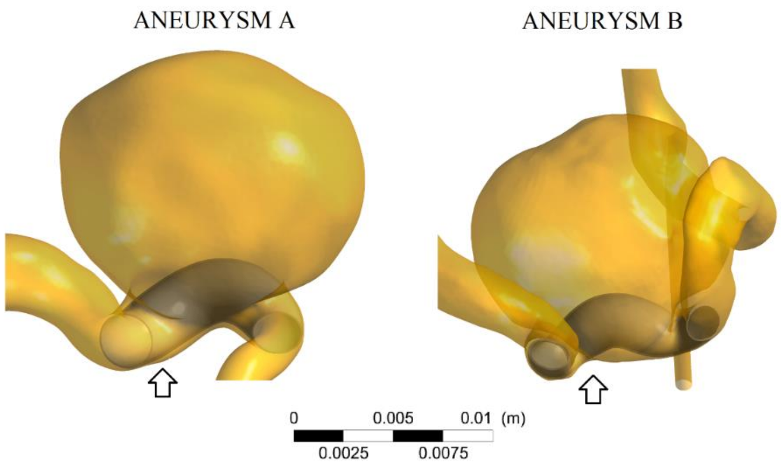

Figure 6-3 Specific shape of the PM tube running through the parent artery of each aneurysm

To measure the flow damping effect of FDs deployed in the seven scenarios, a series of CFD simulations were performed, with different velocity boundary conditions (0.05, 0.1, 0.25, 0.5, and 1 m/s) imposed at the test models' inlets. A free-slip boundary condition was adopted for the flow channel in the test model, and a no-slip condition for the fully-resolved FD stent surface to avoid undue influence of the flow channel walls, as shown in Figure 6-3. Two planes respectively at the upstream and downstream of the wires were selected for the calculation of pressure drop.

To simplify the wire-FD model in aneurysmal haemodynamic simulations, the FD stent was modelled as a tube running through the parent artery of each aneurysm (see Figure 6-4), with a constant thickness of 150 μm. (It has been demonstrated that a PM model thickness of 150 μm can be used to accurately represent the flow resistance of

FD stents of various thicknesses in Chapter 5, provided that k and C_2 are appropriately adjusted.) The shapes of the PM models used in this study were extracted from the stent model deployed in the previous study [141].

6.2.4 Flow Resistance of the PM Model

The flow resistance created by the PM layer — which varies with respect to its intrinsic properties, k and C_2 — is expressed as a momentum source term in addition to the standard fluid equation,

$$S_i = -\left(\frac{\mu}{k} v_i + C_2 \frac{1}{2} \rho |\boldsymbol{v}| v_i\right), \tag{6-1}$$

where i represents the x, y, or z coordinate, $\boldsymbol{v}$ is velocity, μ is viscosity, and ρ is density [79,83].

The S_i term contributes to the pressure drop across the PM layer due to flow. Therefore, the correlation between pressure drop and one-dimensional velocity through the PM layer can be simply represented as the second order polynomial equation

$$\Delta p = \frac{\rho \cdot C_2 \cdot \Delta e}{2} v^2 + \frac{\mu \cdot \Delta e}{k} v, \tag{6-2}$$

where Δe is the thickness of the PM model.

By fitting a quadratic curve to pressure drop data as a function of velocity for each test model, in the form

$$\Delta p = a\, v^2 + b\, v, \tag{6-3}$$

the values of C_2 and k can be estimated from the corresponding parameters a and b.

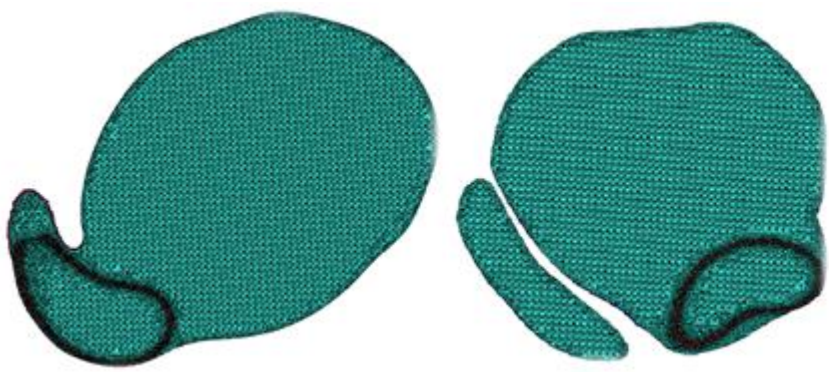

Figure 6-5 Mesh generation for aneurysm A (left) and B (right)

6.2.5 Meshing

The fluid domain and the PM subdomain were discretised into around three million tetrahedral elements in total using ICEM CFD (ANSYS, U.S.A.), with finer elements of less than 0.2 mm in size defined on the aneurysm surface and PM subdomain (see Figure 6-5).

6.2.6 Flow Simulation

To describe a blood-analogue fluid in the simulation, the density and dynamic viscosity were specified as 1050 kg/m3 and 0.0035 Pa·s. The blood flow was assumed to be an incompressible Newtonian fluid within a laminar regime under steady condition. The inlet boundary condition was specified with volume flow rates of 150 mL/min, 250 mL/min and 400 mL/min, respectively. A traction free pressure condition was nominated on the outlets for all cases. The artery wall was defined as stationary, with a no-slip condition. CFD calculations were carried out using a finite-volume-method (FVM) solver in CFX (ANSYS 15.0, U.S.A.).

6.2.7 Haemodynamic Parameters

MFR and EL through the aneurysm neck were calculated to measure the flow-diversion efficacy in each scenario. More details about the calculation of EL can be found in Section 5.2.7.

6.2.8 PM Model Validation

To confirm the accuracy of the calibrated PM model proposed in the present study, a validation was carried out to compare the outcomes between the calibrated PM model and a virtual stent deployment (VSD). Flow-diversion results of two aneurysms into which *Silk* stents were deployed were studied, under various inflow conditions (low, medium, and high). The *Silk* stents were respectively modelled as the calibrated PM model *'S'* and as the VSD model that was introduced in the previous published results [141].

6.3 Results

6.3.1 Porosity and Pore Density of Test Models

The porosity and pore density of each test model (Table 6-1) were calculated to compare the structures of different FD model geometries. For the test models representing the *Silk+*, *FRED*, and two *PED*s, the mean porosities and pore densities were also calculated by averaging the values for maximal and minimal MCR (see Table 6-1).

Table 6-1 The porosity and pore density of each test model. The mean values for the *Silk+* stent, *FRED* stent, and the two *PED*s obtained by averaging the two scenarios* are also shown.

FD stent	Test model scenario	Porosity (%)	Mean porosity (%)	Pore density (1/mm²)	Mean pore density (1/mm²)
PED	P	70	70	22	22
Silk+	S-max	76	80.5	20	19.5
	S-min	85		19	
FRED	F-max	70	71.5	22	19
	F-min	73		16	
Two *PED*s	DP-max	46	58	70	46
	DP-min	70		22	

* Scenarios ending with '-max' and '-min' respectively relate to the maximal and minimal MCR.

6.3.2 Relation between Pressure Drop and Inflow Velocity

Figure 6-6 depicts the variation of pressure drop as a function of velocity for flow through each of the different test models, based on a series of CFD simulations using the fully-resolved geometries.

As the velocity is increased from 0 to 1 m/s, each test model exhibits higher resistance to the flow, indicated by the increasing pressure drop. Indeed, the rate of increase in resistance also grows as velocity increases, consistent with a quadratic relation. Flow through two *PED*s (scenario '*DP*') engendered the highest average pressure drop of up to 1720 Pa. The pressure drops produced by the single-stent models all varied in a range roughly half as large as the average for scenario '*DP*': the *PED* (scenario '*P*') created a pressure drop of 955 Pa, followed by 797 Pa for *FRED* (scenario '*F*') and 567

Pa for *Silk+* (scenario '*S*'). A remarkable difference in the pressure drops was revealed for scenario '*DP*' and scenario '*S*', whose averages differed by a factor of three at the highest velocity.

Table 6-2 presents the coefficients of the quadratic term (*a*) and the first order term (*b*) in equation 6-3, which are obtained by fitting curves to the data in Figure 6-6, representing the relationship between the average pressure drop and velocity for the four scenarios. Based on these paired coefficients, k and C_2 for each scenario was respectively derived, corresponding to the PM model thickness of 150 μm, to characterise the PM-FD stent.

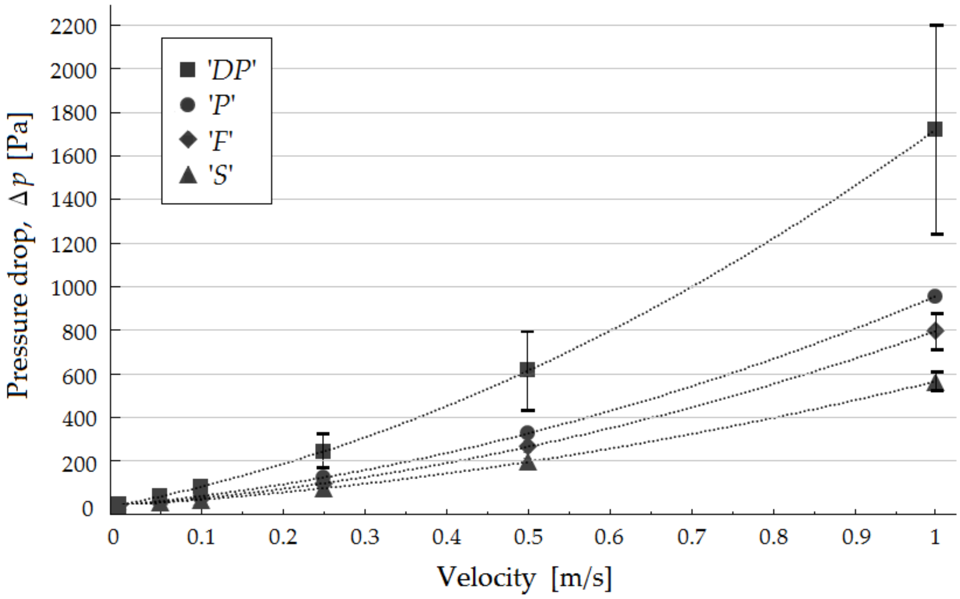

Figure 6-6 The relationship between pressure drop and inflow velocity for flow through each test model. For curves '*F*', '*S*', and '*DP*', the error bars represent the span of pressure drop between the '*min*' and '*max*' MCR for the selected scenarios, and the curves are plotted based on average values of these limits.

Table 6-2 Paired coefficients (*a* and *b*) and PM model parameters (*k* and C_2) derived from test models representing each FD stent scenarios

FD stent scenarios	Coefficient*		Permeability, k [m²]	Inertial resistance factor, C_2 [1/m]
	a	b		
P	598	360	1.46×10^{-9}	7.60×10^{4}
F	526	273	1.92×10^{-9}	6.68×10^{4}
S	339	230	2.29×10^{-9}	4.30×10^{4}
DP	978	744	7.06×10^{-10}	1.24×10^{5}

* The coefficients in equation 6-3, which are obtained from the curves representing the relationship between pressure drop and flow velocity for each test model in Figure 6-2.

6.3.3 Visualisation of Aneurysmal Flow Pattern

Figure 6-7 presents the velocity iso-surfaces, streamlines, and the WSS for aneurysm A (Figure 6-7(a)) and B (Figure 6-7(b)) under the untreated condition, and for treatment according to the four different FD stent scenarios.

Results indicate substantial flow reduction occurred in the aneurysms following treatment with single PM-FD stents (scenarios '*P*', '*S*', and '*F*'), compared to the untreated cases. Further flow diversion was achieved in scenario '*DP*', as both inflow velocity and WSS were further reduced. Differences in the magnitudes of velocity and WSS can be noted from the flow visualisations for scenarios '*P*', '*F*', and '*S*', while the inflow direction and WSS distribution are similar (see Figure 6-7).

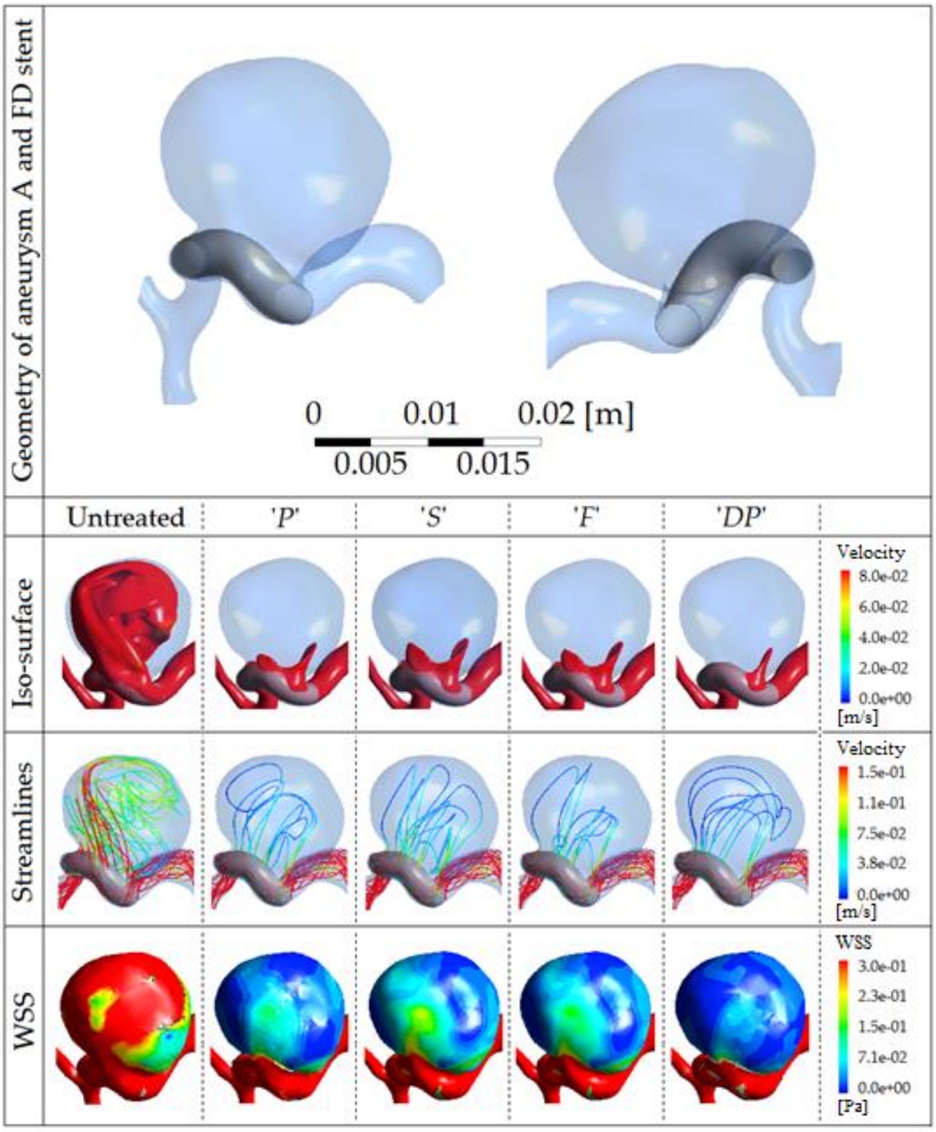

(a)

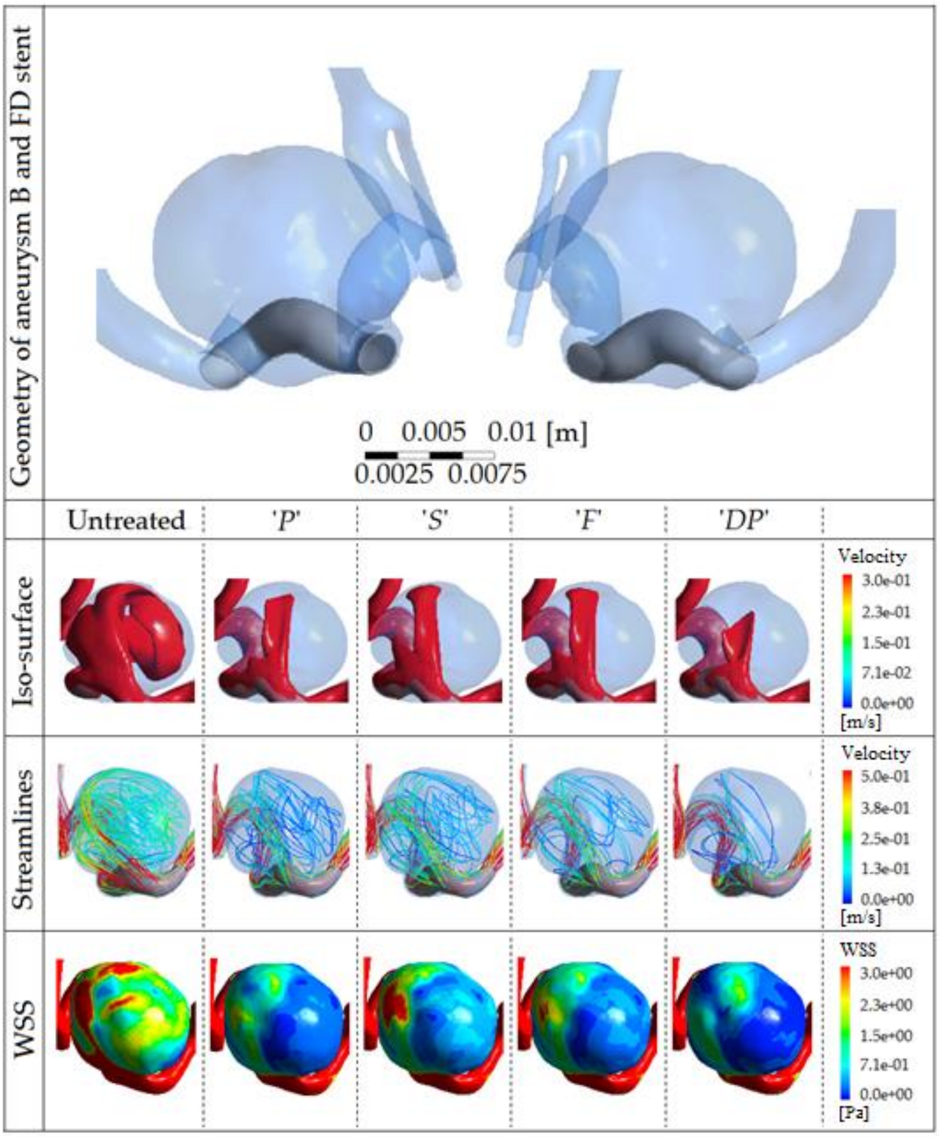

(b)

Figure 6-7 Visualisation of aneurysmal haemodynamics for aneurysm A and B, characterised by velocity iso-surfaces, streamlines, and WSS, under the untreated condition and under four different scenarios of FD stent treatment: (a) aneurysm A (b) aneurysm B

6.3.4 Quantitative Aneurysmal Haemodynamics

Figure 6-8 shows the quantitative results from two aneurysms treated with different FD stents, modelled as PM with calibrated properties. In Figure 6-8(a) the MFR is presented as percentages of the corresponding untreated cases. For the inlet flow rate of 250 mL/min, the MFR after treatment scenario '*DP*' is obviously lower than that of the other scenarios ('*P*', '*F*', and '*S*') by up to 19 and 18 percentage points in aneurysms A and B, respectively. The difference in MFR between the single-stent scenarios '*P*', '*F*', and '*S*' does not exceed 9 percentage points (relative to the untreated cases); among them, scenarios '*P*' and '*S*' respectively show the highest and lowest efficacies of flow diversion, with scenario '*F*' being intermediate. I observed the same tendencies for inlet flow rates of 150 and 400 mL/min, which are represented by the lower and upper error bars in Figure 6-6.

Figure 6-8(b) presents EL as percentages of the corresponding untreated cases. Broadly speaking, the EL results follow the same trends as outlined above for MFR. Values of EL for the different FD test models differed by up to 5 and 14 % (relative to the untreated cases) in aneurysms A and B, respectively. There are, however, two notable distinctions. Firstly, there is a much greater difference in values of relative EL between the two patient-specific aneurysms. This suggests that EL may be more sensitive to

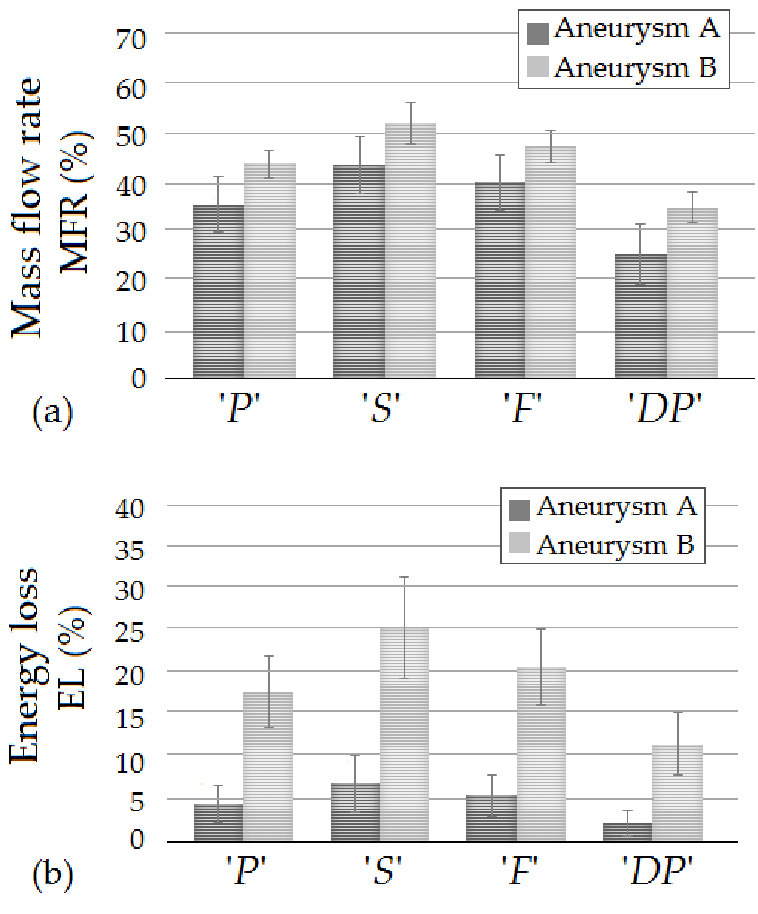

Figure 6-8 Quantitative aneurysmal haemodynamic results for aneurysm A and B under different treatment scenarios. The MFR (a) and EL (b) are given as the percentage of the corresponding untreated case. Bar heights represent the inlet flow rate of 250 mL/min, while the lower and upper error bars extend to results for 150 or 400 mL/min. A plane across each aneurysm neck is selected for the calculation of MFR and EL.

morphology than MFR. Secondly, the relative size of the 'error bars', representing variation due to changes in inflow, is considerably larger for EL. Thus, normalised EL is also more sensitive to inflow rate than is the normalised MFR. Absolute values of MFR and EL for each untreated case are shown in Appendix III.

6.3.5 Flow-Diversion Efficacy in Two Patient-Specific Aneurysms

A difference in the flow-diversion efficacy between two aneurysms was observed, even when the aneurysms were treated with the PM-FD stent in the same scenario (Figure 6-7 and Figure 6-8).

As indicated by the velocity iso-surfaces in Figure 6-7, while the inflow to aneurysm A is largely reduced after the PM-FD stent treatment, a relatively strong inflow remains in the correspondingly treated aneurysm B. For a quantitative comparison, Figure 6-8 shows that for a given treatment scenario the flow-diversion efficacy characterised by MFR and EL has a marked difference of up to 10 and 18 percentage points, respectively, between the two aneurysms.

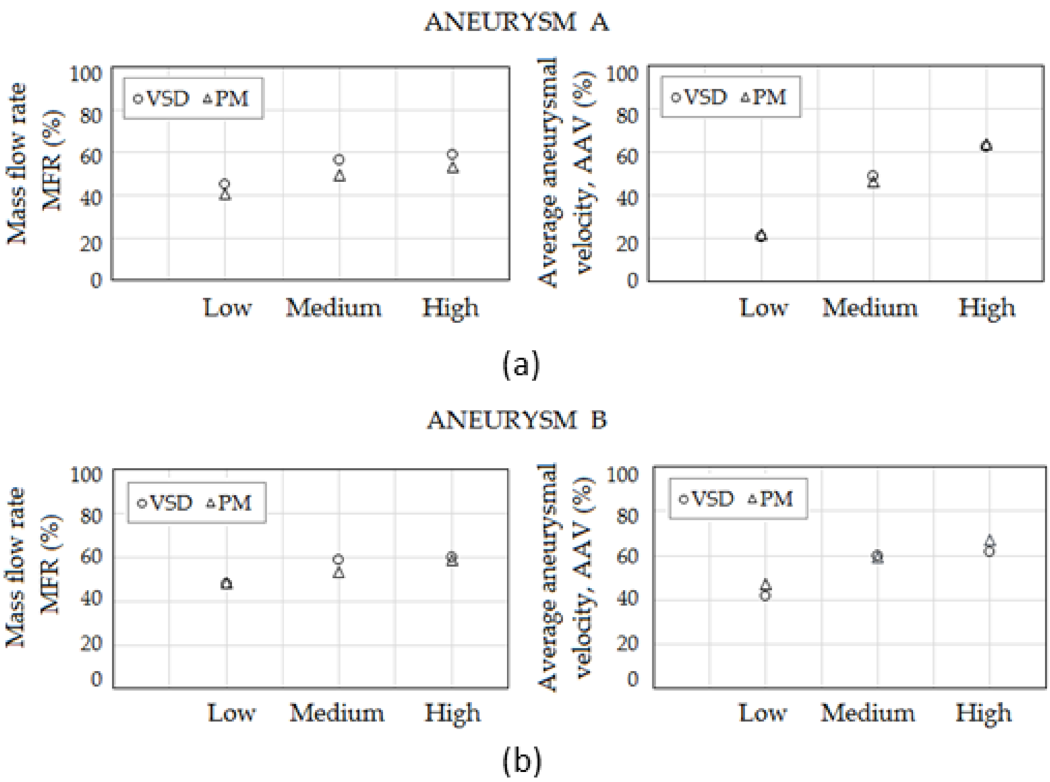

Figure 6-9 Comparison of MFR% and AAV% obtained from two FD modelling approaches — the VSD model [103] and the PM model (present work) — under various inflow conditions, (a) for aneurysm A and (b) for aneurysm B.

6.3.6 Comparison of Simulation Results between PM and VSD Model

Quantitative haemodynamic parameters of MFR and average aneurysmal velocity (AAV) have been calculated, and the maximal differences in these parameters between the two FD modelling approaches (the calibrated PM and the VSD) was found to be less than 5% (Figure 6-9). This result indicates the credibility of using the calibrated PM method in flow simulations of IAs implanted with FD stents.

6.4 Discussion

Using the method of modelling a FD stent as a PM, this study provided a set of parameters for PM-FD stent modelling in CFD simulation, in order to realistically reflect the distinct flow diversion effects. Based on three FD stents available on the market, this work has studied seven scenarios of fully-resolved FD stent deployment, and derived four characterised PM-FD stent models representing the true FD stent deployments, including a dual-stent model. Moreover, the corresponding stent treatments for two patient-specific aneurysms have been simulated in eight different cases.

Through the use of calibrated PM-FD stent models, this study demonstrates a method that is capable of distinguishing the haemodynamic effects associated with different FD stents while retaining the advantages of using a PM model to avoid simulation difficulties as well as to save computational time.

6.4.1 Characterising PM-FD stents

Figure 6-6 demonstrates that the flow resistance induced by the test models varies according to their individual designs. In comparison to the flow resistance induced by scenario '*P*', scenarios '*F*' and '*S*' produced resistances about 20 and 40 percentage points lower, respectively; while scenario '*DP*', as a double-stent deployment, enhances the resistance to around twice that of scenario '*P*'. Clearly there is a dominant inverse relationship between flow resistance and porosity, although this does not explain all of the variation observed — compare the pressure drops for scenarios '*P*', '*F-max*' and '*DP-min*', which all have porosities of 70 % (Table 6-1). The differences in flow resistance from these test model scenarios with identical porosity are considered to be substantially affected by the differences in the stent thicknesses. As the stent thickness increases, it creates a stronger damping effect on the flow. Knowing that the effective stent wire thickness gradually reduces from two *PED*s (‘*DP*’) to *PED* (‘*P*’) and *FRED* (‘*F*’), a correlation between the resistance induced by the stent wires and their effective thicknesses can be noted. This reinforces the contention that the PM model properties, particularly k and C_2, should be calibrated if they are intended to represent true FD stents, as they control the capability of the PM model to transmit fluid, thereby determining the real flow resistance.

As can be identified by the positions of the error bars (scenario ‘*S-max*’, ‘*S-min*’, ‘*F-max*’, ‘*F-min*’, ‘*DP-max*’, and ‘*DP-min*’) in Figure 6-6, even though the pressure drops created by scenarios with different MCRs fluctuate within a range, this range is smaller than the differences between the various stents, and there was no overlap of the error bars. Thus, it is reasonable to believe that the PM-FD stent models defined with k and C_2 derived from the respective regression curves can represent the flow-diversion effects of the fully-resolved FD stents for typical deployment of these stents. (Of course, deployments involving oversized stents, undersized stents, or deliberately enhanced ‘compaction’ that result in drastically different average MCR values could affect the relative flow resistances imposed [141].)

The phenomenon of different flow resistance follows from the structure of the FD stent models, *i.e*. the porosity and the wire structure [90]. These results further illustrate the tendency of flow resistance to decrease when the porosity of a FD stent is increased (see Table 6-1). As specific examples of this, the smallest porosity decrease of 1.5 (scenarios ‘*F*’ and ‘*P*’) corresponded to an increase of 20 % in flow resistance, while the largest porosity decrease of 22.5 % (scenarios ‘*DP*’ and ‘*S*’) corresponded to an increase of 200 % in flow resistance.

6.4.2 Impact of Different PM-FD Treatments on Aneurysmal Haemodynamics

Modelling the fully-resolved FD stent as a PM model avoids the procedure of modelling the deployment process of the FD stent, accounting for the expansion, compaction and other motions of the individual wires, which is challenging and time-consuming. As the PM-FD stent modelling introduced in this study simplifies the fully-resolved stent structure into a moulded tube with a constant thickness, it avoids the requirement of high-resolution discretisation around the wires (which would result in a large number of tiny computational elements), thereby relieving the simulation burden and saving computational time. The choice of a 150 μm thickness for the PM model (rather than, say, 30 μm) likewise saves on computational load, without any significant sacrifice in accuracy [79].

In this study, to simulate FD stents deployed to treat patient-specific aneurysms using PM models, the entire fluid zone was discretised into about three million mesh elements across different cases, which has even more precision than that used in the simulation by Augsburger *et al.* [79], ensuring the capability to accurately predict the flow haemodynamics. Using eight cores on an ordinary desktop computer, the simulation time is around half to four hours for different scenarios under various inlet flow rates, when the convergence criteria were adopted as 10^{-5} for relative residuals. Comparing this to the previous simulations with fully-resolved FD stents, which typically takes about five hours using 16 cores on a high-powered Z840 workstation [141], the computational efficiency is evidently improved substantially. This finding is consistent with the trend that PM models will generally be substantially more computationally efficient, as also found by Augsburger *et al.* [79].

Having this computational advantage and using these sets of the calibrated coefficients to define PM stents, it improves the practicability of simulation for these devices. The derived parameters presented in this work make it possible for simulation to be carried out immediately, thus the approximate flow-diversion efficacy can be estimated for a given aneurysm treated with any such device. This result is a ground-breaking contribution to the field of FD treatment planning, as it not only ensures simulation accuracy but also significantly improves the simulation efficiency. The improved specifications in our PM models and the reduced time cost would be highly beneficial.

6.4.3 Limitations and Future Work

With the test models that represent different fully-resolved FD stents, this study derived the characterised parameters (k and C_2) for each PM model; in this way, the stent models were defined as a homogeneous PM layer with isotropic k and C_2.

Due to the interaction between the aneurysm neck morphology and stent expansion, the true wire configuration varies with the individual stent deployment, thereby resulting in unevenly distributed wires and hence local variations in porosity and pore density. However, our PM models did not account for such non-uniformity. Besides that, the shape adopted by the stent wires can be affected by the artery diameter, the selected stent size, and the compaction force applied, resulting in increased or decreased porosity. The potential effects of these factors on porosity should also be noted in PM stent modelling. Even though the specification for each PM model may not perfectly match the true deployment, the same method was consistently used across all the different scenarios in this study. Therefore, the relative differences between each scenario are still capable of representing the distinct flow-diversion effects of the real FD stents. It is the future work to establish further sophisticated PM-FD stent models.

In this study, the PM model parameters were derived from test models with perpendicular inflow, while the direction of realistic aneurysmal inflow varies locally. It is also the future plan to study the anisotropic parameters for more precise PM stent modelling. As reported in a previous study, the pressure drop across the stent mainly results from the perpendicular velocity component, with minimal influence of the tangential component [90]. This may allow a simplification to be introduced in some models.

The pulsatile phenomenon was not considered in this study, as the flow-diverting treatment is performed in intracranial vessels where the pulsatile phenomenon has less effect on the variation of the artery wall geometry, comparing to that of cardiovascular vessels. Other studies have also demonstrated that despite small variations of the local vorticity due to the pulsatile flow behaviour, steady flow simulation provides a good approximation of spatial average velocity magnitude in IA [132], and the instantaneous shear stress and flow rate in a pulsatile flow regime can be estimated reasonably well from a steady flow simulation [133]. It is also reported that steady-state models provide reasonable estimates for the time-averaged haemodynamics of true pulsatile flow [134]. However, it would be interesting to evaluate the variation of aneurysmal inflow —although tiny— due to the pulsatile phenomenon. Aneurysmal inflow variation due to the parent artery flowrates can be estimated in this study from the MFR difference at various simulation conditions of flowrate, whereas the instantaneous behaviour over a cardiac cycle would require the future establishment of a time-dependent PM model.

6.5 Conclusion

In this study, I generated seven test models based on the designs of three commercially available FD stents on the market (*PED*, *Silk+*, and *FRED*), and studied the corresponding k and C_2 used for the PM stent modelling to represent the true flow-diversion effect of the given FD stents.

This study revealed up to three times difference in flow resistance created by different PM-FD stents, resulting in up to 19 (MFR) and 14 (EL) percentage points difference in the aneurysmal haemodynamics for the stented cases, which indicates the capability of distinguishing and representing the flow-diversion effect of different FD devices using PM-FD stent models.

This work provides a vital foundation for the future development of PM models. Both the reported different flow resistances from various stent designs and the factors that may affect the stent performance have provided solid evidence for future studies to further optimise the flexibility and precision in using PM models.

With the specific settings of PM properties, this study demonstrates the advantages of FD stent simulation using PM models, by providing medical doctors and other researchers with an individualised method that is more efficient than fully-resolved

CFD simulations while also achieving better simulation accuracy than with uncalibrated PM models.

Chapter 7

Conclusions and Outlook

7.1 Conclusions

From results obtained in previous chapters, the morphologic characteristics and simulation parameters that may affect the simulation credibility of aneurysmal haemodynamics have been inspected. The capability of CFD to predict fluid flow variations in idealised and realistic aneurysm geometries, with or without FD stent treatment has been checked. Furthermore, a set of parameters, after being calibrated to a variety of treatment modes, has been provided to future studies using model FD stents.

To sum up, with computational modelling of idealised aneurysms, reconstructed patient-specific aneurysms, and model FD stents, haemodynamic investigation of IAs and their flow-diversion treatments were carried out, which contributes to a more comprehensive and valid understanding of the aneurysmal haemodynamics and the flow-diversion effects.

In Chapter 3, the accuracy and validity of CFD predictions of aneurysmal haemodynamics without FD stent intervention was discussed, by comparing the resolved velocity vector field in a patient-specific aneurysm with different experimental fluid dynamics methods, such as PIV and PCMRI. The simulation and experiments were carried out under the same flow regime and boundary conditions. To carry out a comparison between different methods with minimal influence result from unavoidable morphological errors, advanced techniques were used in the research scheme, like microCT scanning and 3D reconstruction. In that way the *in vitro* silicone phantom was precisely scanned, the results of which were later reconstructed into a 3D virtual model. General comparison between CFD, PIV and PCMRI shows the same vortex flow at the centre of the aneurysm; however, the near-wall flow pattern shows discrepancies in the PCMRI results, which is considered as a consequence of the low spatial resolution used in PCMRI measurement. The 2D velocity vector field comparison between PIV and CFD shows good similarities both in flow pattern and velocity magnitude, while similar 3D streamlines in the centre of aneurysm—the vortices—are observed by comparison between PCMRI and CFD.

In Chapter 4, the validity of CFD predictions for aneurysmal haemodynamics modified by the presence of a *Silk* FD stent was further checked, by comparing the 2D velocity vector field in a patient-specific aneurysm with that measured by PIV. Further, the FD stent modelled as a PM layer was also validated against experimental results for the first time, with PM model properties defined following the k and C_2 derived from a *Silk* stent introduced in Augsburger's report [79]. Comparison between PIV and CFD results shows very good similarities in the velocity vector field for the untreated case and acceptable similarities for the stented case.

Through these two chapters, assessment of the accuracy of CFD predictions of aneurysmal haemodynamics before and after FD stent treatment has been confirmed. CFD can be a reliable tool that accurately predicts the aneurysm haemodynamics, provided that the materials and parameters used in simulation are reasonably controlled and determined, for example, the precision of the reconstructed model, the adoption of reasonable simulation parameters, the reproduction of a stable and consistent flow environment, *etc*. Moreover, the matched flow variations after flow-diversion treatment indicate that the use of a PM model FD stent in CFD is a convenient and flexible tool for investigating the flow fields in treated aneurysms.

In Chapter 5, impacts on aneurysmal haemodynamics were investigated when the PM model stent is designed with various thickness within a certain range, as well as the corresponding adjustment of k. Aneurysmal flow patterns and velocity magnitudes are found to be similar between PM models of different thicknesses (between 50 and 200 μm), provided that k and C_2 are compensated to retain the same pressure drop. The adjustment of k has been found to strongly influence the flow-diversion effect of the PM model.

In Chapter 6, PM model FD stents were respectively calibrated to reflect the flow resistance created by several treatment modes using commercially available FD stents. Flow-diversion effects of such calibrated PM model FD stents were further compared between different treatment modes in two patient-specific aneurysms. From the results, up to 20 % variation in flow-diversion effects can be observed between different calibrated PM model FD stents.

Through these two chapters, PM model FD stents have been calibrated to study the aneurysmal haemodynamics after FD stent treatment. The thickness of the PM model (within the range of 50 to 200 μm studied in this thesis) has been found to have negligible influence on the aneurysmal haemodynamics while the k and C_2 are compensated to retain the relevant pressure drop. This assures the benefit of using a PM model stent in the procedure of mesh generation, for the reduced difficulties and improved mesh quality; furthermore, the computational cost in both time and equipment can be saved apparently. From the correlations between pressure drops and imposed velocities for the treatment modes that have been studied in this research, several pairs of calibrated parameters—k and C_2—can be derived for characterising the PM model FD stents in future studies. According to the simulation results with calibrated model stents, flow-diversion effects reveal significant variations with respect to different PM model stents, which suggests the importance of calibrating model FD stents to match with the represented FD stents. Having this computational advantage and using these sets of the calibrated coefficients to define PM stents, it improves the practicability of simulation for these devices. Compared to fully-resolved stent simulation, time required for computational model preparation and simulation in PM model simulation is substantially reduced. This study demonstrates the advantages of FD stent simulation using PM models, by providing medical doctors and other researchers with an individualised method that is more efficient than fully-resolved CFD simulations while also achieving better simulation accuracy than with uncalibrated PM models.

Overall, these studies certainly contribute to an improved validity of aneurysmal haemodynamics simulation, thereby enhancing the clinical relevance of such aneurysmal haemodynamic studies in the future.

7.2 Outlook

Several questions that have been raised from studies in this thesis could be considered as future research directions, which include:

1) More advanced settings for experimental methods can be adopted to study the fluid flows. 3D PIV, which requires two high-speed cameras could provide 3D planar velocity results, while a volumetric PIV measurement, which requires four cameras, could further investigate the flow movement in the entire 3D flow field. Besides, PCMRI performed with improved resolution, or using a scaled-up aneurysm model with correspondingly adjusted flow conditions (like inflow rate, Reynolds number, *etc.*) could help to precisely resolve a 3D flow field (even 4D with the time frame) with more accurate details. Such results would contribute to a more convincing comparison of the resolved flows between numerical and experimental approaches, as the simulated flow results could be validated in a more comprehensive scheme with both 2D and 3D results.

2) More patient-specific aneurysm models can be included. A larger sample size consisting of different parent artery and aneurysm morphologies would increase the range of flow complexities, thereby leading to a comprehensive examination of the power of each fluid dynamic method when facing various flow fields. Besides, flow-diversion efficacy affected by the aneurysm morphology can be further discussed. This finding holds potential to contribute to the prediction of treatment effects for aneurysms with specific morphologic characteristics.

3) More FD stent treatment scenarios can be considered in the calibration of PM stent modelling. Since different wire structures resulting from various FD stent treatment modes would lead to different resistance to the aneurysm inflow, the derivation of a series of parameters for the PM model stent to replicate the flow resistance would enhance the practicability and effectiveness of using PM models in the simulation of flow-diversion efficacy. Porosity and pore density are critical factors to describe stent wire structures: the correlation between them and PM model parameters is therefore promising information to allow the PM model to be broadly used in future studies, to assist the haemodynamic simulation of aneurysms with a FD stent deployed.

4) More sophisticated PM stent model can be designed with consideration of the inhomogeneous and anisotropic PM model parameters. Due to the interaction

between the stent structure and the artery morphology, the actual wire structures distributed across the aneurysm neck should be various and unevenly distributed, leading to inflows in different directions affected by the local wires. Thus, a PM stent model designed with inhomogeneous flow resistance and anisotropic PM parameters could more realistically represent the local force created by individual stent wire structures.

5) A comprehensive quantitative analysis of the shifts of flow distribution between different flow-diversion treatment modalities, as well as between more advanced CFD models considering the local resistance variations in the stents, would provide useful information to optimise the CFD models for them to precisely predict fluid flow behaviours, and thereby assist the clinics with more valid evaluations. Therefore, more comprehensive quantitative comparisons could be carried out between different modalities, especially for different flow-diversion treatment scenarios and PM models with spatially-varying parameters. Results like the point-to point comparison on numerous planes, the discussion on the spatial shift of different velocity components and the velocity magnitude, etc. could be included. This would lead to a more comprehensive analysis of the PM model performance, as its parameters are variously specified according to different flow-diversion treatment modalities.

6) The establishment of PM model for a specified FD stent deployment would be an important work in the next step, as it would not only establish the methodology for creating a customised PM model, but also provide useful knowledge to build up the more advanced PM model with spatial-varying parameters, as mentioned in Sections 6.4.3 and 7.2 (4). In addition, the shape of the actual stent deployed in the blood vessel can also be captured and used for the PM modelling in CFD simulation. In an actual stent deployment, the shape of the stent after deployment is significantly affected by the morphological characteristics of the blood vessel, like the curvature, tortuosity, variations in diameter, etc., and this would lead to various flow-diversion effect of the stent, as a gap between the stent surface and the parent artery wall may lead to undesired leakage of blood flow into the aneurysm. Thus, research on this topic

would contribute to the establishment of a PM model that can mimic both the flow resistance created by the stent surface and the actual areas in the fluid field that is blocked by the stent.

Following the method presented in Chapter 6 to derive the PM parameters for FD stents, microCT scanning can be performed to capture the geometry of the actual FD stent deployed in a phantom, after which the reconstructed stent model can be used to numerically derive the PM parameters. A surface fitting method could be used to create the PM model surface that has the equivalent shape to the actual stent.

Another interesting topic is to establish the PM model for the coiling treatment (refer to Section 1.1.4.2 Figure 1-2) using the same method mentioned in the above paragraph. As both normal coiling and stent-supported coiling are commonly used in clinical treatment, the PM coil model could enable a more flexible and efficient CFD simulation for coiling treatment effect with consideration of the individual treatment modality, and thereby assist the surgical planning and treatment evaluation before and after a clinical operation."

Bibliography

[1] Seibert, B., Tummala, R.P., Chow, R., Faridar, A., Mousavi, S.A., and Divani, A.A. (2011) Intracranial aneurysms: review of current treatment options and outcomes. *Frontiers in Neurology*. 2.

[2] Sugiyama, S., Endo, H., Niizuma, K., Endo, T., Funamoto, K., Ohta, M., et al. (2016) Computational hemodynamic analysis for the diagnosis of atherosclerotic changes in intracranial aneurysms: a proof-of-concept study using 3 cases harboring atherosclerotic and nonatherosclerotic aneurysms simultaneously. *Computational and Mathematical Methods in Medicine*. 2016 1–12.

[3] Jeong, Y.-G., Jung, Y.-T., Kim, M.-S., Eun, C.-K., and Jang, S.-H. (2009) Size and location of ruptured intracranial aneurysms. *Journal of Korean Neurosurgical Society*. 45 (1), 11.

[4] Rahman, M., Smietana, J., Hauck, E., Hoh, B., Hopkins, N., Siddiqui, A., et al. (2010) Size ratio correlates with intracranial aneurysm rupture status: a prospective study. *Stroke*. 41 (5), 916–920.

[5] Pritz, M.B. (2011) Cerebral aneurysm classification based on angioarchitecture. *Journal of Stroke and Cerebrovascular Diseases*. 20 (2), 162–167.

[6] Meng, H., Wang, Z., Kim, M., Ecker, R.D., and Hopkins, L.N. (2006) Saccular aneurysms on straight and curved vessels are subject to different hemodynamics: implications of intravascular stenting. *American Journal of Neuroradiology*. 27 (9), 1861–1865.

[7] Farnoush, A., Avolio, A., and Qian, Y. (2013) Effect of bifurcation angle configuration and ratio of daughter diameters on hemodynamics of bifurcation aneurysms. *American Journal of Neuroradiology*. 34 (2), 391–396.

[8] Nakstad, P.Hj., Gjertsen, Ø., and Pedersen, H.Kr. (2008) Correlation of head trauma and traumatic aneurysms. *Interventional Neuroradiology*. 14 (1), 33–38.

[9] Kunwor, R. and Canelas, A. (2017) Rare case of cocaine-induced aortic aneurysm: a near dissection event. *Case Reports in Cardiology*. 2017 1–3.

[10] Martin-Schild, S., Albright, K.C., Hallevi, H., Barreto, A.D., Philip, M., Misra, V., et al. (2010) Intracerebral hemorrhage in cocaine users. *Stroke*. 41 (4), 680–684.

[11] Miley, J.T., Rodriguez, G.J., and Qureshi, A.I. (2008) Traumatic intracranial aneurysm formation following closed head injury. *Journal of Vascular and Interventional Neurology*. 1 (3), 79–82.

[12] Schmidt, M. (n.d.) Intracranial aneurysms. 52.

[13] Gonsoulin, M., Barnard, J.J., and Prahlow, J.A. (2002) Death resulting from ruptured cerebral artery aneurysm: 219 cases. *The American Journal of Forensic Medicine and Pathology*. 23 (1), 5–14.

[14] Pappu, S., Dardik, A., Tagare, H., and Gusberg, R.J. (2008) Beyond fusiform and saccular: a novel quantitative tortuosity index may help classify aneurysm shape and predict aneurysm rupture potential. *Annals of Vascular Surgery*. 22 (1), 88–97.

[15] Novitzke, J. and RN (2008) The basics of brain aneurysms: a guide for patients. 1 (3), 89–90.

[16] Vega, C., Kwoon, J.V., Lavine, S.D., and others (2002) Intracranial aneurysms: current evidence and clinical practice. *American Family Physician*. 66 (4), 601–610.

[17] Hacein-Bey, L. and Provenzale, J.M. (2011) Current imaging assessment and treatment of intracranial aneurysms. *American Journal of Roentgenology*. 196 (1), 32–44.

[18] Freeman, L.A., Young, P.M., Foley, T.A., Williamson, E.E., Bruce, C.J., and Greason, K.L. (2013) CT and MRI assessment of the aortic root and ascending aorta. *American Journal of Roentgenology*. 200 (6), W581–W592.

[19] England, A., Niker, A., and Redmond, C. (2010) Variability of vascular CT measurement techniques used in the assessment abdominal aortic aneurysms. *Radiography*. 16 (3), 173–181.

[20] Wiebers, D.O., Investigators, I.S. of U.I.A., and others (2003) Unruptured intracranial aneurysms: natural history, clinical outcome, and risks of surgical and endovascular treatment. *The Lancet*. 362 (9378), 103–110.

[21] Investigators, I.S. of U.I.A. and others (1998) Unruptured intracranial aneurysms—risk of rupture and risks of surgical intervention. *N Engl J Med*. 339 (24), 1725–1733.

[22] Meyers, P.M., Schumacher, H.C., Higashida, R.T., Derdeyn, C.P., Nesbit, G.M., Sacks, D., et al. (2009) Reporting standards for endovascular repair of saccular intracranial cerebral aneurysms. *Stroke*. 40 (5), e366–e379.

[23] Perrone, R.D., Malek, A.M., and Watnick, T. (2015) Vascular complications in autosomal dominant polycystic kidney disease. *Nature Reviews Nephrology*. 11 (10), 589–598.

[24] Molyneux, A.J., Birks, J., Clarke, A., Sneade, M., and Kerr, R.S. (2015) The durability of endovascular coiling versus neurosurgical clipping of ruptured cerebral aneurysms: 18 year follow-up of the UK cohort of the International Subarachnoid Aneurysm Trial (ISAT). *The Lancet*. 385 (9969), 691–697.

[25] Li, H., Pan, R., Wang, H., Rong, X., Yin, Z., Milgrom, D.P., et al. (2013) Clipping versus coiling for ruptured intracranial aneurysms a systematic review and meta-analysis. *Stroke*. 44 (1), 29–37.

[26] Pierot, L. and Wakhloo, A.K. (2013) Endovascular treatment of intracranial aneurysms: current status. *Stroke*. 44 (7), 2046–2054.

[27] Brilstra, E.H., Rinkel, G.J., van der Graaf, Y., van Rooij, W.J.J., and Algra, A. (1999) Treatment of intracranial aneurysms by embolization with coils. *Stroke*. 30 (2), 470–476.

[28] Molyneux, A.J., Kerr, R.S., Birks, J., Ramzi, N., Yarnold, J., Sneade, M., et al. (2009) Risk of recurrent subarachnoid haemorrhage, death, or dependence and standardised mortality ratios after clipping or coiling of an intracranial aneurysm in the International Subarachnoid Aneurysm Trial (ISAT): long-term follow-up. *The Lancet Neurology*. 8 (5), 427–433.

[29] Wong, G.K.C., Kwan, M.C.L., Ng, R.Y.T., Yu, S.C.H., and Poon, W.S. (2011) Flow diverters for treatment of intracranial aneurysms: Current status and ongoing clinical trials. *Journal of Clinical Neuroscience*. 18 (6), 737–740.

[30] Shapiro, M., Raz, E., Becske, T., and Nelson, P.K. (2014) Variable porosity of the pipeline embolization device in straight and curved vessels: a guide for optimal deployment strategy. *American Journal of Neuroradiology*. 35 (4), 727–733.

[31] Ding, Y.H., Tieu, T., and Kallmes, D.F. (2015) Experimental testing of a new generation of flow diverters in sidewall aneurysms in rabbits. *American Journal of Neuroradiology*. 36 (4), 732–736.

[32] Armoiry, X., Paysant, M., Hartmann, D., Aulagner, G., and Turjman, F. (2012) Interest of flow diversion prostheses in the management of unruptured intracranial aneurysms. *International Journal of Vascular Medicine*. 2012 1–5.

[33] Tse, M.M.Y., Yan, B., Dowling, R.J., and Mitchell, P.J. (2013) Current status of pipeline embolization device in the treatment of intracranial aneurysms: a review. *World Neurosurgery*. 80 (6), 829–835.

[34] Kulcsar, Z., Ernemann, U., Wetzel, S.G., Bock, A., Goericke, S., Panagiotopoulos, V., et al. (2010) High-profile flow diverter (silk) implantation in the basilar artery: efficacy in the treatment of aneurysms and the role of the perforators. *Stroke*. 41 (8), 1690–1696.

[35] Sankar, D.S. and Hemalatha, K. (2007) A non-Newtonian fluid flow model for blood flow through a catheterized artery—Steady flow. *Applied Mathematical Modelling*. 31 (9), 1847–1864.

[36] Kumar, D., Vinoth, R., Adhikari, R., and Shankar, V. (2017) Non-Newtonian and Newtonian blood flow in human aorta: A transient analysis. *Biomedical Research*. 28 (7),.

[37] Brust, M., Schaefer, C., Doerr, R., Pan, L., Garcia, M., Arratia, P.E., et al. (2013) Rheology of human blood plasma: viscoelastic versus newtonian behavior. *Physical Review Letters*. 110 (7),.

[38] Rand, P.W., Lacombe, E., Hunt, H.E., and Austin, W.H. (1964) Viscosity of normal human blood under normothermic and hypothermic conditions. *Journal of Applied Physiology*. 19 (1), 117–122.

[39] Moore, N.S. and Van Slyke, D.D. (1930) The relationships between plasma specific gravity, plasma protein content and edema in nephritis. *Journal of Clinical Investigation*. 8 (3), 337.

[40] Inci, S. and Spetzler, R.F. (2000) Intracranial aneurysms and arterial hypertension: a review and hypothesis. *Surgical Neurology*. 53 (6), 530–542.

[41] Evju, Ø. and Mardal, K.-A. (2015) On the assumption of laminar flow in physiological flows: cerebral aneurysms as an illustrative example. in: A. Quarteroni (Ed.), Modeling the Heart and the Circulatory System, Springer International Publishing, Champp. 177–195.

[42] Gabe, I.T., Gault, J.H., Ross, J., Mason, D.T., Mills, C.J., Schillingford, J.P., et al. (1969) Measurement of instantaneous blood flow velocity and pressure in conscious man with a catheter-tip velocity probe. *Circulation*. 40 (5), 603–614.

[43] Day, M.A. (1990) The no-slip condition of fluid dynamics. *Erkenntnis*. 33 (3), 285–296.

[44] Papaioannou, T.G. and Stefanadis, C. (2005) Vascular wall shear stress: basic principles and methods. *Hellenic J Cardiol*. 46 (1), 9–15.

[45] Singh, P.K., Marzo, A., Howard, B., Rufenacht, D.A., Bijlenga, P., Frangi, A.F., et al. (2010) Effects of smoking and hypertension on wall shear stress and oscillatory shear index at the site of intracranial aneurysm formation. *Clinical Neurology and Neurosurgery*. 112 (4), 306–313.

[46] Sen, Y., Qian, Y., Avolio, A., and Morgan, M. (2014) Image segmentation methods for intracranial aneurysm haemodynamic research. *Journal of Biomechanics*. 47 (5), 1014–1019.

[47] Yu, Y., Xu, J., Fang, Y., Wu, X., Yang, P., Jiang, C., et al. (2013) Analysis of morphologic and hemodynamic parameters for unruptured posterior communicating artery aneurysms with oculomotor nerve palsy. *American Journal of Neuroradiology*. 34 (11), 2187–2191.

[48] Jou, L. and Britz, Dr.G. (2016) Correlation between aneurysm size and hemodynamics in one individual with multiple small intracranial aneurysms. *Cureus*.

[49] Farnoush, A., Qian, Y., Takao, H., Murayama, Y., and Avolio, A. (2012) Effect of saccular aneurysm and parent artery morphology on hemodynamics of cerebral bifurcation aneurysms. in: 2012 Annual International Conference of the IEEE Engineering in Medicine and Biology Society, IEEE, pp. 6677–6680.

[50] Farnoush, A., Avolio, A., and Qian, Y. (2014) A growth model of saccular aneurysms based on hemodynamic and morphologic discriminant parameters for risk of rupture. *Journal of Clinical Neuroscience*. 21 (9), 1514–1519.

[51] Shimogonya, Y., Ishikawa, T., Imai, Y., Matsuki, N., and Yamaguchi, T. (2009) Can temporal fluctuation in spatial wall shear stress gradient initiate a cerebral aneurysm? A proposed novel hemodynamic index, the gradient oscillatory number (GON). *Journal of Biomechanics*. 42 (4), 550–554.

[52] Qian, Y. and Umezu, M. (2013) Hemodynamic features of cerebral aneurysms that influence to rupture. *Japanese Society for Medical and Biological Engineering*. 51 (Supplement), M–46.

[53] Takao, H., Murayama, Y., Otsuka, S., Qian, Y., Mohamed, A., Masuda, S., et al. (2012) Hemodynamic differences between unruptured and ruptured intracranial aneurysms during observation. *Stroke*. 43 (5), 1436–1439.

[54] Francis, S.E., Tu, J., Qian, Y., and Avolio, A.P. (2013) A combination of genetic, molecular and haemodynamic risk factors contributes to the formation, enlargement and rupture of brain aneurysms. *Journal of Clinical Neuroscience*. 20 (7), 912–918.

[55] Cebral, J., Ollikainen, E., Chung, B.J., Mut, F., Sippola, V., Jahromi, B.R., et al. (2017) Flow conditions in the intracranial aneurysm lumen are associated with inflammation and degenerative changes of the aneurysm wall. *American Journal of Neuroradiology*. 38 (1), 119–126.

[56] Penn, D.L., Komotar, R.J., and Sander Connolly, E. (2011) Hemodynamic mechanisms underlying cerebral aneurysm pathogenesis. *Journal of Clinical Neuroscience*. 18 (11), 1435–1438.

[57] Dhar, S., Tremmel, M., Mocco, J., Kim, M., Yamamoto, J., Siddiqui, A.H., et al. (2008) Morphology parameters for intracranial aneurysm rupture risk assessment. *Neurosurgery*. 63 (2), 185–197.

[58] Chong, W., Zhang, Y., Qian, Y., Lai, L., Parker, G., and Mitchell, K. (2014) Computational hemodynamics analysis of intracranial aneurysms treated with flow diverters: correlation with clinical outcomes. *American Journal of Neuroradiology*. 35 (1), 136–142.

[59] Long, Y., Zhong, J., Yu, H., Yan, H., Zhuo, Z., Meng, Q., et al. (2015) A scaling aneurysm model-based approach to assessing the role of flow pattern and energy loss in aneurysm rupture prediction. *Journal of Translational Medicine*. 13 (1),.

[60] Zhou, G., Zhu, Y., Yin, Y., Su, M., and Li, M. (2017) Association of wall shear stress with intracranial aneurysm rupture: systematic review and meta-analysis. *Scientific Reports*. 7 (1),.

[61] Shojima, M. (2004) Magnitude and role of wall shear stress on cerebral aneurysm: computational fluid dynamic study of 20 middle cerebral artery aneurysms. *Stroke*.

[62] Meng, H., Tutino, V.M., Xiang, J., and Siddiqui, A. (2014) High WSS or low WSS? Complex interactions of hemodynamics with intracranial aneurysm initiation, growth, and rupture: toward a unifying hypothesis. *American Journal of Neuroradiology*. 35 (7), 1254–1262.

[63] Mut, F., Raschi, M., Scrivano, E., Bleise, C., Chudyk, J., Ceratto, R., et al. (2015) Association between hemodynamic conditions and occlusion times after flow diversion in cerebral aneurysms. *Journal of NeuroInterventional Surgery*. 7 (4), 286–290.

[64] Pritz, M.B. (2012) Geometry of saccular, side-branch cerebral aneurysms: implications for treatment. *Journal of Stroke and Cerebrovascular Diseases*. 21 (5), 391–394.

[65] Qiu, T., Jin, G., Xing, H., and Lu, H. (2017) Association between hemodynamics, morphology, and rupture risk of intracranial aneurysms: a computational fluid modeling study. *Neurological Sciences*. 38 (6), 1009–1018.

[66] Zeng, Z., Durka, M.J., Kallmes, D.F., Ding, Y., and Robertson, A.M. (2011) Can aspect ratio be used to categorize intra-aneurysmal hemodynamics?—A study of elastase induced aneurysms in rabbit. *Journal of Biomechanics*. 44 (16), 2809–2816.

[67] Chung, J., Lachapelle, K., Wener, E., Cartier, R., De Varennes, B., Fraser, R., et al. (2014) Energy loss, a novel biomechanical parameter, correlates with aortic aneurysm size and histopathologic findings. *The Journal of Thoracic and Cardiovascular Surgery*. 148 (3), 1082–1089.

[68] Hu, P., Qian, Y., Lee, C.-J., Zhang, H.-Q., and Ling, F. (2015) The energy loss may predict rupture risks of anterior communicating aneurysms: a preliminary result. *International Journal of Clinical and Experimental Medicine*. 8 (3), 4128.

[69] Larrabide, I., Geers, A.J., Morales, H.G., Aguilar, M.L., and Rüfenacht, D.A. (2015) Effect of aneurysm and ICA morphology on hemodynamics before and after flow diverter treatment. *Journal of NeuroInterventional Surgery*. 7 (4), 272–280.

[70] Imai, Y., Sato, K., Ishikawa, T., and Yamaguchi, T. (2008) Inflow into saccular cerebral aneurysms at arterial bends. *Annals of Biomedical Engineering*. 36 (9), 1489–1495.

[71] Raschi, M., Mut, F., Byrne, G., Putman, C.M., Tateshima, S., Viñuela, F., et al. (2012) CFD and PIV analysis of hemodynamics in a growing intracranial aneurysm. *International Journal for Numerical Methods in Biomedical Engineering*. 28 (2), 214–228.

[72] Van Ooij, P., Guédon, A., Poelma, C., Schneiders, J., Rutten, M.C.M., Marquering, H.A., et al. (2012) Complex flow patterns in a real-size intracranial aneurysm phantom: phase contrast MRI compared with particle image velocimetry and computational fluid dynamics. *NMR in Biomedicine*. 25 (1), 14–26.

[73] Isoda, H., Ohkura, Y., Kosugi, T., Hirano, M., Alley, M.T., Bammer, R., et al. (2010) Comparison of hemodynamics of intracranial aneurysms between MR fluid dynamics using 3D cine phase-contrast MRI and MR-based computational fluid dynamics. *Neuroradiology*. 52 (10), 913–920.

[74] Khodarahmi, I., Shakeri, M., Kotys-Traughber, M., Fischer, S., Sharp, M.K., and Amini, A.A. (2014) In vitro validation of flow measurement with phase contrast MRI at 3 tesla using stereoscopic particle image velocimetry and stereoscopic particle image velocimetry-based computational fluid dynamics: stenotic flow using PC-MRI, SPIV, and CFD. *Journal of Magnetic Resonance Imaging*. 39 (6), 1477–1485.

[75] Roloff, C., Stucht, D., Beuing, O., and Berg, P. (2018) Comparison of intracranial aneurysm flow quantification techniques: standard PIV vs stereoscopic PIV vs tomographic PIV vs phase-contrast MRI vs CFD. *Journal of NeuroInterventional Surgery*. neurintsurg-2018-013921.

[76] Ford, M.D., Nikolov, H.N., Milner, J.S., Lownie, S.P., DeMont, E.M., Kalata, W., et al. (2008) PIV-measured versus CFD-predicted flow dynamics in anatomically realistic cerebral aneurysm models. *Journal of Biomechanical Engineering*. 130 (2), 021015.

[77] Khodarahmi, I. (2015) Comparing velocity and fluid shear stress in a stenotic phantom with steady flow: phase-contrast MRI, particle image velocimetry and computational fluid dynamics. *Magnetic Resonance Materials in Physics, Biology and Medicine*. 28 (4), 385–393.

[78] Bouillot, P., Brina, O., Ouared, R., Yilmaz, H., Lovblad, K.-O., Farhat, M., et al. (2015) Computational fluid dynamics with stents: quantitative comparison with particle image velocimetry for three commercial off the shelf intracranial stents. *Journal of NeuroInterventional Surgery*.

[79] Augsburger, L., Reymond, P., Rufenacht, D.A., and Stergiopulos, N. (2011) Intracranial stents being modeled as a porous medium: flow simulation in stented cerebral aneurysms. *Annals of Biomedical Engineering*. 39 (2), 850–863.

[80] Ohta, M., Anzai, H., Miura, Y., and Nakayama, T. (2015) Parametric study of porous media as substitutes for flow-diverter stent. *Biomaterials and Biomedical Engineering*. 2 (2), 111–125.

[81] Morales, H.G. and Bonnefous, O. (2014) Modeling hemodynamics after flow diverter with a porous medium. in: 2014 IEEE 11th International Symposium on Biomedical Imaging (ISBI), IEEE, pp. 1324–1327.

[82] Suzuki, T., Kadokura, S., Takao, H., Tateshima, S., Masuda, S., Chihebeddine, D., et al. (2014) Verification of porous loss model for assessment of flow diverters.

[83] Zhang, Y., Chong, W., and Qian, Y. (2013) Investigation of intracranial aneurysm hemodynamics following flow diverter stent treatment. *Medical Engineering & Physics*. 35 (5), 608–615.

[84] Jungreuthmayer, C., Steppert, P., Sekot, G., Zankel, A., Reingruber, H., Zanghellini, J., et al. (2015) The 3D pore structure and fluid dynamics simulation of macroporous monoliths: High permeability due to alternating channel width. *Journal of Chromatography A*. 1425 141–149.

[85] Dazeo, N., Dottori, J., Boroni, G., and Larrabide, I. (2018) A comparative study of porous medium CFD models for flow diverter stents: Advantages and shortcomings. *International Journal for Numerical Methods in Biomedical Engineering*. e3145.

[86] Warmbrunn, S. (n.d.) Inspecting endovascular aneurysm treatments with porous medium flow simulations and the use of a statistical framework. 73.

[87] Tsuji M., Ishida F., Furukawa K., Miura Y., Sano T., Shiba M., et al. (2017) Hemodynamic changes after placing intracranial stents : computational fluid dynamics (CFD) analysis using porous media modeling in the stent domain. *Japanese Journal of Neurosurgery*. 26 (6), 444–451.

[88] Wang, S., Ding, G., Zhang, Y., and Yang, X. (2011) Computational haemodynamics in two idealised cerebral wide-necked aneurysms after stent placement. *Computer Methods in Biomechanics and Biomedical Engineering*. 14 (11), 927–937.

[89] Li, Y., Anzai, H., Nakayama, T., Shimizu, Y., Miura, Y., and Qiao, A. (2014) Simulation of hemodynamics in artery with aneurysm and stenosis with different geometric configuration. *Journal of Biomechanical Science and Engineering*. 9 (1), JBSE0003–JBSE0003.

[90] Kim, M., Taulbee, D.B., Tremmel, M., and Meng, H. (2008) Comparison of two stents in modifying cerebral aneurysm hemodynamics. *Annals of Biomedical Engineering*. 36 (5), 726–741.

[91] Beier, S., Ormiston, J., Webster, M., Cater, J., Norris, S., Medrano-Gracia, P., et al. (2016) Hemodynamics in idealized stented coronary arteries: important stent design considerations. *Annals of Biomedical Engineering*. 44 (2), 315–329.

[92] l gorzata Peszynska, M., Trykozko, A., and Sobieski, W. (n.d.) Forchheimer law in computational and experimental studies of flow through porous media at porescale and mesoscale.

[93] Nield, D.A. and Bejan, A. (2006) Convection in porous media. 3rd Ed Springer, New York.

[94] Jambhekar, V.A. (2011) Forchheimer porous-media flow models-numerical investigation and comparison with experimental data. *Published Master Thesis. Stuttgart: Universität Stuttgart-Institut Für Wasserund Umweltsystemmodellierung*.

[95] Grillo, A., Carfagnay, M., and Federicoz, S. (2014) The Darcy-Forchheimer law for modelling fluid flow in biological tissues. *Theoretical and Applied Mechanics*. 41 (4), 283–322.

[96] Amao, A.M. (2007) Mathematical model for Darcy Forchheimer flow with applications to well performance analysis, 2007.

[97] Cakmak, A. (2009) Analysis of nonlinear Darcy-Forchheimer flows in porous media, Texas Tech University, 2009.

[98] Tosco, T., Marchisio, D.L., Lince, F., and Sethi, R. (2013) Extension of the Darcy–Forchheimer law for shear-thinning fluids and validation via pore-scale flow simulations. *Transport in Porous Media*. 96 (1), 1–20.

[99] Teng, H. and Zhao, T.S. (2000) An extension of Darcy's law to non-Stokes flow in porous media. *Chemical Engineering Science*. 55 (14), 2727–2735.

[100] Xiang, J., Ma, D., Snyder, K.V., Levy, E.I., Siddiqui, A.H., and Meng, H. (2014) Increasing flow diversion for cerebral aneurysm treatment using a single flow diverter. *Neurosurgery*. 75 (3), 286–294.

[101] Zhang, M., Li, Y., Zhao, X., Verrelli, D.I., Chong, W., Ohta, M., et al. (2017) Haemodynamic effects of stent diameter and compaction ratio on flow-diversion treatment of intracranial aneurysms: A numerical study of a successful and an unsuccessful case. *Journal of Biomechanics*. 14 (58), 179–186.

[102] Ma, D., Xiang, J., Choi, H., Dumont, T.M., Natarajan, S.K., Siddiqui, A.H., et al. (2014) Enhanced aneurysmal flow diversion using a dynamic push-pull technique: an experimental and modeling study. *American Journal of Neuroradiology*. 35 (9), 1779–1785.

[103] Janiga, G., Daróczy, L., Berg, P., Thévenin, D., Skalej, M., and Beuing, O. (2015) An automatic CFD-based flow diverter optimization principle for patient-specific intracranial aneurysms. *Journal of Biomechanics*. 48 (14), 3846–3852.

[104] Janiga, G., Rössl, C., Skalej, M., and Thévenin, D. (2013) Realistic virtual intracranial stenting and computational fluid dynamics for treatment analysis. *Journal of Biomechanics*. 46 (1), 7–12.

[105] Sforza, D.M., Putman, C.M., and Cebral, J.R. (2012) Computational fluid dynamics in brain aneurysms. *International Journal for Numerical Methods in Biomedical Engineering*. 28 (6–7), 801–808.

[106] Wong, G.K.C. and Poon, W.S. (2011) Current status of computational fluid dynamics for cerebral aneurysms: The clinician's perspective. *Journal of Clinical Neuroscience*. 18 (10), 1285–1288.

[107] Surana, K.S., Allu, S., Tenpas, P.W., and Reddy, J.N. (2007) K-version of finite element method in gas dynamics: higher-order global differentiability numerical solutions. *International Journal for Numerical Methods in Engineering*. 69 (6), 1109–1157.

[108] Westerweel, J., Elsinga, G.E., and Adrian, R.J. (2013) Particle image velocimetry for complex and turbulent flows. *Annual Review of Fluid Mechanics*. 45 (1), 409–436.

[109] Melling, A. (1997) Tracer particles and seeding for particle image velocimetry. *Measurement Science and Technology*. 8 (12), 1406–1416.

[110] Lotz, J., Meier, C., Leppert, A., and Galanski, M. (2002) Cardiovascular flow measurement with phase-contrast MR imaging: basic facts and implementation. *Radiographics*. 22 (3), 651–671.

[111] Stankovic, Z., Allen, B.D., Garcia, J., Jarvis, K.B., and Markl, M. (2014) 4D flow imaging with MRI. *Cardiovascular Diagnosis and Therapy*. 4 (2), 173.

[112] Ohta, M., Hirabayashi, M., Wetzel, S., Lylyk, P., Wata, H., Tsutsumi, S., et al. (2004) Impact of stent design on intra-aneurysmal flow: a computer simulation study. *Interventional Neuroradiology*. 10 (2_suppl), 85–94.

[113] Gay, M. and Zhang, L.T. (2009) Numerical studies of blood flow in healthy, stenosed, and stented carotid arteries. *International Journal for Numerical Methods in Fluids*. 61 (4), 453–472.

[114] Castro, M.A. (2013) Understanding the role of hemodynamics in the initiation, progression, rupture, and treatment outcome of cerebral aneurysm from medical image-based computational studies. *ISRN Radiology*. 2013 1–17.

[115] Jeong, W. and Rhee, K. (2012) Hemodynamics of cerebral aneurysms: computational analyses of aneurysm progress and treatment. *Computational and Mathematical Methods in Medicine*. 2012 1–11.

[116] Riccardello, G.J., Changa, A.R., Al-Mufti, F., Singh, I.P., Gandhi, C., Roman, M., et al. (2018) Hemodynamic impingement and the initiation of intracranial side-wall aneurysms. *Interventional Neuroradiology*. 24 (3), 288–296.

[117] Hammad, K.J., Ötügen, M.V., and Arik, E.B. (1999) A PIV study of the laminar axisymmetric sudden expansion flow. *Experiments in Fluids*. 26 (3), 266–272.

[118] Mokhtar, N.H., Abas, A., Teong, S.L., and Razak, N.A. (2016) Particle image velocimetry experiment of blood flow through stent in artery bifurcation aneurysm problem. in: Songkhla, Thailandp. 030095.

[119] Bouillot, P., Brina, O., Ouared, R., Lovblad, K.-O., Farhat, M., and Pereira, V.M. (2014) Particle imaging velocimetry evaluation of intracranial stents in sidewall aneurysm: hemodynamic transition related to the stent design. *PLoS ONE*. 9 (12), e113762.

[120] Polanczyk, A., Podgorski, M., Wozniak, T., Stefanczyk, L., and Strzelecki, M. (2018) Computational fluid dynamics as an engineering tool for the reconstruction of hemodynamics after carotid artery stenosis operation: a case study. *Medicina*. 54 (3), 42.

[121] Traber, J., Wurche, L., Dieringer, M.A., Utz, W., von Knobelsdorff-Brenkenhoff, F., Greiser, A., et al. (2016) Real-time phase contrast magnetic resonance imaging for assessment of haemodynamics: from phantom to patients. *European Radiology*. 26 (4), 986–996.

[122] Ha, H., Kim, G.B., Kweon, J., Lee, S.J., Kim, Y.-H., Lee, D.H., et al. (2016) Hemodynamic measurement using four-dimensional phase-contrast MRI: quantification of hemodynamic parameters and clinical applications. *Korean Journal of Radiology*. 17 (4), 445.

[123] Shimizu, Y., Javadzadegan, A., Hayase, T., and Ohta, M. (2013) Flow observations in elastic stenosis biomodel with comparison to rigid-like model. *Technology and Healthcare*. 21 (4), 305–314.

[124] Qian, Y., Takao, H., Umezu, M., and Murayama, Y. (2011) Risk analysis of unruptured aneurysms using computational fluid dynamics technology: preliminary results. *American Journal of Neuroradiology*. 32 (10), 1948–1955.

[125] Geers, A.J., Larrabide, I., Radaelli, A.G., Bogunovic, H., Kim, M., Gratama van Andel, H.A.F., et al. (2011) Patient-specific computational hemodynamics of intracranial aneurysms from 3D rotational angiography and CT angiography: an in vivo reproducibility study. *American Journal of Neuroradiology*. 32 (3), 581–586.

[126] Goubergrits, L., Schaller, J., Kertzscher, U., Petz, C., Hege, H.-C., and Spuler, A. (2013) Reproducibility of image-based analysis of cerebral aneurysm geometry and hemodynamics: an in-vitro study of magnetic resonance imaging, computed tomography, and three-dimensional rotational angiography. *Journal of Neurological Surgery Part A: Central European Neurosurgery*. 74 (05), 294–302.

[127] Nakamura, M., Wada, S., Yokosawa, S., Isoda, H., Takeda, H., and Yamaguchi, T. (2007) Measurement of blood flow in the left ventricle and aorta using clinical 2D cine phase-contrast magnetic resonance imaging. *Journal of Biomechanical Science and Engineering*. 2 (2), 46–57.

[128] Köhler, B., Born, S., van Pelt, R.F.P., Hennemuth, A., Preim, U., and Preim, B. (2017) A survey of cardiac 4D PC-MRI data processing: 4D PC-MRI data processing survey. *Computer Graphics Forum*. 36 (6), 5–35.

[129] Suzuki, T., Takao, H., Suzuki, T., Suzuki, T., Masuda, S., Dahmani, C., et al. (2017) Variability of hemodynamic parameters using the common viscosity assumption in a computational fluid dynamics analysis of intracranial aneurysms. *Technology and Health Care*. 25 (1), 37–47.

[130] Büsen, M., Arenz, C., Neidlin, M., Liao, S., Schmitz-Rode, T., Steinseifer, U., et al. (2017) Development of an in vitro PIV setup for preliminary investigation of the effects of aortic compliance on flow patterns and hemodynamics. *Cardiovascular Engineering and Technology*. 8 (3), 368–377.

[131] Persoons, T. and O'Donovan, T.S. (2010) High dynamic velocity range particle image velocimetry using multiple pulse separation imaging. *Sensors*. 11 (1), 1–18.

[132] Bouillot, P., Brina, O., Ouared, R., Lovblad, K.O., Pereira, V.M., and Farhat, M. (2014) Multi-time-lag PIV analysis of steady and pulsatile flows in a sidewall aneurysm. *Experiments in Fluids*. 55 (6), 1746.

[133] Back, L.D., Radbill, J.R., and Crawford, D.W. (1977) Analysis of pulsatile, viscous blood flow through diseased coronary arteries of man. *Journal of Biomechanics*. 10 (5–6), 339–353.

[134] Geers, A.J., Larrabide, I., Morales, H.G., and Frangi, A.F. (2014) Approximating hemodynamics of cerebral aneurysms with steady flow simulations. *Journal of Biomechanics*. 47 (1), 178–185.

[135] Yousif, M.Y., Holdsworth, D.W., and Poepping, T.L. (2011) A blood-mimicking fluid for particle image velocimetry with silicone vascular models. *Experiments in Fluids*. 50 (3), 769–774.

[136] Yousif, M.Y., Holdsworth, D.W., and Poepping, T.L. (2009) Deriving a blood-mimicking fluid for particle image velocimetry in sylgard-184 vascular models. in: Engineering in Medicine and Biology Society, 2009. EMBC 2009. Annual International Conference of the IEEE, IEEE, pp. 1412–1415.

[137] Li, Y., Zhang, M., Verrelli, D.I., Yang, W., Chong, W., Ohta, M., et al. (2017) Sensitivity study on modelling a flow-diverting stent as a porous medium using computational fluid dynamics. in: Engineering in Medicine and Biology Society (EMBC), 2017 39th Annual International Conference of the IEEE, IEEE, pp. 3389–3392.

[138] Li, Y., Zhang, M., Verrelli, D.I., Chong, W., Ohta, M., and Qian, Y. (2018) Numerical simulation of aneurysmal haemodynamics with calibrated porous-medium models of flow-diverting stents. *Journal of Biomechanics*. 80 88–94.

[139] Theunissen, R., Scarano, F., and Riethmuller, M.L. (2008) On improvement of PIV image interrogation near stationary interfaces. *Experiments in Fluids*. 45 (4), 557–572.

[140] Yagi, T., Sato, A., Shinke, M., Takahashi, S., Tobe, Y., Takao, H., et al. (2013) Experimental insights into flow impingement in cerebral aneurysm by stereoscopic particle image velocimetry: transition from a laminar regime. *Journal of The Royal Society Interface*. 10 (82), 20121031.

[141] Zhang, M., Li, Y., Zhao, X., Verrelli, D.I., Chong, W., Ohta, M., et al. (2017) Haemodynamic effects of stent diameter and compaction ratio on flow-diversion treatment of intracranial aneurysms: A numerical study of a successful and an unsuccessful case. *Journal of Biomechanics*.

[142] Sfyroeras, G.S., Dalainas, I., Giannakopoulos, T.G., Antonopoulos, K., Kakisis, J.D., and Liapis, C.D. (2012) Flow-diverting stents for the treatment of arterial aneurysms. *Journal of Vascular Surgery*. 56 (3), 839–846.

[143] Aurboonyawat, T., Blanc, R., Schmidt, P., Piotin, M., Spelle, L., Nakib, A., et al. (2011) An in vitro study of Silk stent morphology. *Neuroradiology*. 53 (9), 659–667.

[144] Makoyeva, A., Bing, F., Darsaut, T.E., Salazkin, I., and Raymond, J. (2013) The varying porosity of braided self-expanding stents and flow diverters: an experimental study. *American Journal of Neuroradiology*. 34 (3), 596–602.

[145] Mohlenbruch, M.A., Herweh, C., Jestaedt, L., Stampfl, S., Schonenberger, S., Ringleb, P.A., et al. (2015) The FRED flow-diverter stent for intracranial aneurysms: clinical study to assess safety and efficacy. *American Journal of Neuroradiology*. 36 (6), 1155–1161.

[146] Soares, J.S., Gao, C., Alemu, Y., Slepian, M., and Bluestein, D. (2013) Simulation of platelets suspension flowing through a stenosis model using a dissipative particle dynamics approach. *Annals of Biomedical Engineering*. 41 (11), 2318–2333.

[147] Qiao, A., Han, H.-C., Ohta, M., and Qian, Y. (2014) Computational simulations in the cardiovascular system. *The Scientific World Journal*. 2014 1–1.

[148] Li, M.X., Beech-Brandt, J.J., John, L.R., Hoskins, P.R., and Easson, W.J. (2007) Numerical analysis of pulsatile blood flow and vessel wall mechanics in different degrees of stenoses. *Journal of Biomechanics*. 40 (16), 3715–3724.

[149] Cebral, J.R., Mut, F., Raschi, M., Scrivano, E., Ceratto, R., Lylyk, P., et al. (2010) Aneurysm rupture following treatment with flow-diverting stents: computational hemodynamics analysis of treatment. *American Journal of Neuroradiology*.

[150] Castro, M.A., Putman, C.M., and Cebral, J.R. (2006) Computational fluid dynamics modeling of intracranial aneurysms: effects of parent artery segmentation on intra-aneurysmal hemodynamics. *American Journal of Neuroradiology*. 27 (8), 1703–1709.

[151] Steinman, D.A., Milner, J.S., Norley, C.J., Lownie, S.P., and Holdsworth, D.W. (2003) Image-based computational simulation of flow dynamics in a giant intracranial aneurysm. *American Journal of Neuroradiology*. 24 (4), 559–566.

[152] Torii, R., Oshima, M., Kobayashi, T., Takagi, K., and Tezduyar, T.E. (2007) Influence of wall elasticity in patient-specific hemodynamic simulations. *Computers & Fluids*. 36 (1), 160–168.

Appendix I

An Example of CFD Simulation with Idealised Aneurysm Geometries

Introduction

Background

Currently, stroke is one of the most dangerous disease threatening patient's health and life, which is significantly associated with IA and artery stenosis [83]. Stenosis may create disturbance and flow separation, and consequently induce significant flow resistance, large pressure drop, complicated flow pattern, disturbed WSS, and wall motion patterns [84]–[86]. The use of CFD in the study involving aneurysm and stenosis achieve significant findings [87], focusing on various shape and size of aneurysms in complex configuration of parent arteries, stenosis severity with idealised models and patient-specific models.

Current issue

Haemodynamics is thought to be an important factor in the pathogenesis and treatment of intracranial aneurysms and stenosis [46], [91]. However, the haemodynamic characteristics of the complicated arterial disease accompanied by both stenosis and aneurysm have not been clearly investigated.

Purpose

The purpose of this study is to investigate the impact of complex morphologies on aneurysmal haemodynamics, by simulating 7 idealised straight-vessel models (refer to Section 2.4 for more details about the study with straight vessel model) and 14 idealised curved-vessel models. Specific attentions are paid to different severity of stenosis, various distance between stenosis and aneurysm, and highly-curved parent arteries in different curvatures.

Materials and Methods

Geometry of stenosis and aneurysm

This study pays attention to blood vessels with both stenosis and aneurysm, considering of the variation of the size and shape of the geometrical configurations. Idealised models were created using 3D CAD software (Pro/ENGINEER Wildfire 4.0, PTC, USA). Two groups of typical geometries were established: stenosis and aneurysm located in straight vessels (refer to Section 2.4 for more details about the study with straight vessel model), and stenosis and aneurysms located in curved vessel.

Morphological parameters of curved vessels with stenosis and aneurysm are as below: The size of the semicircular curved vessel is different depends on its curvature. The aneurysm locates at the apex of the convex side of the semicircular curve, with an aneurysm in the maximal diameter of 8 mm. Two straight tubes (30 mm in length) have been created at the opening respectively at the inlet and outlet of the semicircular curved parent artery (see Figure AI-1). The diameter of the parent artery is 4 mm. An outer cut at the vessel is created, which is regarded as the stenosis, at the upstream of the aneurysm. The position of the outer cut varies with respect to different distance between stenosis and aneurysm, and the diameter of the narrowed section is determined by the stenosis ratio (defined as equation 2-7). The Dean number, calculated with $\{Re^*(D^*C/4)^{1/2}\}$, where D is the diameter of the parent artery and C is

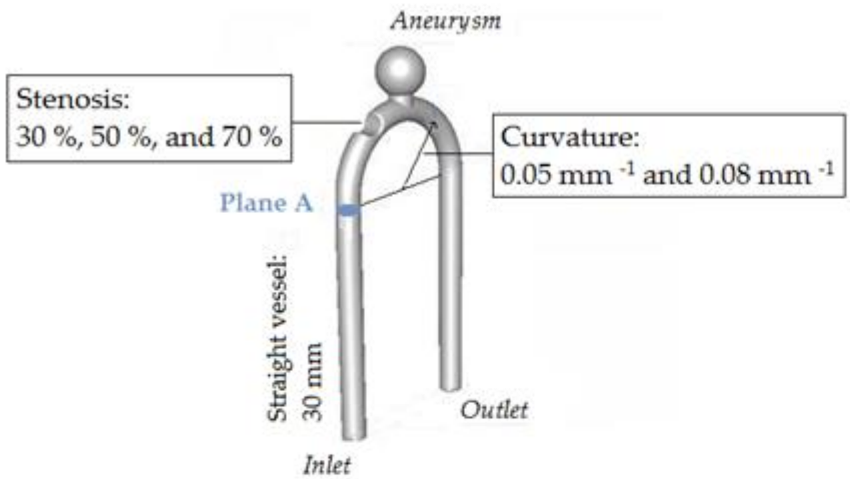

Figure AI-1 Sketch of geometry with stenosis and aneurysm in a curved vessel the curvature of the parent artery, ranges between 53 and 67 for the curved-vessel models studied in this research, since the diameter is 4 mm and the nominated Re is 240 [6]. Hence, the curvatures and model settings in this research are considered to be matched with the real environment in human body, as the typical Dean number ranges from 10 to 200 in human intracranial arteries [146].

A variety of degrees of stenosis were studied to represent for mild stenosis (30%), moderate stenosis (50%) and severe stenosis (70%) in patient cases [113] [147].

Meshing

Considering that mesh generation is a crucial procedure determining the simulation accuracy, the meshes across all the models were performed under a standard protocol. The entire fluid zone was discretised into tetrahedral elements with 3 boundary layers. The maximal element size was defined as the smallest vessel diameter divided by 10, in order to ensure that the fluid zone to be discretised into at least 10 elements even for the narrowest cross-section. The entire fluid domain was discretised into about 1 million to 2 million elements across different cases. A mesh dependency test was performed to assure the stability of simulation result with such mesh generation.

Fluid Simulation

Assumptions of Newtonian, incompressible fluid and laminar flow were determined for the fluid, with the density specified as 1050 kg/m3 and the viscosity specified as 0.0035 Pa·s.

A steady condition was applied for all simulations. Velocity of 0.2 m/s was specified at the model inlet with a Re of 240, within the range of Re in intracranial arteries (from 110 to 850). By this setting, the simulation was in good consistency with the assumption of laminar flow in every grids within the fluid zone. Pressure boundary condition of 0 Pa was defined at the outlet. Stationary and no-slip condition was set on the model wall.

The calculation was performed using a commercial solver (Ansys Fluent 14 Inc., USA) based on FVM.

Results

Curved vessel with aneurysm and stenosis

Flow pattern

According to fluid mechanics, a principle of flow mechanisms in straight vessel and curved vessel is different. In the sidewall aneurysm model, flow in the parent vessel is tangential to the aneurysm orifice and the stream in the blood artery is viscous shear-driven flow. In curved-vessel models, the aneurysm sac is located at the convex side of the parent artery, along the inertial path of the flow. The stream in the artery is inertia-driven flow [6].

The inertia-driven flow created different results from straight blood vessels of flow pattern along the artery, as shown in Figure AI-2. It illustrates the comparison of flow pattern between 4 models with a same aneurysm existing after a moderate distance from the stenosis. The different behaviours of flow were affected by different

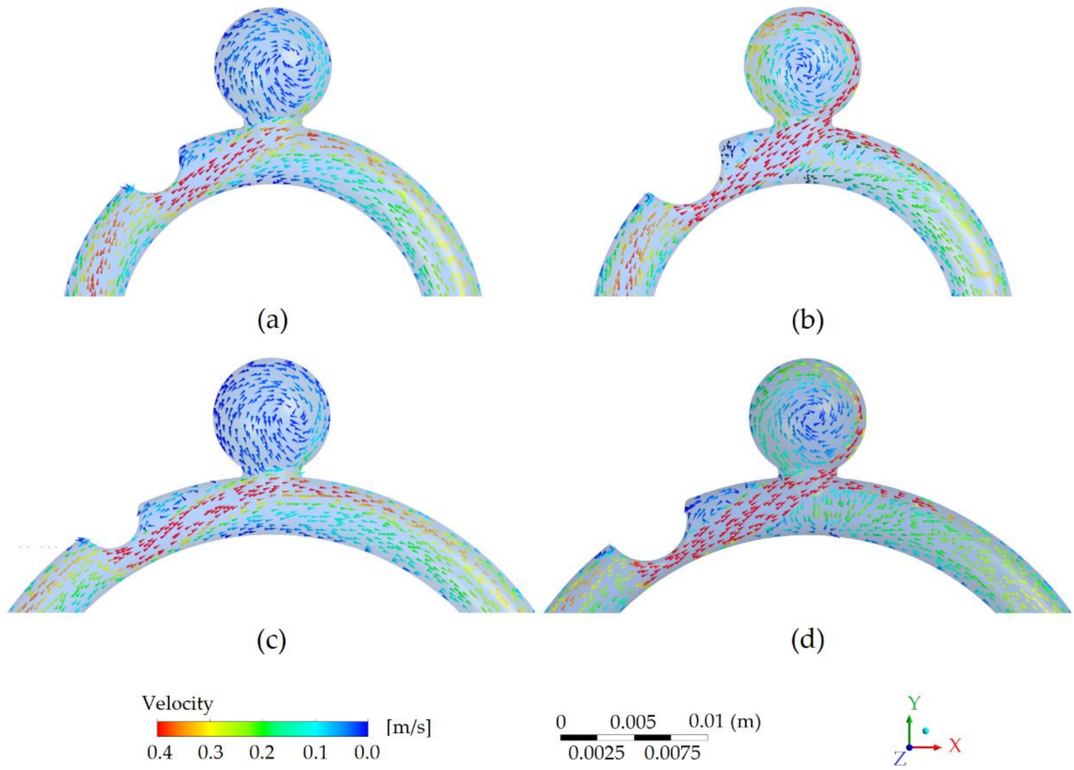

Figure AI-2 Aneurysmal flow pattern and reattachment length in different models: (a) C = 0.05 mm-1, 50 % (b) C = 0.05 mm-1, 70 % (c) C = 0.08 mm-1, 50 % (d) C = 0.08 mm-1, 70 % (curvature of parent artery, degree of stenosis)

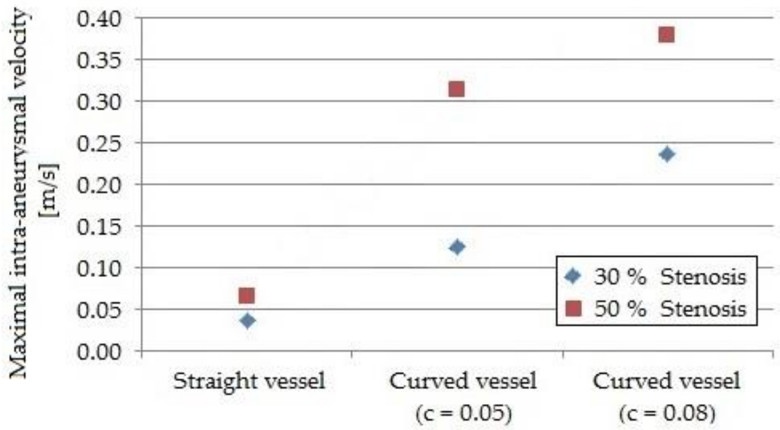

Figure AI-4 Maximal intra-aneurysmal velocity for models with different levels of stenosis and parent artery curvatures

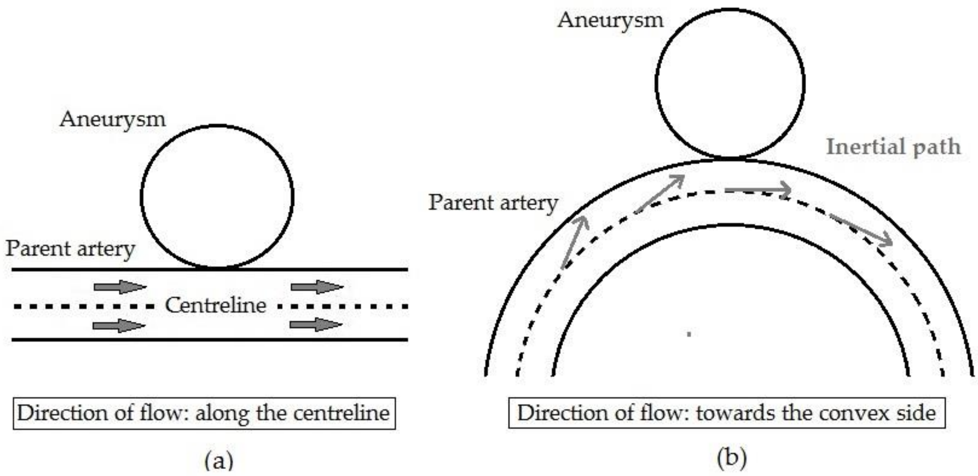

Figure AI-3 Sketch of the reattachment length affected by curvature of parent artery: (a) straight vessel (b) C = 0.05 mm $^{-1}$ (c) C = 0.08 mm $^{-1}$

curvatures of parent arteries and different degrees of stenosis. The 70 % stenosis created a relatively stronger and higher velocity flow in the parent artery of all models. The relatively stronger flow went along the inertial path of flow in the parent artery, which was dominated by the inertial force. With the moderate distance between aneurysm and stenosis, the relatively stronger flow became the aneurysmal inflow, and created a relatively higher velocity in the aneurysm. From Meng's result, the momentum of inflow drastically increases by several orders of magnitude as parent artery curvature increased from zero (straight vessel). They inferred that inertia-driven force induce the aneurysmal flow by creating an inflow that was 103 to 104 times stronger than the shear-driven flow [6]. In this research, the inflow was intensified when the curvature of parent artery increased, and as well as when the degree of stenosis increased, as shown in Figure AI-3, which indicates the flow inside the aneurysm is apparently affected by the geometric deformation of the blood vessel.

Also, from the comparison between the velocity in models with different curvatures in Figure A1-2, it reveals that the reattachment length became smaller as the curvature of parent artery increased. Because the flow in curved vessels is driven by inertial force, the flow is more likely to run along the inertial path, so that the direction of the flow tends to point out at the convex side of the artery, as shown in Figure AI-4. As for the recirculation flow after the stenosis, the behaviour of reattachment flow was also different from straight vessel affected by the inertial force. When the curvature of the parent artery becomes higher, it is easier for the reattachment flow after the stenosis to

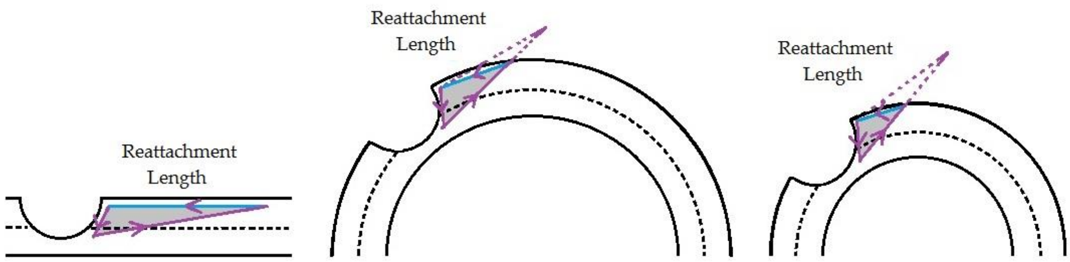

Figure AI-6 Sketch of the direction of flow in parent artery

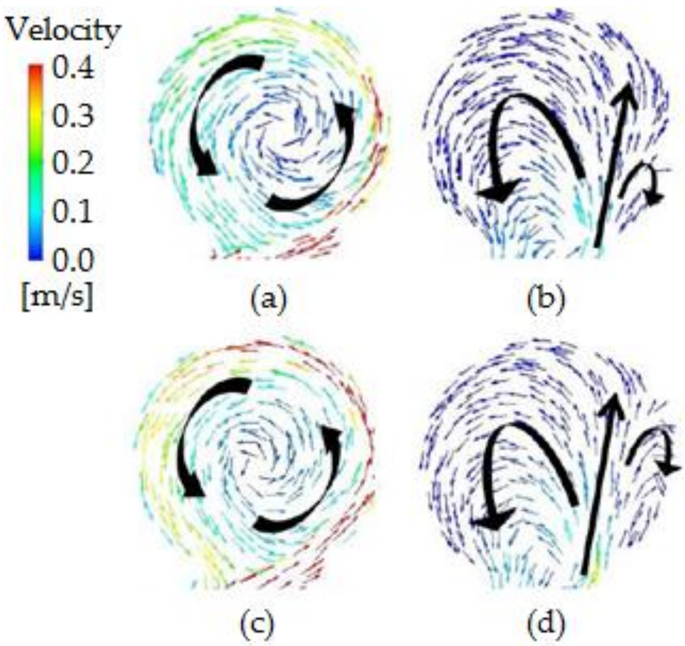

Figure AI-5 Aneurysmal flow pattern affected by vascular curvature and position of stenosis: (a) C = 0.05 mm -1, moderate (b) C = 0.05 mm -1, short (c) C = 0.08 mm -1, moderate (d) C = 0.08 mm -1, short (vascular curvature, distance between stenosis and aneurysm)

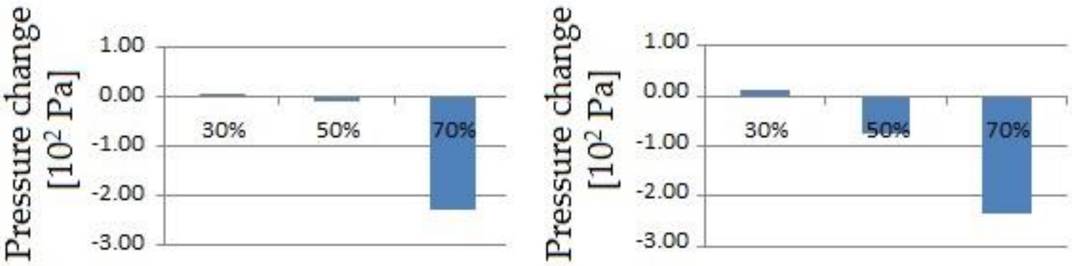

Figure AI-7 Intra-aneurysmal pressure (average value) change between models in different artery curvatures: (a) C = 0.05 mm $^{-1}$ (b) C = 0.08 mm $^{-1}$

arrive at the artery wall, as shown in Figure AI-5. Thus, the phenomenon that the reattachment length became smaller as the curvature increased can be understood.

Since the reattachment length became smaller in the curved vessels, Figure A1-2 also demonstrates that even in the case with severe stenosis, the reattachment flow was not long enough to arrive at the aneurysm orifice when the distance between stenosis and aneurysm was moderate, so that the reattachment flow did not affect the aneurysmal flow pattern. However, when the distance between stenosis and aneurysm decreased to adequate small, the recirculation flow extended to the aneurysm neck, as shown in Figure AI-6, and the aneurysmal flow pattern was disturbed to multi-vortexes flow pattern. Therefore, though the recirculation in curved vessel is not as large as that in the straight vessel, the existence of severe stenosis may also impact the aneurysmal flow pattern, provided that the distance between stenosis and aneurysm is adequate small.

Pressure

Figure AI-7 shows the aneurysmal pressure change in different models. Pressure changes in curved vessels were similar to that in the straight vessels, the aneurysmal pressure decreased when the degree of stenosis increased from 30% to 70 %. However, comparing to straight vessels, the curved vessels produced less noticeable decreasing value. Between models with same severity of stenosis in different curvatures, the value of the pressure change fluctuates in a close range. In the case of 70 % stenosis, the aneurysmal pressure drop was about 248 Pa (2.41 mmHg) higher than the pressure drop in the case of 30 %.

Discussion

This study implemented the simulation of idealised models with a certain shape and size of aneurysm on straight vessels with different degree of stenosis on various positions, and also on curved vessels with two different curvatures. Many researches have shown the flow pattern in parent artery with aneurysm to describe the normal flow patterns inside the aneurysm [6,70]. Also, the phenomenon of flow recirculation is an important characteristic of stenosis which has been discussed before [113,117,148]. Different morphologies of parent artery and degrees of stenosis may influence the flow pattern in the artery, especially for the reattachment flow. No research has provided the simulation result of model with an aneurysm exists after a stenosis in the parent artery, however such kind of clinical cases exist [149]. Hence, the simulation of models with both stenosis and aneurysm is necessary to be carried out to observe the unusual and complicated flow pattern, especially when the stenosis is severe enough to create a recirculation at its downstream. Result shows that the existence of stenosis and the consequent reattachment flow influences the aneurysmal flow pattern depends on a crucial factor—the distance between them.

Some limitations exist in this study because the use of idealised geometries, as the smooth wall and the lacking of bifurcation may neglect the complexity of the haemodynamics in the flow, since more CFD studies of blood flow intends to use patient-specific models [150–152]. However, this study aims to examine the impact on aneurysmal haemodynamics with the existence of pre-aneurysmal stenosis in different size and positions. Comparing to the patient-specific model, the adoption of idealised model intends to omit the undesired geometric complexities that could significantly complicate the haemodynamic investigation [70]. Besides, the determine of boundary conditions may significantly influence the simulation result, even for models with similar morphologies.

Conclusion

To learn the different haemodynamics in the geometry with both stenosis and aneurysm and study the influence to the aneurysm when a pre-aneurysm stenosis exists which may threaten people's health and life even more severely, numerical simulation of idealised models of straight and curved blood vessels with both aneurysm and pre-aneurysm stenosis have been studied, with altering the degree of stenosis, the distance between stenosis and aneurysm and the curvature of parent artery. The present study emphasizes the abnormal phenomenon in flow pattern and increase of intra-aneurysmal pressure change affected by the existence of pre-aneurysm stenosis.

Observing the flow pattern of all models, the reattachment length increases as the degree of stenosis increases (refer to Section 2.4 for more details). Dominated by inertial force, reattachment flow in curved vessel is obvious smaller than that of straight vessel, and it tends to decrease as the curvature of parent artery increases. As to artery with severe stenosis and short distance between stenosis and aneurysm, the flow pattern may become multi-vortexes flow pattern when the reattachment flow extends to the aneurysm neck.

Because of the existence of stenosis, the intra-aneurysmal pressure shows a trend of decrease. As the degree of stenosis becomes severe, the decrease of intra-aneurysmal pressure increases. In other words, the treatment of pre-aneurysm stenosis may create higher pressure condition to the aneurysm which should be taken into consideration in further studies as well as the clinical research.

Appendix II

In-plane Vortex Centre Measured by PIV and CFD in Chapter 4

Table AII-1 Vortex difference between measurement by PIV and CFD in Chapter 4

	Flowrate	Plane	Method	Horizontal Difference	Vertical Difference
No Stent	150	X2	CFD	4 mm further right	Similar
			PIV		
	250	X1	CFD	Similar	1.7 mm higher
			PIV		
		X2	CFD	4.5 mm further right	Similar
			PIV		
		X3	CFD	1.5 further left	Similar
			PIV		
Silk	250	X2	CFD	2.5 mm further right	Similar
			PIV		
	400	X2	CFD	4.3 mm further right	Similar
			PIV		

Appendix III

Absolute value of MFR and EL
for untreated cases
in Chapter 6

Table AIII-1 Absolute values of MFR and EL for the untreated cases in Chapter 6

Flow Rate [mL/min]	Aneurysm A		Aneurysm B	
	MFR [kg/s]	EL [kg·m^2/s^3]	MFR [kg/s]	EL [kg·m^2/s^3]
150	2.72E-03	1.87E-05	5.02E-03	8.16E-05
250	4.88E-03	1.02E-04	9.83E-03	4.16E-04
400	8.31E-03	4.27E-04	1.81E-02	1.83E-03